POLISH ACADEMY OF SCIENCES – WROCŁAW BRANCH
WROCŁAW UNIVERSITY OF TECHNOLOGY

ARCHIVES OF CIVIL AND MECHANICAL ENGINEERING

Quarterly
Vol. X, No. 2

WROCŁAW 2010

EDITOR IN CHIEF

ZBIGNIEW GRONOSTAJSKI

EDITORIAL LAYOUT AND PROOF-READING

WIOLETTA GÓRALCZYK

TYPESETTING

SEBASTIAN ŁAWRUSEWICZ

SECRETARY

WIOLETTA GÓRALCZYK

Publisher: Committee of Civil and Mechanical Engineering
of Polish Academy of Sciences – Wrocław Branch,
Faculty of Civil Engineering and Faculty of Mechanical Engineering
of Wrocław University of Technology

OFICYNA WYDAWNICZA POLITECHNIKI WROCŁAWSKIEJ
Wybrzeże Wyspiańskiego 27, 50-370 Wrocław
http://www.oficyna.pwr.wroc.pl
e-mail: oficwyd@pwr.wroc.pl

ISSN 1644-9665

Drukarnia Oficyny Wydawniczej Politechniki Wrocławskiej. Zam. nr 557/2010.

Contents

Spis treści

ARCHIVES OF CIVIL AND MECHANICAL ENGINEERING

Vol. X 2010 No. 2

Investigations of the friction welding of Incoloy MA 956 alloy

A. AMBROZIAK
Institute of Production Engineering and Automation, Wrocław University of Technology, Poland.

Friction welded similar material (work hardened and thermally treated) alloy Incoloy MA 956 joints and Incoloy MA 956 alloy/austenitic steel X10CrNiTi 189 joints were tested. The microstructures, microhardness and tensile strength of the joints were determined. Optimum friction welding process parameters were matched. Friction welding has been found to be useful for joining Incoloy MA 956 alloys together and for joining the latter with austenitic steel X10CrNiTi 189.

Keywords: *superalloys, MA 956, friction welding, tensile strength, hardness*

1. Introduction

Iron- or nickel-based oxide-dispersion-strengthened (ODS) alloys are used in high-temperature applications under normal atmospheric conditions. The alloys also contain chromium, aluminium, iron, yttrium oxide as well as molybdenum, zirconium and tantalum additions. Since metallic materials having such a composition are not in the state of equilibrium they are produced by powder metallurgy methods. The production process includes such operations as high-energy grinding and mixing of components, hot extrusion and recrystallizing annealing.

Elongated grains occur in the microstructure of ODS alloys. Yttrium oxide occurs mainly on grain boundaries and hinders their growth at high temperatures. This method of producing ODS alloys is called mechanical alloying. When it is said that in ODS alloys segregations occur on grain boundaries, it is meant the boundaries of the grains introduced in the solid state or through thermal treatment (recrystallizing annealing), by means of powder metallurgy methods. The mechanical properties of ODS alloys in the direction conforming to the direction of strain are better than in the perpendicular direction. Such alloys can work at temperatures up to 1300 °C (iron matrix alloys, called ferritic ODS alloys) or up to 1100 °C (nickel matrix alloys, called austenitic ODS alloys), preserving good resistance to oxidation and gas corrosion.

Since ODS alloys are not in a state of metallurgic equilibrium, when melted, the alloy and the introduced yttrium oxide separate and the latter passes into slag and to the surface of the weld or it remains inside the weld. As a result, ODS alloys lose their original properties, particularly their heat resistance.

ODS alloys can be joined together by thermal welding, but welding in which the native material is partially melted results in weld porosity (especially in iron-based alloys) and cracks (especially in nickel-based alloys), which cannot be avoided even when electron beam welding is employed [1].

Hence attempts are made to apply solid-state welding and above all friction welding, diffusion welding and high-temperature soldering to join ODS alloys together [1–5].

2. Test methodology

Conventional friction welding was conducted in a vertical welding machine type KUKA RS 30 (Figure 1). The scheme of the welding process is shown in Figure 2.

Fig. 1. Friction welding machine (vertical system)

An iron-based ODS alloy of Incoloy MA 956 grade (20% Cr, 4.5% Al, 0.5% Ti, 0.05% Y_2O_3, the rest – Fe) in a work hardened state (specimens denoted as MA 956F) and thermally treated (annealing at 1300 °C for 30 minutes – specimens denoted as MA 956H) and austenitic steel of grade X10CrNiTi 189 were used in the tests. Similar- and dissimilar material joints were made.

The welding process parameters adopted for the materials (25 mm ϕ rods were welded) are shown in Table 1. The obtained joints were evaluated through metallographic examinations, microhardness measurements and static tensile tests.

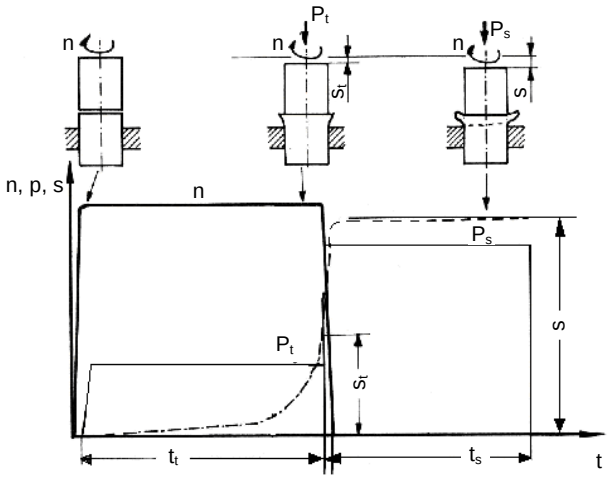

Fig. 2. Scheme of friction welding process used in investigations (n = 1500 min^{-1}, P_t – pressure during the period of friction, P_s – pressure during the period of upsetting, t_t – duration of the period of friction, s_t – contraction during the period of friction, s – total contraction during the whole period of welding)

Table 1. Friction welding parameters for tested joints

Pos.	Material pairs	Specimen No.	P_t [MPa]	P_s [MPa]	t_t [s]	t_s [s]	s_t [mm]	s [mm]
1	MA 956H/MA956H	1	48	135	30	40	3.4	13.6
2		2	48	135	40	40	3.1	16.8
3		3	48	90	20	40	2.5	3.9
4		4	48	110	20	40	2.4	6.4
5	MA 956F/MA 956F	10	48	135	15	40	9.4	16.3
6		11	48	135	10	40	5.0	11.1
7		12	48	90	20	40	14.2	19.3
8		13	48	110	20	40	14.4	20.6
9	MA 956H/MA 956F	6	48	135	30	40	14.0	23.1
10		7	48	135	40	40	17.5	29.2
11		8	48	90	20	40	8.4	12.1
12		9	48	110	20	40	8.8	14.6
13	MA 956F/X10CrNiTi 189	14	48	135	15	40	3.8	9.1
14		15	48	135	10	40	2.4	5.9
15		16	48	90	20	40	5.6	8.7
16		17	48	110	20	40	5.6	10.2
17	MA 956H/X10CrNiTi 189	19	48	135	30	40	2.5	10.1
18		20	48	135	40	40	2.2	12.8
19		21	48	90	20	40	0.9	2.4
20		22	48	110	20	40	0.8	3.7

3. Test results

The microstructure of the Incoloy MA 956 alloy in its initial state is shown in Figure 3. Alloy Incoloy MA 956F has a close-grained structure (Figure 3a) with a microhardness of 368 $HV_{0.025}$ in the longitudinal section and 403 $HV_{0.025}$ in the cross section. After an additional thermal treatment (annealing) alloy Incoloy MA 956H shows a coarse-grained structure (Figure 3b) with elongated grains. As a result of the heat treatment the microhardness of the alloy decreased to about 286 $HV_{0.025}$ at a small scatter of hardness measurement results for the two specimen directions.

The size of flash and the width of the heat affected zone (HAZ) in the axis of the specimen and outside (Figure 4) were measured for the tested friction welded joints (in their longitudinal sections). The results of the measurements are shown in Table 2.

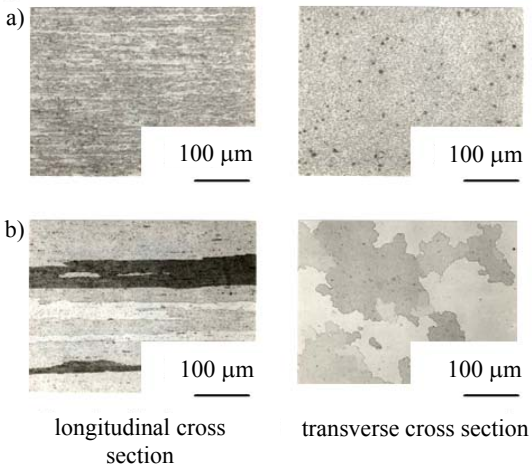

Fig. 3. Microstructures of ODS alloys: a) MA 956F; b) MA 956H

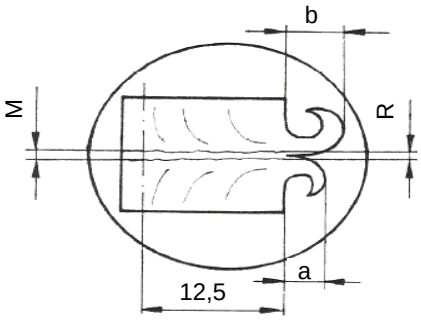

Fig. 4. Scheme of flash size and HAZ width measurements in tested friction welded joints

Table. 2. HAZ width and flash size in tested friction welded joints (symbols as in Figure 4)

No.	Material pairs	Specimen No.	HAZ width [μm]		Flash size [mm]	
			M	*R*	*a*	*b*
1	MA 956H/MA 956H	1	96	205	8.5	9.0
2		2	75	150	9.3	3.3
3		3	648	960	4.1	4.0
4		4	360	600	4.4	5.8
5	MA 956F/MA 956F	10	270	180	6.8	6.7
6		11	170	170	5.8	6.1
7		12	400	140	7.5	7.5
8		13	250	140	7.6	7.6
9	MA 956H/MA 956F	6	170	215	10.8*	7.4**
10		7	140	300	11.0*	7.1**
11		8	600	290	8.4*	4.7**
12		9	370	360	8.7*	5.3**
13	MA 956F/X10CrNiTi 189	14	36	300	6.7*	4.8***
14		15	10	150	6.2*	3.6***
15		16	80	55	7.2*	3.8***
16		17	30	130	7.3*	4.9***
17	MA 956H/X10CrNiTi 189	19	170	300	6.9**	6.9***
18		20	60	290	6.2**	7.8***
19		21	720	280	2.3**	2.9***
20		22	860	300	3.0**	3.9***

* – flash on MA 956F side
** – flash on MA 956H side
*** – flash on steel X10CrNiTi 189 side

4. Similar-material Incoloy MA 956 joints

After alloy Incoloy MA 956 F is friction welded (whereby it is in a work hardened state) a ca 200 μm wide weld zone characterized by large grains can be distinguished. A weld interface passing into a fine-grained native material is visible (Figure 5a). A material texture towards the flash, i.e. perpendicularly to the specimen's axis, occurs in both zones. At lower upsetting pressures inclusions and porosities occur in the weld zone (specimen 3, Table 1).

A 75 μm (specimen middle) to 960 μm (specimen edge) wide weld zone with a varying microstructure resembling that of similar-material MA 956 F joints (Figure 5b, Table 2) occurs in the heat treated Incoloy MA 956 H alloy joints. Microcracks running on grain boundaries are visible in the microstructure of the specimens, particularly in the outer areas of the joint (Figure 5c). It was found that the greater the upsetting pressure and the shorter the friction time, the larger the number of microcracks. The microhardness in the weld zone is reduced to about 250–280 $HV_{0.025}$ (by about 100 units relative to the native material) (Figure 7a).

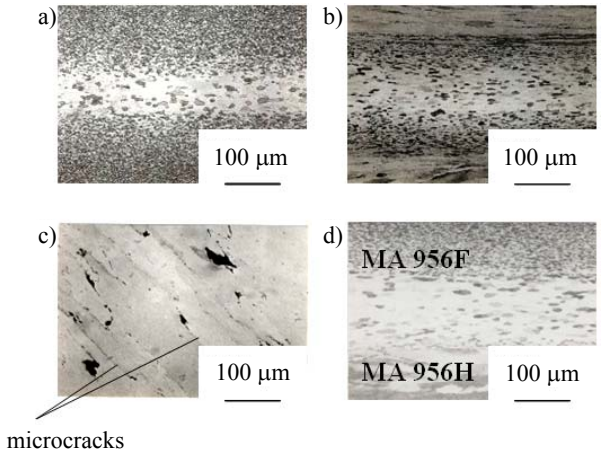

Fig. 5. Microstructures of friction welded joints: (a) Incoloy MA 956F/MA 956F, (b) Incoloy MA 956H/MA 956H, (c) crack in MA 956H/MA 956H, (d) Incoloy MA 956F/MA 956H

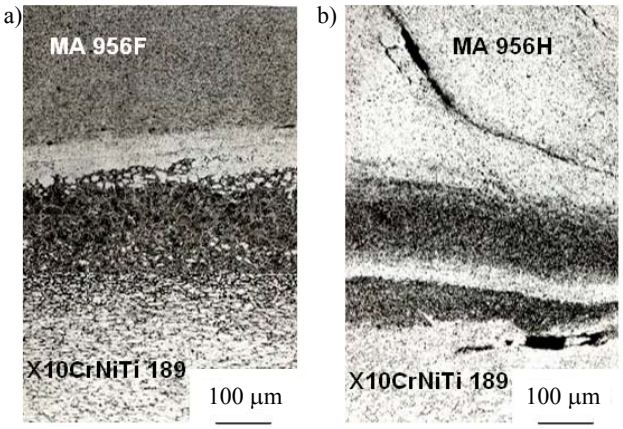

Fig. 6. Microstructure of Incoloy MA 956F-steel X10CrNITi 189 joint: (a) MA 956F/X10CrNiTi 189, (b) MA 956H/X10CrNiTi 189

5. Dissimilar-material joints

A 140–600 μm wide weld zone occurs in the dissimilar-material Incoloy MA 956 F/MA 956 H joints (Figure 5d). Because of the great upsetting pressures and the long friction times, the weld zone is narrow. At great upsetting pressures microcracks occur on the MA 956 H alloy side, but in smaller numbers than in the case of the similar-material joint. A 10 μm (specimen axis) to 300 μm (specimen edges) wide weld zone occurs in the dissimilar-material Incoloy MA 956/steel joints (Figure 6a).

The smaller the upsetting pressure, the wider the weld zone, but then discontinuities occur at the boundary of material flow from the weld zone, both on the MA 956 alloy side and the X10CrNiTi 189 steel side (Figure 6b). The tests have shown that the pressures during upsetting should be at least 110 MPa high.

As shown by microhardness measurements (Figure 7b), hard (ca 510 $HV_{0.025}$) microstructures occur in the weld zone at the material flow boundary on the X10CrNiTi 189 steel side (Figure 6a). Microhardness is slightly reduced (to about 220 $HV_{0.025}$) in the weld zone on the MA 956 alloy side.

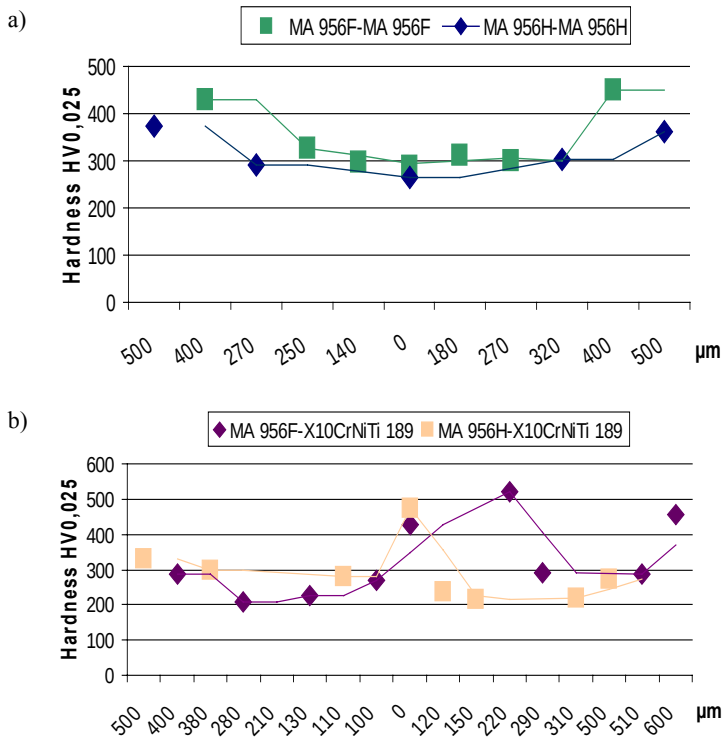

Fig. 7. a) Microhardness in outer specimen areas in similar-material Incoloy MA 956 alloy joints (specimen 4 and 10, Table 1), b)dissimilar-material Incoloy MA 956 alloy/X10CrNiTi 189 steel joints (specimen 14 and 20, Table 1)

6. Tension testing of joints

Static tension tests were carried out on specimens 20 mm in diameter in order to evaluate the quality of the friction welded joints. The results are shown in Table 3. The similar-material hardened Incoloy MA 956 F alloy joints show a relatively high strength (about 927 MPa) and the fracture, without visible plastic deformations, occurs in the weld zone.

The thermally treated Incoloy MA 956 H alloy joints subjected to the tension test show considerable plastic deformations and the fracture occurs in the native material at a distance of 30–40 mm from the weld zone. The tensile strength is about 680 MPa.

In the dissimilar-material Incoloy MA 956 H/MA 956 F joints the strength of the joint's strength is about 694 MPa and the fracture takes place in the weld zone.

At low upsetting pressures the average strength of the dissimilar-material Incoloy MA 956 alloy/steel X10CrNiTi 189 joints was about 497 MPa (specimen 16). At higher upsetting pressures (above 110 MPa) a visible elongation on the steel side occurs, the fracture takes place in steel X10CrNiTi 189 and strength is about 560 MPa.

Table 3. Static tensile test results for friction welded joints

No.	Material pairs	Specimen No.	$R_{p0.2}$ [MPa]	R_m [MPa]	Fracture location
1	MA 956H/MA 956H	2	544.9	683.75	native material
2		3	527.9	675.8	native material
3	MA 956F/MA 956F	10	877.4	926.75	weld zone
4	MA 956H/MA 956F	6	566.25	694.3	weld zone
5	MA 956F/X10CrNiTi 189	15	325.75	561.4	steel
6		16	315.95	497.15	weld zone, steel
7	MA 956H/X10CrNiTi 189	20	326.75	593.1	steel

7. Conclusions

The following conclusions can be drawn from the investigations:

1. Friction welding makes it possible to obtain good quality similar-material Incoloy MA 956 alloy joints and dissimilar-material Incoloy MA 956 alloy/austenitic steel X10CrNiTi 189 joints.

2. The original structures of the materials change in a range of only ca 10 μm (in the specimen axis) to 1000 μm (in the outer areas of the joint).

3. The longer friction times (over 30 s) and the large upsetting pressures (from 110 MPa) result in narrower uniform weld zones.

4. Discontinuities in the hardened Incoloy MA 956 occur mainly in the specimen's outer areas when short friction times or small upsetting pressures are applied.

5. The tensile strength of the tested joints friction welded at an upsetting pressure of minimum 110 MPa is close to that of the native materials.

References

[1] Ambroziak A., Lison R.: *Schweißen und Löten von ODS-Werkstoffen*, Schweissen u. Schneiden, DVS-Verlag GmbH, Düsseldorf, Vol. 44, No. 7, 1992, pp. 371–376.

[2] Ates H., Turker M., Kurt A.: *Effect of friction pressure on the properties of friction welded MA 956 iron-based superalloy*, Materials and Design, Vol. 28, No. 3, 2007, pp. 948–953.
[3] Inkson B.J., Threadgill P.L.: *Friction welding of FeAl40 Grade 3 ODS alloy*, Materials Science and Engineering A, Vol. 258, Issues 1–2, 1998, pp. 313–318.
[4] Kalemba I., Dymek S., Hamilton C., Blicharski M.: *Microstructure evolution in friction stir welded aluminum alloys*, Archives of Metallurgy and Materials, Vol. 54, No. 1, 2009, pp. 75–82.
[5] Shinozaki K., Kang C.Y., Kim Y.C., Aritoshi M., North T.H., Nakao Y.: *The metallurgical and mechanical properties of ODS alloy MA956 friction welds*, Welding J. Res. Suppl. Vol. 76, No. 8, 1997, pp. 289–299.

Badania zgrzewania tarciowego stopu Incoloy MA 956

Badano złącza zgrzewane tarciowo jednoimienne stopu Incoloy MA 956 w stanie umocnionym i obrobionym cieplnie, jak i ich połączenia ze stalą austenityczną X10CrNiTi 189. Określono mikrostruktury, mikrotwardość oraz wytrzymałość na rozciąganie wykonanych złączy. Dobrano optymalne parametry procesu zgrzewania tarciowego. Stwierdzono przydatność zgrzewania tarciowego do procesu łączenia jednoimiennych stopów Incoloy MA 956, jak i ich złączy ze stalą austenityczną X10CrNiTi 189.

ARCHIVES OF CIVIL AND MECHANICAL ENGINEERING

Vol. X 2010 No. 2

An analysis of the load-carrying capacity of elements subjected to complex stress states with a focus on the microstructural failure

P.G. KOSSAKOWSKI
Kielce University of Technology, Al. Tysiąclecia Państwa Polskiego 7, 25-314 Kielce, Poland.

The paper analyses the load-bearing capacity of S235JR steel elements subjected to complex stress states, taking into account the effect of microstructural damage. Assessing the material required conducting a microstructural analysis and standardized tensile strength tests. A modified Gurson–Tvergaard–Needelman (GTN) model was used to numerically analyse S235JR steel elements under the action of complex stresses. The results of the numerical analysis were reported to be consistent with those obtained during the strength tests. The method for the numerical calculations was described along with the admissible results and the criteria of failure for S235JR steel basing on the modified GTN model and the development of microdamage. As S235JR steel is a common structural material in Poland, the investigation results will be of use to a number of engineers and other specialists responsible for determining the load-carrying capacity and structural safety of elements or whole systems.

Keywords: *Gurson–Tvergaard–Needelman model, voids, numerical calculations, S235JR steel*

1. Introduction

While determining the structural safety of an element, it is necessary to measure the actual stresses and compare them with the admissible values defining the strength of the material. The analysis is relatively easy to conduct if an element is under the action of uniaxial stress. If complex stress states are involved, i.e. when the failure stress is a three-stress function, the analysis becomes more complicated. As the failure of a material (plastic deformation or fracture) is dependent on more than one major stresses, the safety of a structure can be assessed using the so called Huber strength hypotheses. The tensile stress of an element in the complex stress state is determined basing on the reduced stress compared to the failure stress, which is defined for structural steels according to the Huber–Mises (HM) hypothesis. A number of studies show that the HM model is not always suitable to analyse the plastic state in and beyond the range of deformations corresponding to the necking of an element subjected to tension. Assuming the continuum of the material, one cannot apply this model to establish the influence of the microstructural defects on the material strength. Such phenomena can be analysed using other models defining the relationship between the particular failure stages and the strength of the material.

One of the first models of this type was the Kachanov model [1], in which the failure parameter is defined as the damaged area divided by the unaffected area. Kachanov's approach was extended by Lemaitre, who introduced the potential elastic energy function to analyse the potential failure of the material [2–3]. Lemaitre's model was used mainly to describe creep rupture and fatigue of the materials. As the failure parameter is difficult to define, especially measure, the model was not appropriate for modeling the fracture phenomena for elements subjected to static or dynamic loads. Kachanov's model did not take into account the conditions of damage formation due to loading. The models by Kachanov and Lemaitre are some of the few used in elastic-plastic damage mechanics which take into consideration material failure. As suggested by Murakami in Ref. [4], the other models used for describing material damage are those of Gurson [5], Suquet [6], Cordebois and Sidoroff [7], Tvergaard [8–9], Rousselière [10–11], Dragon and Chihab [12], Chow and Lu [13], Voyiadjis and Katt [14], Murzewski [15],] Mou and Han [16], Saanouni [17], and Taper et al. [18]. In the recent years, the Gurson model, which links the degree of failure with the material structure, has been modified extensively.

The Gurson model for a porous solid [5], which is a modified Huber–Mises criterion, defines the influence of an increase in the void volume fraction on the strength of the material. This model was further modified by Tvergaard [19], and then by Tvergaard and Needleman [20–21]. The two scientists developed a method for the calculation of failure loads resulting from ductile fracture by considering selected microstructural parameters and plastic properties of a material, which is referred to as the GTN model. All the above mentioned models will be discussed further in this paper.

Damage in the form of voids occurs on the existing inclusions or separations. The growth and coalescence of these voids result in the development of localized plastic deformations. Many researchers suggest that the process of void growth is dependent on the state of stress, particularly the stress triaxiality ratio.

The cracking of polycrystalline structures is a complex issue. The processes of crack initiation and propagation are closely related to the material microstructure. There are three basic types of fracture mechanisms, i.e. brittle, shear and ductile. In shear and ductile fracture patterns, the cracking is attributable to the nucleation and coalescence of voids (see Figures 1 and 2) [22].

The current studies conducted by using the GTN model aim at determining microstructural parameters for different types of materials [23–28], analyzing the plasticity due to void initiation and growth, and defining the effect of voids on the load-carrying capacity of elements [29–39]. A number of studies [30–32] show that, for alloys and structural steels, the GTN model ensures better consistency of results obtained by numerical calculation (modelling) with experimental results than the HM model. By applying the GTN model to calculations, one is capable of analyzing the phenomenon of void growth, which allows locating the "weak" points in the structure, especially those susceptible to a local loss of load-carrying capacity.

From the present state of knowledge concerning the numerical modelling of steel plasticity, we can conclude that the modelling has been performed for small simple elements made of different types of steel or metallic alloys.

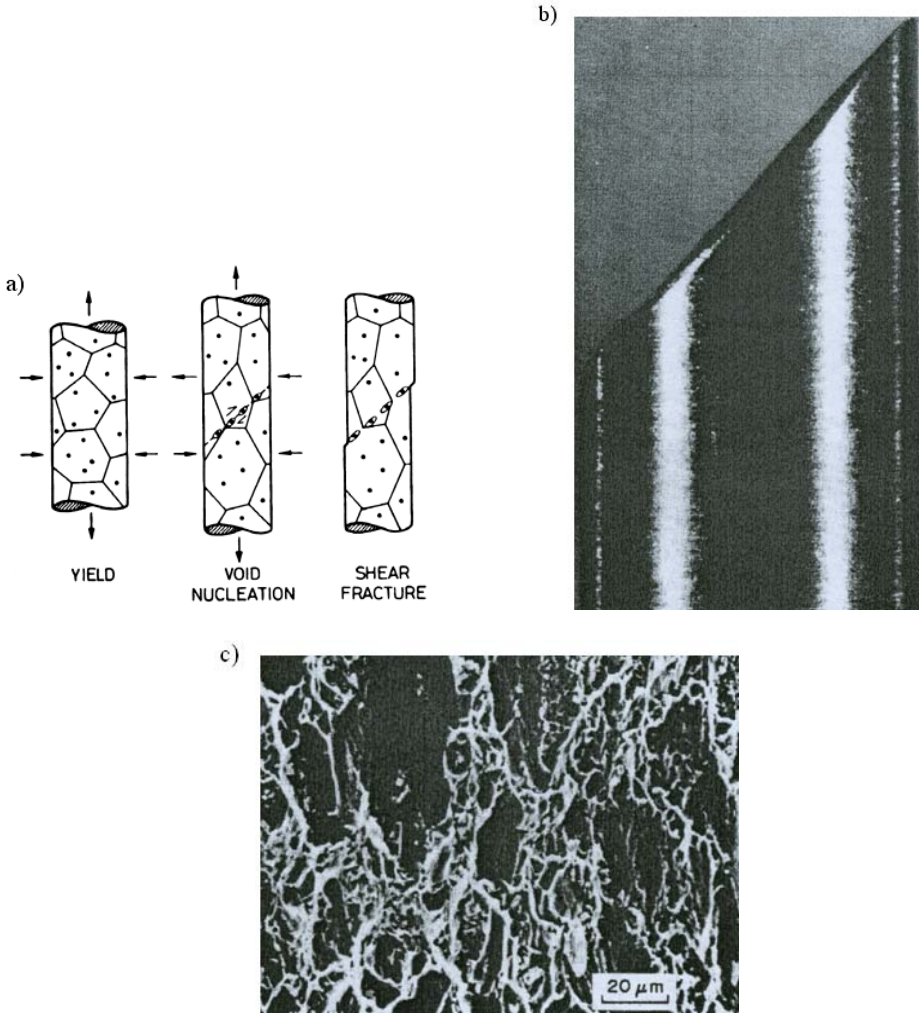

Fig. 1. a) Schematics of the nucleation, growth, and coalescence of voids leading to shear fracture, b) Macrophotograph of a 7075-T4 steel specimen subjected to tension which failed by shear fracture, c) Microphotograph of a 7075-T4 steel specimen which failed by shear fracture [22]

Most results are obtained by conducting simple strength tests, mainly tensile strength tests. Numerical analyses are performed using the method of best fit to material constants (the GTN model) for elements with predetermined geometries and strength properties. Microstructural parameters are frequently determined basing on the curve fit-

ting principle. There is no comprehensive approach that would allow performing numerical calculations for arbitrary elements. Another drawback is the lack of standardized microstructural parameters to develop a GTN model for steels used most commonly in engineering.

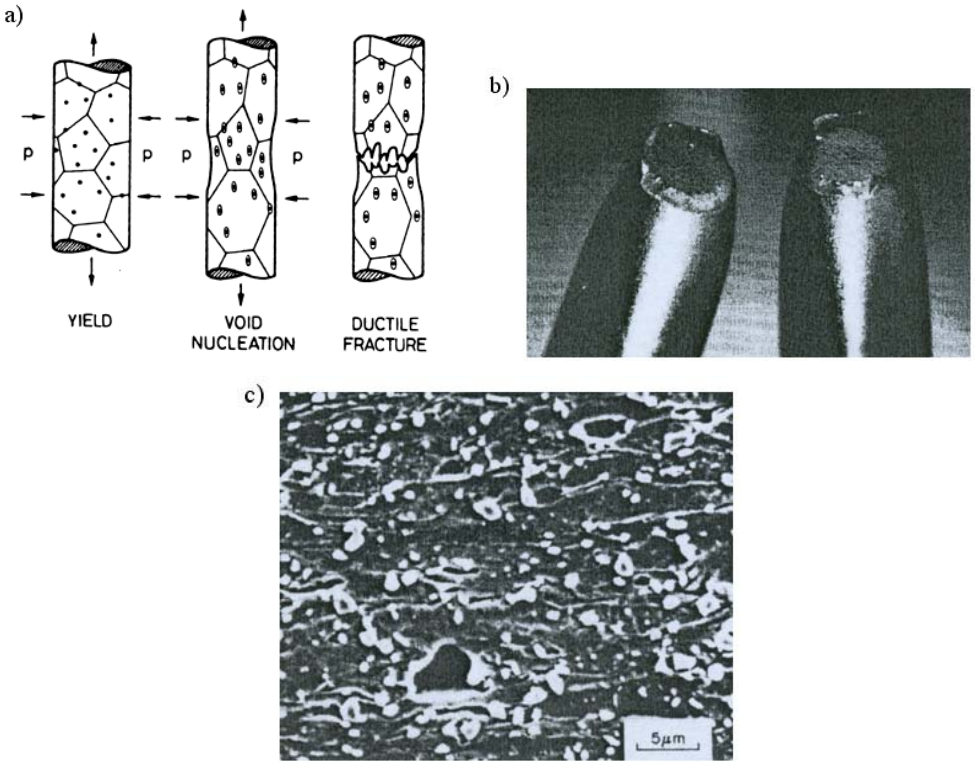

Figure 2. a) Schematics of the nucleation, growth and coalescence of voids leading to ductile fracture, b) Macrophotograph of a 1080 spheroidized steel specimen subjected to tension that failed by ductile fracture, c) A SEM microphotograph showing void growth in 1045 spheroidized steel subjected to axial tension, [22]

It is thus essential to develop a procedure for the numerical modelling of the load limit for any element subjected to any load, taking into account the effect of microfailure. This paper includes results of a load-carrying capacity analysis and discusses the void growth in S235JR steel elements in complex stress states basing on the Gurson–Tvergaard–Needelman (GTN) model, which takes into consideration the material structure.

The aim of the research was to determine the standardized material parameters for S235JR steel by conducting microstructural studies and standard tensile strength tests, followed by numerical modelling of data. As a result, it was possible to determine the parameters of the modified Gurson–Tvergaard–Needelman (GTN) model by analyzing the structure of S235JR steel.

The modified model was used to numerically analyse elements subjected to complex stress states, i.e. elements with different geometries as opposed to standard specimens subjected to tension.

The paper discusses the numerical calculation procedure, the result analysis, and the criteria of failure for S235JR steel obtained on the basis of the modified GTN model and the void growth. S235JR steel was selected for the tests because it is a common structural material in Poland. The data may be used for any analyses and expertise connected with the assessment of the load-carrying capacity and safety of structural elements and systems.

2. Gurson–Tvergaard–Needelman (GTN) damage model

As emphasized at the beginning, the classic Huber–Mises (HM) model cannot be used to analyse the effects of damage of microstructure on the load-carrying capacity and the strength of materials. Effective stresses (stress intensity) are a function of principal stresses according to the formula:

$$\overline{\sigma} = \frac{1}{\sqrt{2}}\sqrt{(\sigma_1 - \sigma_2)^2 + (\sigma_2 - \sigma_3)^2 + (\sigma_1 - \sigma_3)^2}, \tag{1}$$

where:

$\overline{\sigma}$ – von Mises effective stresses,

σ_1, σ_2, σ_3 – principal stresses.

The first model to take into consideration microdamage (pores, voids) was the Gurson model [5], which assumes that the proportion of voids in the plastic potential function is dependent on the void volume fraction f rather than the void volume, in accordance with the following relationship:

$$\Phi = \left(\frac{\overline{\sigma}}{\sigma_0}\right)^2 + 2f\cosh\left(\frac{3\sigma_m}{2\sigma_0}\right) - 1 - f^2 = 0, \tag{2}$$

where:

Φ – non-dilatational strain energy,

$\overline{\sigma}$ – von Misses effective stress according to the HM hypothesis,

σ_0 – strength of the material resulting from the tensile strength curve (yield stress),

σ_m – hydrostatic pressure (mean stress),

f – void volume fraction.

This condition was modified by Tvergaard [19] as:

$$\Phi = \left(\frac{\overline{\sigma}}{\sigma_0}\right)^2 + 2q_1 f^* \cosh\left(-q_2\frac{3\sigma_m}{2\sigma_0}\right) - \left(1 + q_3 f^{*2}\right) = 0, \tag{3}$$

where:

f^* – actual void volume fraction,

q_i –Tvergaard coefficients describing the plastic properties of the material.

As can be seen from the GTN model, the influence of the plastic properties was taken into consideration by introducing the Tvergaard coefficients q_i, their values being as follows:

$$q_i = \begin{cases} q_1 = 1.5 \\ q_2 = 1.0 \\ q_3 = q_1^2 = 2.25 \end{cases}. \tag{4}$$

The above values have been confirmed in numerous studies as typical of many metals and steel grades. It should be noted that in the original Gurson condition, the coefficients characterizing the plastic properties of the material were $q_1 = q_2 = q_3 = 1$ [5]. When $f = 0$, the GTN yield condition (1) is reduced to form defined according to the HM condition. In the GTN model, the void volume fraction f^* is determined as follows:

$$f^* = \begin{cases} f & \text{for} \quad f \le f_c \\ f_c + \dfrac{\bar{f}_F - f_c}{f_F - f_c}\left(f - f_c\right) & \text{for} \quad f_c < f < f_F \\ \bar{f}_F & \text{for} \quad f \ge f_F \end{cases}, \tag{5}$$

where:

f_c – critical void volume fraction,

f_F – void volume fraction corresponding to the loss of material strength.

$$\bar{f}_F = \frac{q_1 + \sqrt{q_1^2 - q_3}}{q_3}.$$

An increase in the void volume fraction f is defined by the following relationship:

$$df = df_{gr} + df_{\text{nucl}} \tag{6}$$

where:

df_{gr} – time derivative of the volume fraction of voids existing in the material,

df_{nucl} – time derivative of the volume fraction of voids initiated by the deformation.

An increase in the volume fraction of voids df_{gr} existing in the material is defined as:

$$df_{gr} = \left(1 - f\right) d\varepsilon^{pl} : I \tag{7}$$

An increase in the volume fraction of voids initiated by the deformation df_{nucl} is defined as:

$$df_{nucl} = A\, d\bar{\varepsilon}_m^{pl} \tag{8}$$

An important parameter is the intensity of the nucleation (initiation) of voids A, defined as:

$$A = \frac{f_N}{s_N\sqrt{2\pi}} \exp\left[-\frac{1}{2}\left(\frac{\bar{\varepsilon}_m^{pl} - \varepsilon_N}{s_N}\right)\right], \tag{9}$$

where:

f_N – volume fraction of voids nucleated (initiated) on inclusions,
ε_N – mean strain of the void nucleation (initiation),
s_N – standard deviation of the nucleation strain,
$\bar{\varepsilon}_m^{pl}$ – mean plastic strain.

3. Determining the microstructural parameters of the GTN model

3.1. Microstructural analysis

The first step of the material analysis was to obtain microstructural images of S235JR steel [40] with a ferritic-perlitic matrix (Figure 3). As can be seen, there are a large number of non-metallic inclusions, which are mainly sulfides and brittle oxides. S235JR steel is reported to have appropriate metallurgical purity.

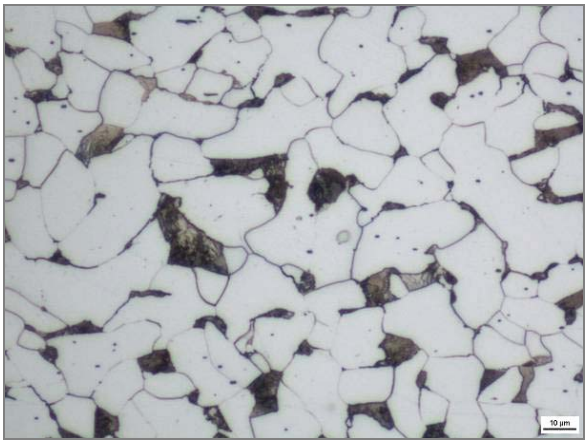

Fig. 3. SEM image of S235JR steel (transverse cross-section, middle layer) [40]

Sulfide inclusions were elongated in shape, with their length reaching 61.9 μm. Their distribution in the volume was irregular. They were arranged in bands. Table 1 shows the maximum diameter d_{max} and the extension ratio d_{max}/d_2, where d_2 is the equivalent diameter.

Other non-metallic inclusions found in the tested materials are uniaxial brittle oxide inclusions, which may co-occur with sulfide inclusions. To fully characterize non-metallic inclusions in the material, it was necessary to determine the basic stereological parameters:

- f_0 – void volume fraction,
- A – cross-sectional area,
- d_2 – equivalent diameter,
- d_{max} – maximum diameter,
- d_{max}/d_2 – extension ratio.

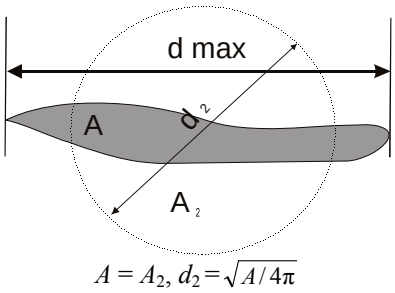

Fig. 4. Defining the stereological parameters for non-metallic inclusions [40]

Table 1. Comparing the results of the quantitative analysis of the images [40]

Cross-section	Cross-sectional area	Void volume fraction	n	A [μm^2]		d_2 [μm]		d_{min} [μm]		d_{max} [μm]		d_{max}/d_2	d_{max} (for the largest inclusion)
				mean value	std. dev	mean value	std. dev	mean value	std. dev	mean value	std. dev		
Transverse	central	0.17%	62	5.3	13.1	2.1	1.6	1.2	0.6	4.2	5.8	2.0	61.9
Transverse	outer	0.07%	66	2.5	3.3	1.5	0.9	1.0	0.5	2.5	2.2	1.6	18.2
Longitudinal	central	0.06%	68	1.8	5.5	1.3	0.8	1.1	0.6	1.6	1.6	1.3	22.0
Longitudinal	outer	0.03%	49	1.5	2.9	1.2	0.7	1.0	0.5	1.5	1.3	1.3	18.3

3.2 Tensile strength tests

The next step was to perform static tensile strength tests for specimens with a circular cross-section, with the diameter of the specimen ϕ = 10 mm, the length of the measuring base l_0 = 50 mm, and the primary cross-sectional area S_0 = 78.5 mm^2, according to [41]. Two ranges of traverse speed, i.e. 1 and 4 mm/min, were analysed. No impact of the speed was reported.

The average values obtained during the tests were as follows: the yield point (yield stress), $R_{0.2}$ = 318 MPa, the tensile strength, $R_{m.}$ = 446 MPa, and the displacement percentage, A_5 = 33.9%. Using the averaged $\sigma(\varepsilon)$ curve, it was possible to determine the nominal normal stress σ and the longitudinal strain ε.

Determining the microstructural parameters required modelling the data from the tensile strength tests (GTN model) numerically. The averaged tensile strength curve was approximated using the following equation:

$$\frac{\sigma}{\sigma_0} = \left(\frac{\sigma}{\sigma_0} + \frac{3G}{\sigma_0} \bar{\varepsilon}_m^{pl} \right)^N \tag{10}$$

where:

σ – stress,

σ_0 – yield stress,

G – coefficient of transverse elasticity,

$\bar{\varepsilon}_m^{pl}$ – mean plastic strain,

N – strain-hardening exponent.

Table 2. Strength parameters of S235JR steel according to Equation (10)

σ_0 [MPa]	σ_m [MPa]	G [MPa]	N
318	446	80 000	0.183

The data obtained during tensile strength tests were numerically modeled basing on the equation of the approximate curve (10). The Gurson–Tvergaard–Needelman (GTN) damage model takes into account the nucleation and growth of inclusion-related voids. The initial void volume fraction f_0 was 0.0017 = 0.17 %.

The critical void volume fraction, f_c, above which the material strength decreases, was 0.06. This value coincides with the results obtained by other authors [31]. As suggested by Richelsen and Tvergaard [42], the critical value of the void volume fraction, f_c, is dependent on the initial void volume fraction f_0. It ranges from f_c = 0.04 at f_0 = 0.0 to f_c = 0.12 at f_0 = 0.06. The calculated value, f_c = 0.06, is consistent with the experimental results.

The value of the void volume fraction corresponding to the loss of strength f_F was 0.667.

The Tvergaard parameters were: q_1 = 1.5, q_2 = 1.0, and q_3 = 2.25. The volume fraction of the nucleated voids f_N was 0.04, the average nucleation (initiation) strain of inclusion-related voids ε_N was 0.3, and the standard deviation of the strain s_N was 0.05.

Table 3. Microstructural parameters of the modified GTN model of S235JR steel

f_0	f_c	f_F	q_1	q_2	q_3	f_N	ε_N	f_N
0.0017	0.06	0.667	1.5	1.0	2.25	0.04	0.3	0.05

The numerical calculations were performed using the program based on the Finite Element Method, Abaqus Explicit version 6.7. The elements were modelled as axially symmetrical components using standard 4-node CAX4R elements [43].

Figure 5 shows a tensile strength curve determined numerically in the form of the load F versus displacement l function for the GTN model parameters.

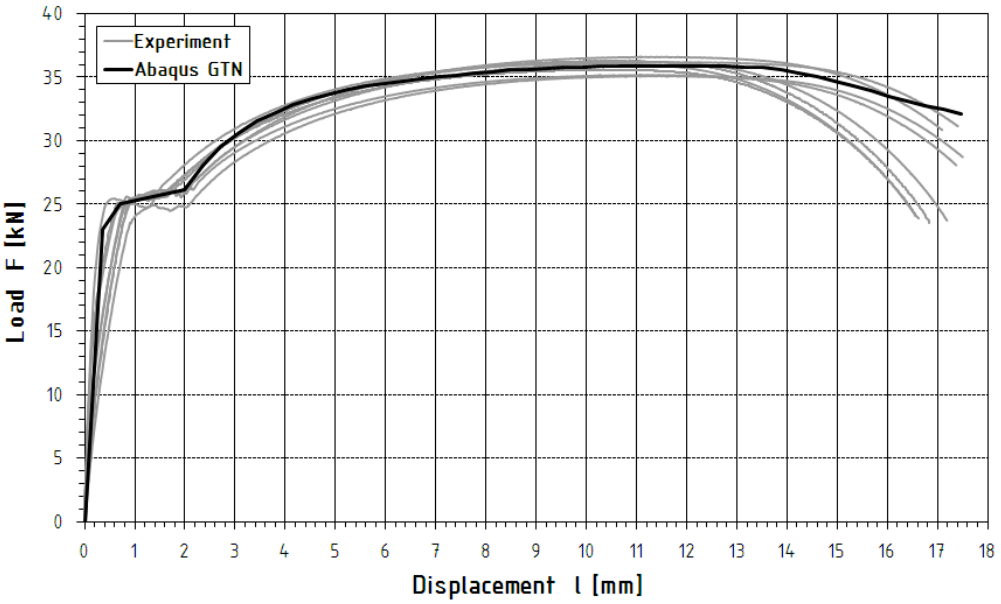

Fig. 5. Load-displacement $F(l)$ curves obtained through experiments and numerical analysis

4. Experimental and numerical modelling of load-carrying capacity and failure susceptibility in complex stress states

The analysis of load-carrying capacity and failure susceptibility was conducted using stretched ring-notched specimens with circular cross-sections for different notch radii ρ_0 (Figure 6).

The stress inside the specimens was calculated using the Bridgman analytical solution [44]. The triaxiality stress ratio $\sigma_m / \bar{\sigma}$ was determined as:

$$\frac{\sigma_m}{\bar{\sigma}} = \frac{1}{3} + \ln\left(\frac{r_0}{2\rho_0} + 1\right), \tag{11}$$

where:

$\sigma_m = (\sigma_{11}+\sigma_{22}+\sigma_{33})/3$ – mean stress,
$\overline{\sigma}$ – von Misses effective stress,
$2r_0$ – original minimum diameter,
ρ_0 – notch radius.

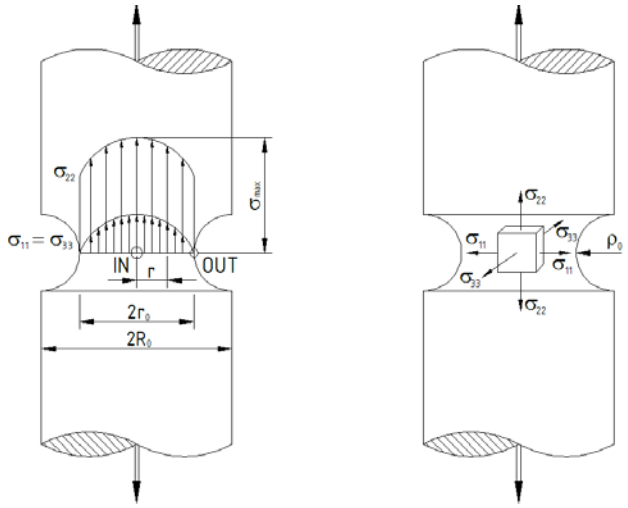

Fig. 6. Geometry and stress state components of a ring notched specimen

From relationship (11) it is clear that a change in the notch radius, ρ_0, has a significant effect on the stress state in the notch area. The analysis was conducted for elements with diameters $2R_0$ = 14.0 mm and $2r_0$ = 7.0 mm and notch radii ρ_0 ranging from 1.0 mm to 7.0 mm. It was possible to study the state of stress at different stress triaxiality ratios, ranging from $\sigma_m / \overline{\sigma}$ = 0.556 for ρ_0 = 7.0mm to $\sigma_m / \overline{\sigma}$ = 1.345 for ρ_0 = 1.0 mm (Table 4).

Table 4. Stress triaxiality ratio $\sigma_m / \overline{\sigma}$ for different notch radii

Notch radius	Stress triaxiality ratio
ρ_0 = 1.0mm	$\sigma_m / \overline{\sigma}$ = 1.345
ρ_0 = 1.5mm	$\sigma_m / \overline{\sigma}$ = 1.107
ρ_0 = 3.5mm	$\sigma_m / \overline{\sigma}$ = 0.739
ρ_0 = 7.0mm	$\sigma_m / \overline{\sigma}$ = 0.556

The load-carrying capacity analysis included tensile strength tests, during which specimens were subjected to static tension. The quantities measured were load F and displacement of points distributed symmetrically along the notch l, with the extensometer initial length being l_{0s} = 32.56 mm (Figure 7).

Two ranges of traverse speed were used: 1 and 4 mm/min. The speed was reported to have no effect on the results. The load vs. displacement curves are shown in Figures 10–13.

Fig. 7. View of a ring-notched round specimen subjected to tension in a complex stress state

The nature of the fracture (Figure 8) corresponds to the typical ductile failure, whose mechanism was described in the introduction and illustrated in Figure 2. The cracking resulted from the coalescence of voids through localized plastic strain. Macroscopically, the cracks were perpendicular to the maximum normal stress (tensile axis). In the central fracture area, there were numerous folds, which are attributable to the coalescence of voids due to slides down the planes inclined to the tensile axis at an angle of 30–45°. The cracks resulted from the slide and the coalescence of voids, with the slide occurring in the outer parts of the specimens. The cracks went along slide bands in the plane inclined to the tensile axis at an angle of 45°. For specimens with a high stress triaxiality ratio, at $\sigma_m / \overline{\sigma} > 1$ (where $\rho_0 = 1.0$ mm and $\rho_0 = 1.5$ mm, Figures 8a and b), the characteristic phenomenon was plasticity in a very small area surrounding the notch. For the other specimens (where $\rho_0 = 3.5$ mm and $\rho_0 = 7.0$ mm, Figs 8c and d), the plasticity was more visible; it extended from the bottom of the notch in the longitudinal direction, like in tensile strength tests conducted for smooth specimens.

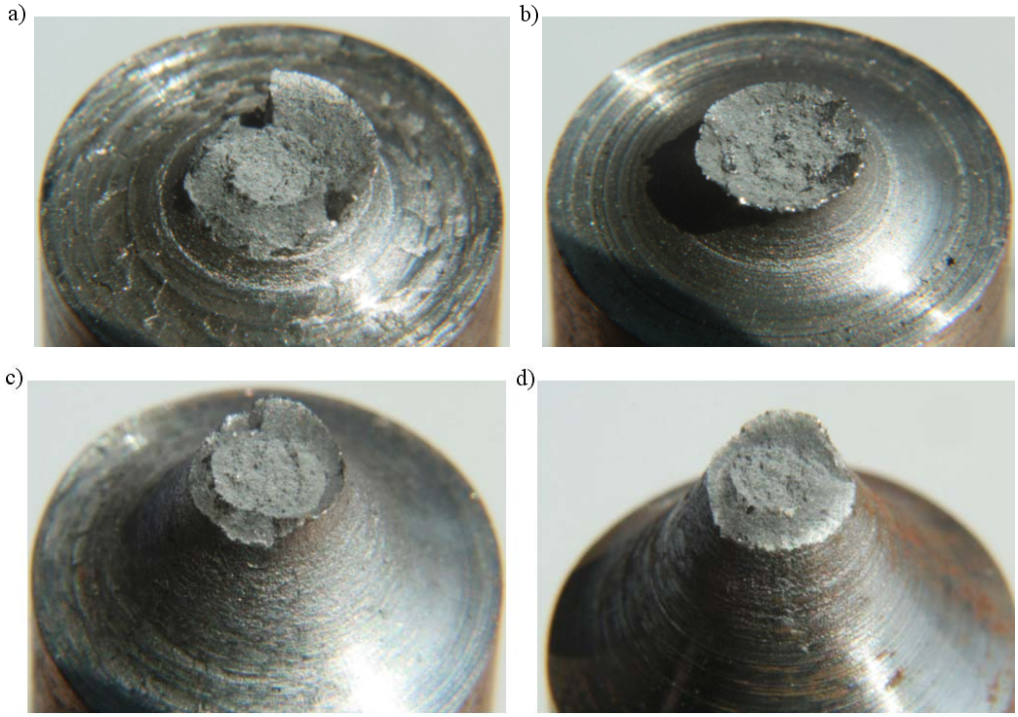

Fig. 8. Macrographs of fracture surfaces of specimens under tension in a complex stress state: a) ρ_0 = 1.0 mm, b) ρ_0 = 1.5 mm, c) ρ_0 = 3.5 mm, d) ρ_0 = 7.0 mm

The next stage of the analysis was numerical calculations. It was necessary to develop a procedure for modelling specimens by using the GTN model, verify the experimental results, and analyse the growth of microvoids and their effect on the load-carrying capacity.

The numerical calculations were performed using a program based on the Finite Element Method (Abaqus Explicit version 6.7). The elements modelled were the same as those used during the tensile strength tests. The ring-notched specimens with a circular cross-section were subjected to static tension in the complex stress state, the notch radius ρ_0 ranging from 1.0 mm to 7.0 mm. The modelling was performed for axially symmetrical standard 4-node CAX4R elements [42]. Because of the symmetry, the modeling was conducted only for half-specimens (Figure 9). The height of the numerical models corresponded to half of the extensometer length, i.e. 16.28 mm.

The Gurson-Tvergaard-Needleman (GTN) damage model required using the nonlinear explicit dynamic analysis. To compare the results, it was essential to perform numerical calculations based on the classic Huber-Misses model using a static analysis. The load-carrying capacity was defined by plotting the load F against displacement l (Figures 10–13).

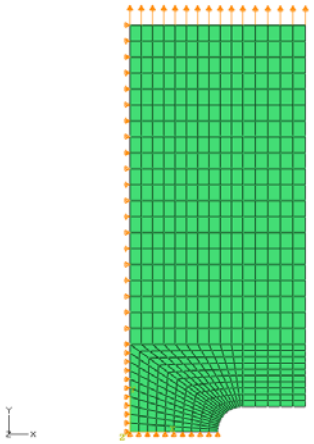

Fig. 9. Numerical model of a ring-notched element with a circular cross-section

The void growth was analysed basing on the changes in the void volume fraction that occurred during the plasticity process and the effect of voids on the stress state described by the stress triaxiality ratio $\sigma_m / \bar{\sigma}$. The relationship between the void volume fraction and the stress triaxiality ratio $\sigma_m / \bar{\sigma}$ in the function of displacement l was determined for a point inside a specimen designated as IN and for the bottom of the notch at a point designated as OUT (according to Figure 6).

As can be seen from the $F(l)$ curves plotted for the ring-notched specimens subjected to tension, the load F, which was determined by applying the GTN model and the non-linear explicit dynamic analysis, was lower than that obtained with the classic Huber-Misses model and the static analysis. It was found that the material porosity significantly affected the tensile strength and the load-carrying capacity.

It should be noted that the tensile strength curves obtained by applying the GTN model and the non-linear explicit dynamic analysis are consistent with the experimental results, and thus are closer to the real ones. This is not true about the results obtained by applying the HM model and the static analysis.

The GTN model assumes that for elements with the notch radius ρ_0 ranging from 1.0 mm to 3.5 mm, which corresponds to a maximum load, the numerical data are consistent with the experimental results. For a specimen with the notch radius equal to 7.0 mm, the values of load determined numerically were lower than those obtained experimentally (Figure 13). In a wider range, the numerically calculated values of the load F were lower than the real ones (Figures 10–13).

The $F(l)$ curves plotted for elements with $\rho_0 = 1.0$ mm and $\rho_0 = 1.5$ mm show that the maximum values of the load F (load-carrying capacity) were achieved at $l = 0.5$ mm (Figures 10 and 11). For the other elements with $\rho_0 = 3.5$ mm and $\rho_0 = 7.0$ mm, the load-carrying capacity was accomplished at $l = 0.68$ mm and $l = 0.85$ mm, respectively (Figures 12 and 13).

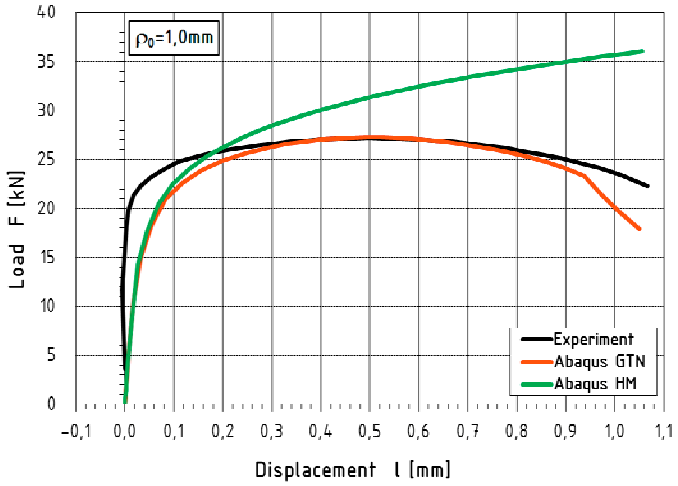

Fig. 10. Load-displacement $F(l)$ curves for a specimen with the notch radius $\rho_0 = 1.0$ mm

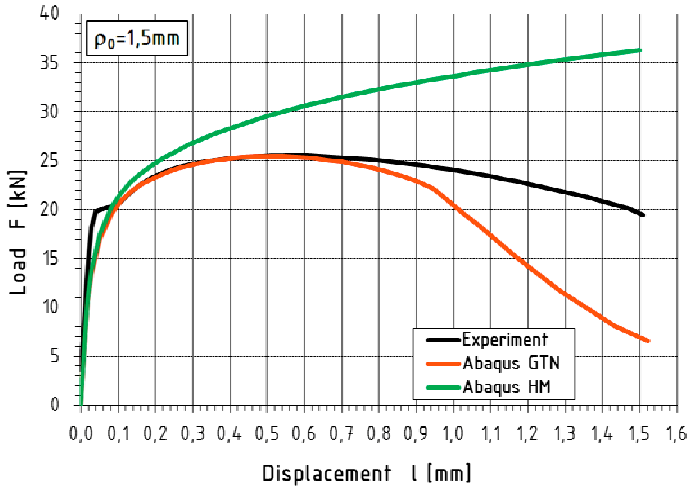

Fig. 11. Load-displacement $F(l)$ curves for a specimen with the notch radius $\rho_0 = 1.5$ mm

For each specimen, there was a fall in the load capacity followed by the element failure after the maximum strength was reached. This applies both to the experimental results and the numerical simulation data obtained by means of the GTN model. For elements with $\rho_0 = 1.0$ mm and $\rho_0 = 1.5$ mm and the resulting high stress triaxiality ratio, one can determine the point beyond which there occurs a sharp decrease in load corresponding to the displacement l equal to 0.94 mm. In the range from the maximum load-carrying capacity to the failure, the differences in load were bigger during the experiments than during the numerical calculations.

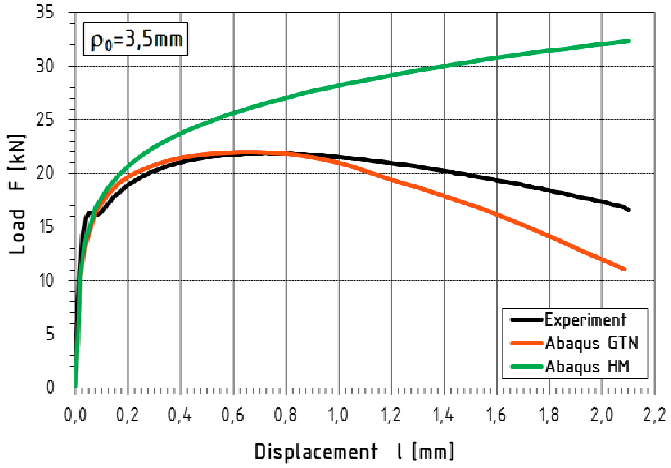

Fig. 12. Load-displacement $F(l)$ curves for a specimen with the notch radius $\rho_0 = 3.5$ mm

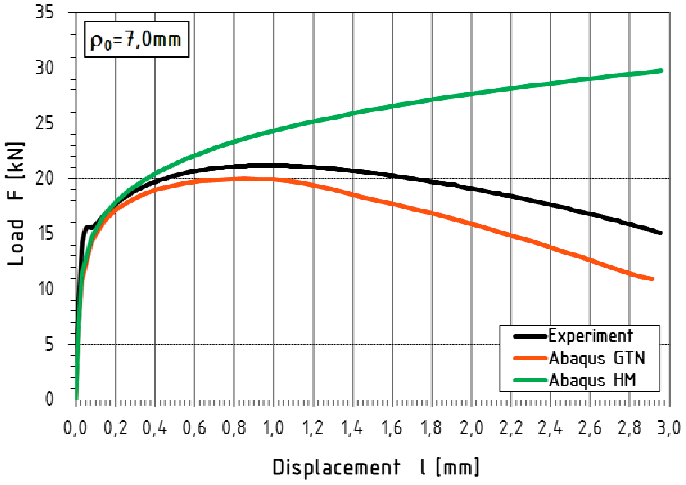

Fig. 13. Load-displacement $F(l)$ curves for a specimen with the notch radius $\rho_0 = 7.0$ mm

An increase in the void volume fraction was observed for the displacements corresponding to the maximum load-carrying capacity, i.e. $l = 0.5$ mm for specimens with $\rho_0 = 1.0$ mm and $\rho_0 = 1.5$ mm and $l = 0.68$ mm and $l = 0.85$ mm for specimens with $\rho_0 = 3.5$ mm and $\rho_0 = 7.0$ mm, respectively. Figures 14 and 18 illustrate the increase in the void volume fraction for specimens with the notch radius $\rho_0 = 1.0$ mm ($\sigma_m / \bar{\sigma} > 1$) and $\rho_0 = 3.5$ mm ($\sigma_m / \bar{\sigma} < 1$). The initial increase in the void volume fraction was particularly intensive in the outer part of the specimen (point OUT in Figure 14).

Beyond the maximum load-carrying capacity, there was a more rapid increase in the void growth rate, especially for elements with a higher stress triaxiality ratio, $\sigma_m / \overline{\sigma} > 1$ (Figure 14). When $\sigma_m / \overline{\sigma} > 1$, the more rapid increase in the void growth rate resulted from the considerable decrease in the load-carrying capacity; for elements with ρ_0 = 1.0 mm and ρ_0 = 1.5 mm, the displacement was l = 0.94 mm. Beyond that point, the growth of voids inside the specimen (point IN) was more rapid than outside (point OUT). During the process of further plasticity, the voids inside an element grew in number more intensively and rapidly (Figure 14). Figures 15a and b show maps of the void volume fraction for elements with the highest stress triaxiality ratio, i.e. $\sigma_m / \overline{\sigma}$ = 1.345 at ρ_0 = 1.0 mm. The map of the void volume fraction in Figure 15a corresponds to l = 0.94 mm, and accordingly, to a sudden drop in the load-carrying capacity. Figure 15b presents a map of the void volume fraction after that point was reached. In the first case, the highest void volume fraction was in the outer part (point OUT), while in the other case, the increase in voids was more visible in the inner part (point IN). It could thus be concluded that the rupture would go from the inside to the outside.

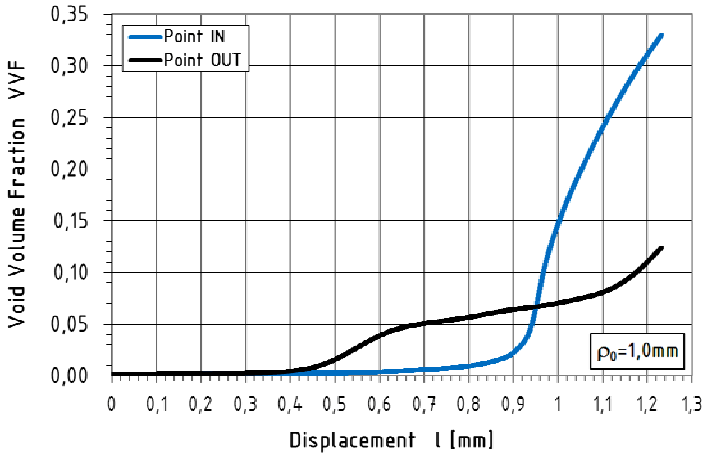

Fig. 14. Void volume fraction versus displacement curve for a specimen with ρ_0 = 1.0 mm

Another characteristic phenomenon observed during the numerical simulation was that the damage growth occurred in a very small volume of material, directly in the plane of the smallest cross-section near the notch bottom (Figures 15 and 19).

The phenomena described above are particularly strong for elements with a high stress triaxiality ratio, i.e. $\sigma_m / \overline{\sigma} > 1$. When $\sigma_m / \overline{\sigma} < 1$, that is for elements with ρ_0 = 3.5 mm and ρ_0 = 7.0 mm, the phenomena were less intensive. The void volume growth rate was lower for $\sigma_m / \overline{\sigma} < 1$ than for $\sigma_m / \overline{\sigma} > 1$. The phenomenon was reflected in the experimental results and the numerical simulations data. The specimens

with ρ_0 = 1.0 mm and ρ_0 = 1.5 mm were reported to fail much sooner. It is thus clear that the material failure caused, for instance, by an increase in the number of voids, will occur sooner if the stress traixiality ratio is high, $\sigma_m / \overline{\sigma} > 1$.

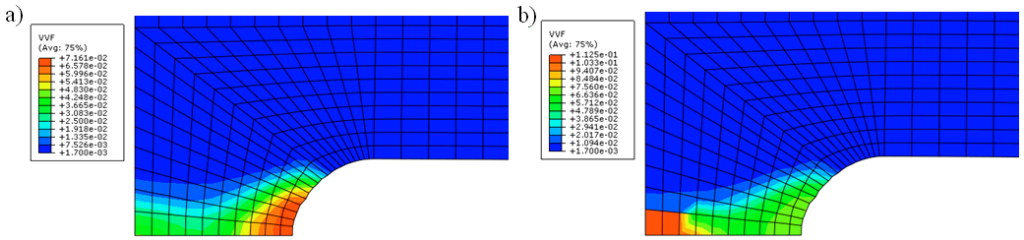

Fig. 15. Void volume fraction maps for a specimen with ρ_0 = 1.0 mm, a) l = 0.94 mm, b) l = 0.97 mm

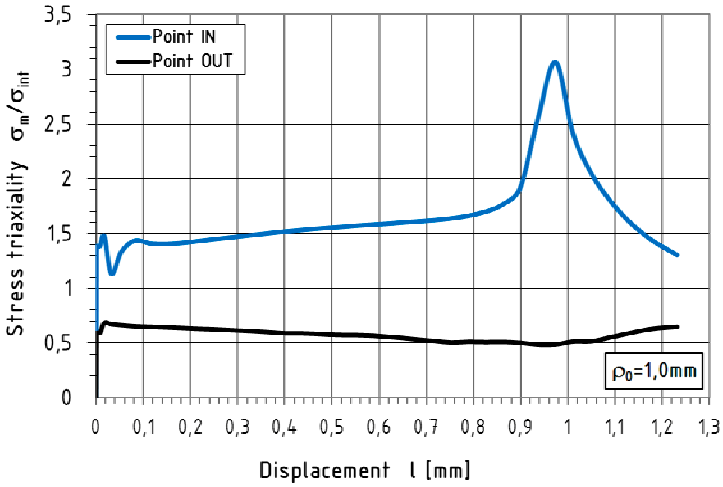

Fig. 16. Triaxiality stress ratio versus displacement curves for a specimen with ρ_0 = 1.0 mm

As can be seen, the increase in the void volume fraction affected the load-carrying capacity and strength of the specimens considerably. This influence was particularly visible when $\sigma_m / \overline{\sigma} > 1$. It can be concluded that for elements with $\sigma_m / \overline{\sigma} > 1$, the microstructural failure (void growth) was closely related to the changes in the stress state.

The void volume fraction at the moment of failure ranged between 20 and 45%. The value of 45% was obtained for elements with ρ_0 = 1.5 mm at test duration of 13s. For the other specimens, the value was in the range of 20–29%. The minimum void volume fraction was approximately 20%. It was possible to determine the criterion of failure basing on the GTN model. It should be noted that the result refers to one rate of

deformation. If the load conditions are different, the result may be different, too. It seems that the influence of the deformation rate on the rate and intensity of void growth needs to be analysed separately.

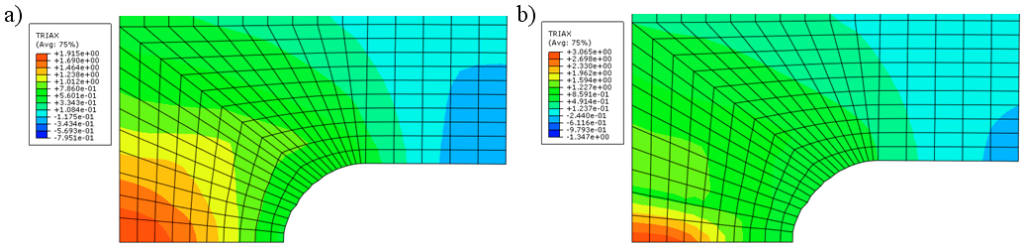

Fig. 17. Triaxiality stress ratio maps for a specimen with $\rho_0 = 1.0$ mm: a) $l = 0.90$ mm; b) $l = 0.97$ mm

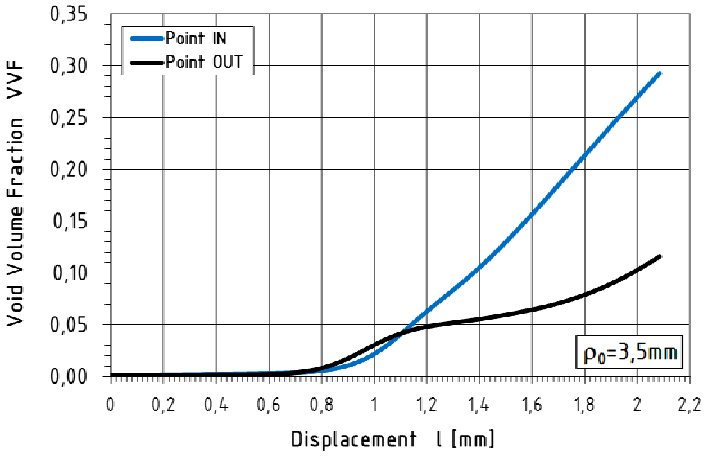

Fig. 18. Void volume fraction versus displacement curves for a specimen with $\rho_0 = 3.5$ mm

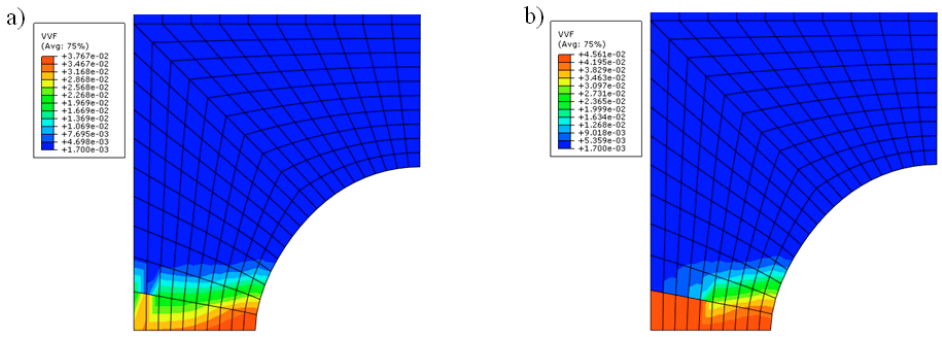

Fig. 19. Void volume fraction maps for a specimen with $\rho_0 = 3.5$ mm, a) $l = 1.05$ mm, b) $l = 1.12$ mm

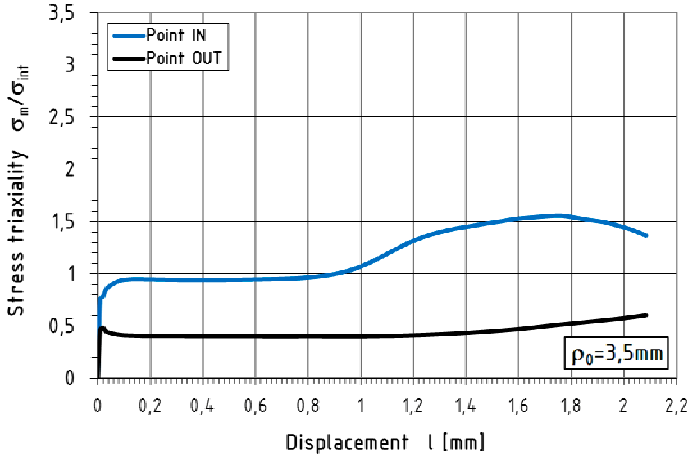

Fig. 20. Triaxiality stress ratio versus displacement curves for a specimen with $\rho_0 = 3.5$ mm

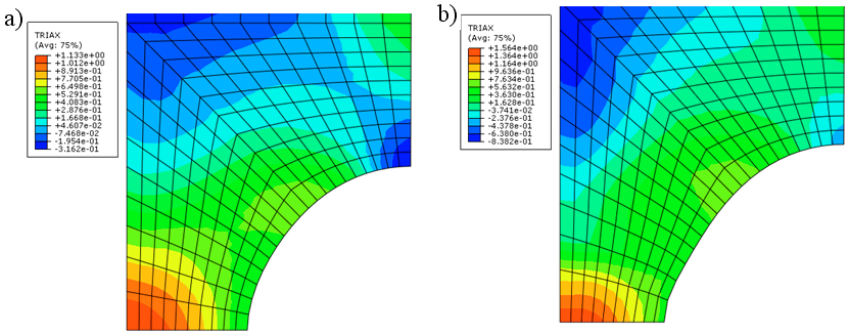

Fig. 21. Triaxiality stress ratio maps for a specimen with $\rho_0 = 3.5$ mm, a) $l = 1.05$ mm, b) $l = 1.76$ mm

Another objective of the study was to evaluate the impact of the stress state on the load-carrying capacity of elements and the material microdamage. The stress state was expressed as the stress triaxiality ratio, while the microdamage was defined by the increase in the void volume fraction. Prior to the rapid decline in the load-carrying capacity, there was a slight increase in the stress triaxiality ratio $\sigma_m / \overline{\sigma}$ in the inner part of the elements and a slight decrease of this ratio in the outer. This corresponds to l = 0–0.85 mm for elements with ρ_0 = 1.0 mm and ρ_0 = 1.5 mm. When l reached 0.85 mm, there was a significant increase in $\sigma_m / \overline{\sigma}$ in the inner part; it rose until $\sigma_m / \overline{\sigma} = 3.1$ at $l = 0.96$ mm for an element with $\rho_0 = 1.0$ mm. It is clear that the rapid decline in the load-carrying capacity and the rate of increase in the void volume fraction were related to the rapid change in the stress state reflected by a sudden increase in the stress triaxiality ratio in the inner part. In the analysed range, there was a slight

increase in $\sigma_m / \overline{\sigma}$ in the outer part of the elements. After the rapid decrease in the load capacity at $l > 0.96$ mm, there was a decrease in the stress triaxiality ratio in the inner part until $\sigma_m / \overline{\sigma} \approx 1.4$, which corresponded to the initial value of $\sigma_m / \overline{\sigma}$. Figures 17a and b show maps of the stress triaxiality ratio $\sigma_m / \overline{\sigma}$ for an element with $\rho_0 = 1.0$ mm at $l = 0.90$ mm and $l = 0.97$ mm.

Changes in the stress triaxiality ratio $\sigma_m / \overline{\sigma}$ coinciding with microstructural changes were observed also in elements with $\rho_0 = 3.5$ mm and $\rho_0 = 7.0$ mm; their intensity, however, was considerably smaller (Figures 20 and 21).

5. Final remarks and conclusions

The paper deals with the results of the load capacity analysis and the growth of microstructure damage taking the form of voids for elements made of S235JR steel subjected to complex stress states. The modified Gurson–Tvergaard–Needelman (GTN) model taking account of the material structure was used.

The objective of the study was to determine the standardized material parameters for S235JR steel by conducting a microstructural analysis and standard tensile strength tests with their numerical modelling. The parameters were obtained by means of the modified GTN model taking into account the steel structure.

The modified model was used for the numerical analysis of elements under the action of complex stress states, whose geometries were different from those of the standardized specimens. The numerical calculations including the analysis of maximum values and the criteria of failure for S235JR steel based on the modified GTN model and the development of microvoids.

Because of the extensive use of S235JR steel in the building industry in Poland, the results can be applied to various analyses and expertise with the aim of estimating the load-carrying capacity and the structural safety of elements.

The following are the conclusions drawn from the analysis results:

– By applying the modified GTN model, which takes into account the real microstructural parameters for S235JR steel elements, one is capable of estimating the failure loads resulting from plastic fracture.

– The tensile strength curves obtained by using the modified GTN model taking into consideration the real microstructural parameters and the non-linear explicit-type dynamic analysis were consistent with the experimental results, i.e. the real results, in contrast with the data obtained by means of the HM model and the static analysis.

– The parameters of the modified GTN model taking account of the real microstructural parameters of S235JR steel determined on the basis of the microstructural analysis, tensile strength tests and numerical analysis, were used to good effect during the analysis of elements subjected to complex stress states.

– Initially, the void growth was very intensive in the outer part of the specimens. After the maximum load-carrying capacity was reached, the rate of the void growth

was higher, especially for elements with a higher stress triaxiality ratio, i.e. $\sigma_m / \overline{\sigma} > 1$. When $\sigma_m / \overline{\sigma} > 1$, the increase in the void growth rate corresponded to the rapid fall in the element load capacity. Once the point was reached, the voids grew in number more rapidly in the central part of the elements rather than in the outer part. It can be assumed that the failure occurring in the central part is crucial to the load capacity of the whole element.

– An increase in the void volume fraction is observed in a very small volume of the material; it occurs in the plane of the smallest cross-section near the notch bottom.

– An increase in the void volume fraction affected the load-carrying capacity and strength of analysed elements. Effect was more visible for the elements with $\sigma_m / \overline{\sigma} > 1$. When $\sigma_m / \overline{\sigma} > 1$, the void growth was attributable to changes in the stress state.

– The specimens with the notch radius ρ_0 equal to 1.0 mm or 1.5 mm was reported to fail earlier than the other specimens. It can be assumed that failure caused, for instance, by an increase in the void growth, will occur more rapidly in elements with a high stress triaxiality ratio (i.e. $\sigma_m / \overline{\sigma} > 1$).

– The minimum void volume fraction of 20% corresponding to the element failure was determined by applying the modified GTN model, which took into consideration the real microstructural parameters. The value can be treated as a criterion of failure for the S235JR specimens subjected to complex stress states.

– By analyzing the damage which takes the form of voids, one is able to analyse the load-carrying capacity, and accordingly, the safety of structural elements. As failure is expected to occur once the void volume fraction reaches a critical value, it is possible to apply this procedure to analyse the failure states of structural elements made of S235JR steel basing on the modified GTN model taking account of the real microstructural parameters of this material.

– The modified GTN model, which takes account of the real microstructural parameters of S235JR steel, was used to analyse the growth of voids, and their number and location in an element. Basing on the results, it was possible to establish the weak points of the structure, i.e. areas particularly susceptible to loss of load-carrying capacity. The material structure was reported to be responsible for the load-carrying capacity of the whole element.

Acknowledgements

The research reported herein was conducted as part of Project R04 007 01 funded over the period 2006–2010 from education budget.

References

[1] Kachanov L.: *Time of the rupture process under creep conditions*, Izv. Akad Nauk SSSR, Otd. Tekh. Nauk, No. 8, 1958, pp. 26–31.

[2] Lemaitre J.: *How to use damage mechanics*, Nuclear Eng. and Design, Vol. 80, No. 2, 1984, pp. 233–245.
[3] Lemaitre J.: *A continuum damage mechanics model for ductile fracture*, J. Eng. Mat. and Technology, Vol. 107, No. 1, 1985, pp. 83–89.
[4] Murakami S., Proc. 2nd Int. Conference on Constitutive Laws for Engineering Materials, ed. Desai, C.S. and Krempl E., Elsevier, 1987.
[5] Gurson A.L.: *Continuum theory of ductile rupture by void nucleation and growth: Part I – yield criteria and flow rules for porous ductile materials*, J. Eng. Mat. and Tech., Vol. 99, No. 1, 1977, pp. 2–15.
[6] Suquet P.: *Plasticité et homomogénéisation*, Thése Doctorat d'Etat, Univ. Paris VI, 1982.
[7] Cordebois J.P., Sidoroff F.: *Endommanegament anisotrope en elasticité et plasticité*, J. Méc. Théor. Appl., Numero Spécial, 1982, pp. 45–60.
[8] Tvergaard V.: *Material failure by void coalescence in localized shear bands*, DCAMM Report No. 221, Techn. Univ. of Denmark, Lyngby, 1981, pp. 1–26.
[9] Tvergaard V.: *Numerical study of localization in a void sheet*, DCAMM Report No. 337, Techn. Univ. of Denmark, Lyngby, 1988, pp. 1–19.
[10] Rousselier G.: *Finite deformation constitutive relations including ductile fracture damage*, IUTAM Symp. on Three-dimensional constitutive relations and ductile fracture, Eds. Dourdan, Nemat-Nasser, North-Holland, 1981, pp. 331–355.
[11] Rousselier G.: *Les modéles de rupture ductile et leurs possibilités actuelles dans le cadre de l'approche locale de la rupture*, Moret-sur-Loing, 1986, France.
[12] Dragon A., Chihab A.: *Quantifying of ductile fracture damage evolution by homogenization approach*, SMiRT 8, Brussels, 1985.
[13] Chow C.L., Lu T.J.: *An analytical and experimental study of mixed-mode ductile fracture under nonproportional loading*, Int. J. Damage Mech., Vol. 1, No. 2, 1992, pp. 191–236.
[14] Voyiadjis G.Z., Kattan P.I.: *A plasticity-damage theory for large deformation of solids, Part I: theoretical formulation*, Int. J. Eng. Sci., Vol. 30, No. 9, 1992, pp. 1089–1108.
[15] Murzewski J.: *Brittle and ductile damage of stochastically homogeneous solids*, Int. J. Damage Mech., Vol. 1, No. 3, 1992, pp. 276–289.
[16] Mou Y.H., Han R.P.S.: *Damage evolution in ductile materials*, Int. J. Damage Mech, Vol. 5, No. 3, 1996, pp. 241–258.
[17] Saanouni K., Foster C., Ben Hatira F: *On the anelastic flow with damage*, Int. J. Damage Mech., Vol. 3, No. 2, 1994, pp. 140–169.
[18] Taher S.F., Baluch M.H., Al-Gadhib A.H.: *Towards a canonical elastoplastic damage model*, Eng. Fracture Mech., Vol. 48, No. 2, 1994, pp. 151–166.
[19] Tvergaard V.: *Influence of voids on shear band instabilities under plane strain condition*, Int. J. Fracture Mech., Vol. 17, No. 4, 1981, pp. 389–407.
[20] Tvergaard V., Needleman A.: *Analysis of the cup cone fracture in a round tensile bar*, Acta Metall., Vol. 32, No. 1, 1984, pp. 157–169.
[21] Needleman A., Tvergaard V.: *Analysis of the ductile rupture in notched bars*, J. Mech. and Physics Solids, Vol. 32, No. 6, 1984, pp. 461–490.
[22] Terlinck D., Zok F., Embury J.D., Ashby M.F.: *Fracture mechanism maps in stress space*, Acta Metall., Vol. 36, No. 5, 1998, pp. 1213–1228.
[23] Aoki S., Amaya K., Sahashi M., Nakamura T.: *Identification of Gurson's material constants by using Kalman filter*, Comp. Mech., Vol. 19, No. 6, 1997, pp. 501–506.

[24] Corigliano A., Mariani S., Orsatti B.: *Identification of Gurson-Tvergaard material model parameters via Kalman filtering technique. I. Theory*, Int. J. Fracture, Vol. 104, No. 4, 2000, pp. 349–373.
[25] Nowak Z., Stachurski A.: *Identification of an augmented Gurson model parameters for plastic porous media*, Foundation of Civil and Environmental Engineering, No. 2, 2002, pp. 141–150.
[26] Nowak Z.: *Metoda identyfikacji w mechanice materiałów ciągliwych*, IPPT PAN, Warszawa, 2006.
[27] Springmann M., Kuna M.: *Identification of material parameters of the Gurson-Tvergaard-Needleman model by combined experimental and numerical techniques*, Comp. Mat. Sc., Vol. 32, No. 3–4, 2005, pp. 544–552.
[28] Chhibber R., Arora N., Gupta S.R., Dutta B.K.: *Estimation of Gurson material parameters in bimetallic weldments for the nuclear reactor heat transport piping system*, Jour. Mech. Eng. Sc., Vol. 222, No. 12, 2008, pp. 2331–2349.
[29] Hayhurst D., Trąmpczyński W., Leckie F.: *On the role of cavity nucleation in creep deformation and fracture*, Acta Metall., Vol. 31, No. 10, 1983, pp. 1537–1542.
[30] Biel-Gołaska M., Gołaski L.: *Modelowanie procesu pękania odlewów kolikowych i cienkościennych ze stopu Al-Si poddanych obciążeniom dynamicznym*, Projekt badawczy Nr PB 1037/T08/95/09, Instytut Odlewnictwa, Kraków, 1998.
[31] Lachowski J., Biel-Gołaska M.: *Symulacja odkształcania plastycznego i ewolucji uszkodzeń w przestrzennych stanach obciążenia*, VII Krajowa konferencje Mechaniki Pękania, Kielce-Cedzyna, 23–25 IX 1999, Zeszyty Naukowe Politechniki Świętokrzyskiej, Kielce, 1999, pp. 261–268.
[32] Biel-Gołaska M., Gołaski L., Lachowski J., Żuczek R.: *Analiza rozwoju uszkodzeń w stopach odlewniczych*, Raport KBN, Nr 8008/00, Instytut Odlewnictwa, Kraków, 2000.
[33] Hang Z.L., Thaulow C., Ødegård J.: *A complete Gurson model approach for ductile fracture*, Eng. Fract. Mech., Vol. 67, No. 2, 2000, pp. 155–168.
[34] Reusch F., Svendsen B., Klingbeil: *Local and non-local Gurson-based ductile damage and failure modelling a large deformation*, European J. of Mech. A/Solids, Vol. 22, No. 6, 2003, pp. 779–792.
[35] Hashemi S.H., Howard I.C., Yates J.R., Andrews R.M.: *Micro-mechanical damage modelling of notched bar testing of modern line pipe steel*, The 15th European Conference of Fracture – *Advanced fracture mechanics for life and safety*, Stockholm, August 11–13, 2004, p. 8.
[36] Münlich U., Brocks W.: *Regularization behaviour of nonlocal Gurson-type model*, The 15th European Conference of Fracture – *Advanced fracture mechanics for life and safety*, Stockholm, August 11–13, 2004, p. 8.
[37] Samal M.K., Seidenfuss M., Roos E., Dutta B.K., Kushwaha H.S.: *A mesh-independent Gurson–Tvergaard–Needleman damage model and its application in simulating ductile fracture behaviour*, J. Mech. Eng. Sc., Vol. 223, No. 2, 2008, pp. 283–292.
[38] Cricrì G.: *Consistent use of the Gurson-Tvergaard damage model for the R-curve calculation*, Convegno Nazionale IGF XX, Torino, 2009, pp. 138–150.
[39] J. Pastor, Ph. Thoré.: *Gurson model for porous pressure sensitive materials*, D. Weichert, A. Ponter (eds.), Limit States of Materials and Structures, Springer Science+Business Media B.V., 2009.

[40] *Określenie struktury materiałów (pobranych z konstrukcji) analiza porównawcza z parametrami stali wzorcowej*, Raport z badań w ramach projektu *Opracowanie oraz wstępna weryfikacja procedury diagnozowania metodą emisji akustycznej konstrukcji metalowych ze szczególnym uwzględnieniem mostów stalowych*, Politechnika Warszawska, Wydział Inżynierii Materiałowej, Warszawa, 2008.
[41] PN-EN 1002-1, *Metale. Próba rozciągania*. Część 1: *Metoda badania w temperaturze otoczenia*.
[42] Richelsen A.B, Tvergaard V.: *Dilatant plasticity or upper bound estimates for porous ductile solids*, Acta Metall. Mater., Vol. 42, No. 8, 1994, pp. 2561–3577.
[43] *ABAQUS Analysis user's manual, Version 6.7*, ABAQUS, Inc. and Dassault Systèmes, 2007.
[44] Bridgman P.W.: *Studies in large flow and fracture*, McGraw-Hill, New York, 1952.

Analiza nośności elementów pracujących w złożonych stanach naprężenia z uwzględnieniem wpływu uszkodzeń miktrostrukturalnych

W artykule przedstawiono wyniki analizy nośności elementów wykonanych ze stali S235JR pracujących w złożonych stanach naprężenia z uwzględnieniem wpływu uszkodzeń mikrostrukturalnych. Opracowano zmodyfikowany model Gursona–Tvergaarda–Needelmana (GTN) dla stali S235JR poprzez wykonanie badań mikrostrukturalnych, przeprowadzenie normowych prób rozciągania oraz ich modelowane numeryczne. Zmodyfikowany model GTN zastosowano w analizie numerycznej elementów pracujących w złożonych stanach naprężeń. Stwierdzono zgodność uzyskanych wyników w stosunku do rezultatów badań wytrzymałościowych. Opisano sposób prowadzenia obliczeń numerycznych wraz z analizą możliwych do uzyskania wyników oraz określono kryteria zniszczenia stali S235JR w oparciu o zmodyfikowany model GTN i rozwój mikrouszkodzeń.

ARCHIVES OF CIVIL AND MECHANICAL ENGINEERING

Vol. X 2010 No. 2

Analytical solution of forced-convective boundary-layer flow over a flat plate

H. MIRGOLBABAEI
School of Mechanic, Islamic Azad University, Jouybar Branch, Jouybar, Iran.

A. BARARI, L.B. IBSEN
Department of Civil Engineering, Aalborg University, Sohngårdsholmsvej 57, 9000 Aalborg, Aalborg, Denmark.

M.G. ESFAHANI
Department of Civil Engineering, Babol Noshirvani University of Technology, Babol, Iran.

In this letter, the problem of forced convection heat transfer over a horizontal flat plate is investigated by employing the Adomian Decomposition Method (ADM). The series solution of the nonlinear differential equations governing on the problem is developed. Comparison between results obtained and those of numerical solution shows excellent agreement, illustrating the effectiveness of the method. The solution obtained by ADM gives an explicit expression of temperature distribution and velocity distribution over a flat plate.

Keywords: *convection heat transfer, nonlinear equations, Adomian decomposition method, numerical method (NM)*

1. Introduction

Most scientific problems such as heat transfer are inherently of nonlinearity. We know that except a limited number of these problems, most of them do not have analytical solutions. Therefore, these nonlinear equations should be solved by using other methods. Some of them are solved by using numerical techniques and some of them are solved by using perturbation method. Since there are some limitations with the common perturbation method, and also because the basis of the common perturbation method is upon the existence of a small parameter, developing the method for different applications is very difficult. Most boundary-layer models can be reduced to systems of nonlinear ordinary differential equations which are usually solved by numerical methods. It is however interesting to find solutions to boundary layer problems using analytical approach. Analytical methods have significant advantages over numerical methods in providing analytic, verifiable, rapidly convergent approximation. The Adomian decomposition method based on series approximation is the newly developed method for strongly nonlinear problems. The Homotopy Perturbation Method uses functions to obtain series solutions to boundary-layer equations [1–6] while the

series in ADM [7] are derived from functions consisting of terms corresponding to the initial conditions. The analytic ADM has been proven successful in solving a wide class of nonlinear differential equations [7–13]. Hashim [8] applied ADM to the classical Blasius' equation. Wazwaz [14] used ADM to solve the boundary layer equation of viscous flow due to a moving sheet. Awang Kechil and Hashim [15] extended the applicability of ADM to obtain approximate analytical solution of an unsteady boundary layer problem over an impulsively stretching sheet. The first application of ADM to a 2-by-2 system of nonlinear ordinary differential equations of free-convective boundary layer equation was presented by Awang Kechil and Hashim [16]. Hayat et al. [17] studied the MHD flow over a nonlinearly stretching sheet by employing the Modified Adomian Decomposition Method.

In this paper, we revisit the steady two-dimensional laminar forced convection in a flow of viscous fluid against a flat plate with uniform wall temperature. Fluid is assumed to have constant properties. In this letter, we are interested in applying ADM to obtain an approximate analytical solution of this problem and the results obtained will be validated by those of numerical simulation.

2. Governing equations

Consider steady flow, with constant free stream velocity u_∞ without turbulence over a semi-infinite flat plate aligned with the flow. All fluid properties are considered to be constant. The continuity, Navier–Stokes, and energy equations of this flow are as follows [16]:

$$\frac{\partial u}{\partial x}+\frac{\partial v}{\partial y}=0, \tag{1}$$

$$u\frac{\partial u}{\partial x}+v\frac{\partial u}{\partial y}=-\frac{1}{\rho}\frac{dP}{dx}+\upsilon\frac{\partial^2 u}{\partial x^2}, \tag{2}$$

$$u\frac{\partial T}{\partial x}+v\frac{\partial T}{\partial y}=\alpha\frac{\partial^2 T}{\partial y^2}, \tag{3}$$

with following boundary conditions:

$$T=0 \text{ at } y=0, \tag{4a}$$

$$T\to T_\infty \text{ when } y\to\infty, \tag{4b}$$

$$T=T_\infty \text{ at } x=0, \tag{4c}$$

$u = 0, \quad v = 0$ at $y = 0$, (4d)

$u = u_\infty$ at $x = 0$, (4e)

$u \to u_\infty$ when $y \to \infty$. (4f)

The solution to the momentum equation is decoupled from the energy solution. However, the solution of the energy equation is still linked to the momentum solution. The following dimensionless variables are introduced in the transformation:

$$\eta = \frac{y}{\sqrt{x}} Re_x^{0.5}, \tag{5}$$

$$\theta(\eta) = \frac{T - T_\infty}{T_w - T_\infty}. \tag{6}$$

The Reynolds number is defined as:

$$Re = \frac{u_\infty x}{\upsilon}. \tag{7}$$

Using Equations (1) through (6), the governing equations can be reduced to two equations where *f is* a function of the similarity variable (η) [18]:

$$f''' + \frac{1}{2} ff'' = 0, \tag{8a}$$

$$\theta'' + \frac{Pr}{2} f\theta' = 0, \tag{8b}$$

where f is related to the u velocity by [18]:

$$f' = \frac{u}{u_\infty}. \tag{9}$$

The reference velocity is the free stream velocity of forced convection. The boundary conditions are obtained from the similarity variables. For the forced convection case [18]:

$$f(0) = 0, \quad f'(0) = 1, \quad \theta'(0) = 1, \quad f'(\infty) = 1, \quad \theta(\infty) = 0, \tag{10}$$

3. Adomian decomposition method

We follow the standard procedure of ADM [7] by introducing two linear differential operators $L_1 = d^3/d\eta^3$ and $L_2 = d^2/d\eta^2$ with inverse operators $L_1^{-1}(\cdot) = \int_0^\eta \int_0^\eta \int_0^\eta (\cdot)\mathrm{d}t\,\mathrm{d}t\,\mathrm{d}t$ and $L_2^{-1}(\cdot) = \int_0^\eta \int_0^\eta (\cdot)\mathrm{d}t\,\mathrm{d}t$. Thus, Equation (8) in operator form,

$$L_1(f) = -\frac{1}{2} ff'' \tag{11}$$

$$L_2(\theta) = -\frac{Pr}{2} f\theta' \tag{12}$$

Applying the inverse operators on Equations (11) and (12) and let $f''(0) = \alpha_1$, $\theta'(0) = \alpha_2$, we obtain,

$$f = \frac{1}{2}\alpha_1\eta^2 + \frac{1}{2} L_1^{-1}(P(f)), \tag{13}$$

$$\theta = 1 + \alpha_2\eta + \frac{Pr}{2} L_2^{-1}(Q(f,\theta)), \tag{14}$$

where the nonlinear terms in Equations (13) and (14),

$$P(f) = ff'', \tag{15}$$

$$Q(f,\theta) = f\theta', \tag{16}$$

and their respective decompositions,

$$P(f) = \sum_{i=0}^{\infty} A_i, \tag{17}$$

$$Q(f,\theta) = \sum_{i=0}^{\infty} E_i, \tag{18}$$

A_i, E_i are so-called Adomian polynomials [7], given by

$$A_i = \frac{1}{i!}\left[\frac{d^i}{d\lambda^i} P\left(\sum_{j=0}^{\infty} \lambda^j f_j\right)\right]_{\lambda=0}, \qquad i \geq 0. \tag{19}$$

This yields

$$A_0 = f_0 f_0'', \tag{20}$$

$$E_0 = f_0 \theta_0', \tag{21}$$

and for $i \geq 1$

$$A_i = \sum_{m=0}^{i} f_m f_{i-m}'', \tag{22}$$

$$E_i = \sum_{m=0}^{i} f_m \theta_{i-m}', \tag{23}$$

In ADM [14], f and θ are defined as infinite series,

$$f = \sum_{i=0}^{\infty} f_i \ (\eta), \tag{24}$$

$$\theta = \sum_{i=0}^{\infty} \theta_i \ (\eta). \tag{25}$$

Substituting Equations (17) and (18) and Equations (24) and (25) into Equations (13) and (14), we obtain

$$\sum_{i=0}^{\infty} f_i(\eta) = \frac{1}{2}\alpha_1 \eta^2 - \frac{1}{2} L_1^{-1}\left(\sum_{i=0}^{\infty} A_i \right), \tag{26}$$

$$\sum_{i=0}^{\infty} \theta_i(\eta) = 1 + \alpha_2 \eta - \frac{Pr}{2} L_2^{-1}\left(\sum_{i=0}^{\infty} E_i \right), \tag{27}$$

and the individual terms for f and θ are obtained from the recursive relations

$$f_0 = \frac{1}{2}\alpha_1 \eta^2, \tag{28}$$

$$\theta_0 = 1 + \alpha_2 \eta, \tag{29}$$

$$f_{i+1} = -\frac{1}{2} L_1^{-1}(A_i), \qquad i \geq 0, \tag{30}$$

$$\theta_{i+1} = -\frac{Pr}{2} L_2^{-1}(E_i), \qquad i \geq 0, \tag{31}$$

For practical numerical computation, we will compute the j-term approximation of $f(\eta)$, $\theta(\eta)$ which are $\phi_j(\eta) = \sum_{i=0}^{j-1} f_i$, $\psi_j(\eta) = \sum_{i=0}^{j-1} \theta_i$, respectively, as the j-term approximations converge to the true series as j approaches infinity.

4. Results and discussion

The Adomian polynomials (20–23) and the recursive relations (28–31) are then coded in the Maple environment computer package with the controlling significant digits set to 11. We obtain 10-term approximation to both f and θ given by $\phi_{10}(\eta) = \sum_{i=0}^{9} f_i$, and $\psi_{10}(\eta) = \sum_{i=0}^{9} \theta_i$, respectively, but for lack of space, only the first 3 terms produced from (28–31) are given below:

$$f_0(\eta) = \frac{1}{2}\alpha_1 \eta^2, \tag{32}$$

$$f_1(\eta) = -\frac{1}{240}\alpha_1^2 \eta^5, \tag{33}$$

$$f_2(\eta) = \frac{11}{161280}\alpha_1^3 \eta^8, \tag{34}$$

$$\theta_0(\eta) = \alpha_2 \eta + 1, \tag{35}$$

$$\theta_1(\eta) = -\frac{\mathrm{Pr}}{48}\alpha_1 \alpha_2 \eta^4, \tag{36}$$

$$\theta_2(\eta) = \frac{11}{20160}\mathrm{Pr}\,\alpha_1^2 \alpha_2 \eta^7, \tag{37}$$

The undetermined values of α_1 and α_2 are calculated from the boundary conditions at infinity in (10). The difficulty at infinity is overcome by employing the diagonal

Padé approximants [19] that approximate $f'(\eta)$ and $\theta(\eta)$ using $\phi_{10}(\eta)$ and $\psi'_{10}(\eta)$, respectively. The numerical results of α_1 and α_2 from $\lim_{\eta\to\infty}\phi'_{10}=1$ and $\lim_{\eta\to\infty}\psi_{10}=0$ for selected m in the range from 8 to 11 are presented in Table 1 for Pr = 1. Since Equation (8) can not be easily solved by the analytical method; Equation (8) is, therefore, solved by the numerical method using the software MAPLE whose results are given in Tables 2 and 3, and also the consequent results of the numerical and Adomian Decomposition are compared in Figures 1, 2 and 3. As you can see in Pr = 1, the ADM has a high accuracy.

Table 1. Numerical values of $f''(0)$, $\theta'(0)$, for Pr = 1

	[8.8]	[9.9]	[10.10]	[11.11]	Exact
α_1	0.2683198	0.44927	0.3293037	0.3293037	0.3293037
α_2	–0.2797056	–0.426513	–0.3487661	–0.3487661	–0.3487661

Table 2. The results of ADM, HPM and NM for $f(\eta)$, $f'(\eta)$ if Pr = 1

	$f(\eta)$			$f'(\eta)$	
η	ADM	NM		ADM	NM
0	0	0		0	0
0.2	0.0065859	0.0066412		0.0658571	0.0664077
0.4	0.0263396	0.0266762		0.1316636	0.1327641
0.6	0.0592395	0.0597215		0.1972899	0.1989372
0.8	0.1052295	0.1061082		0.2625216	0.2647094
1	0.1642024	0.1655717		0.3270638	0.32978
1.2	0.2359847	0.2379487		0.3905487	0.3937761
1.4	0.3203229	0.3229819		0.4525474	0.4562617
1.6	0.4168731	0.4203207		0.5125869	0.5167567
1.8	0.525194	0.529518		0.5701715	0.5747581
2	0.6447451	0.6500243		0.6248074	0.6297657
2.2	0.7748894	0.7811933		0.6760307	0.6813103
2.4	0.9149026	0.9222901		0.7234349	0.7289819
2.6	1.0639869	1.0725059		0.7666961	0.772455
2.8	1.2212899	1.2309773		0.8055934	0.8115096
3	1.3859262	1.3968082		0.8400224	0.8460444
3.2	1.5570018	1.5690949		0.8699999	0.8760814
3.4	1.7336381	1.7469501		0.89565596	0.9017612
3.6	1.9149935	1.9295251		0.9172393	0.9233296
3.8	2.1002831	2.1160298		0.9350592	0.9411181
4	2.2887911	2.3057464		0.9494855	0.9555182
4.2	2.4798731	2.4980396		0.9608389	0.966957
4.4	2.6729204	2.6923609		0.969051	0.9758708
4.6	2.8671706	2.888248		0.9722134	0.9826835
4.8	3.0608776	3.0853206		0.9815741	0.9877895
5	3.2479336	3.2832736		0.9896845	0.9915419

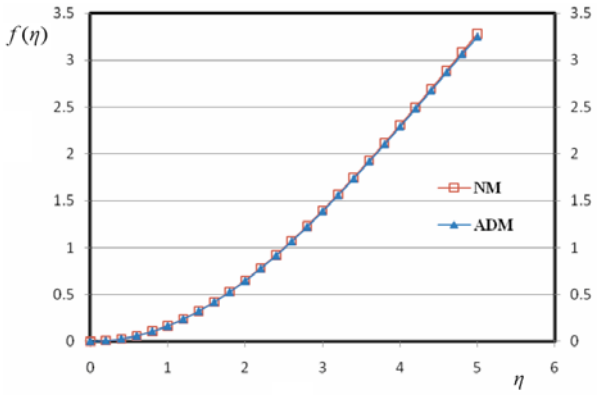

Fig. 1. The comparison of the answers resulted by *ADM* and *NM* for $f(\eta)$

Table 3. The results of ADM, HPM and NM for $\theta(\eta)$ if $Pr = 1$

η	ADM	NM	η	ADM	NM
0	1	1	2.6	0.2333038	0.2275449
0.2	0.9341428	0.9335922	2.8	0.1944065	0.1884903
0.4	0.8683363	0.8672358	3	0.1599775	0.1439554
0.6	0.80271	0.8010627	3.2	0.13012	0.1239183
0.8	0.7374783	0.7352908	3.4	0.1043403	0.0882386
1	0.6729361	0.6702199	3.6	0.0827606	0.0666702
1.2	0.6094512	0.6062238	3.8	0.0649412	0.0588819
1.4	0.5474525	0.5437381	4	0.0505144	0.0314817
1.6	0.487413	0.4832432	4.2	0.03916103	0.0330429
1.8	0.4298284	0.4252418	4.4	0.0309489	0.0241292
2	0.3751925	0.3702342	4.6	0.0277865	0.0173165
2.2	0.3239692	0.3186896	4.8	0.0186443	0.0122105
2.4	0.276565	0.271018	5	0.01264024	0.0084581

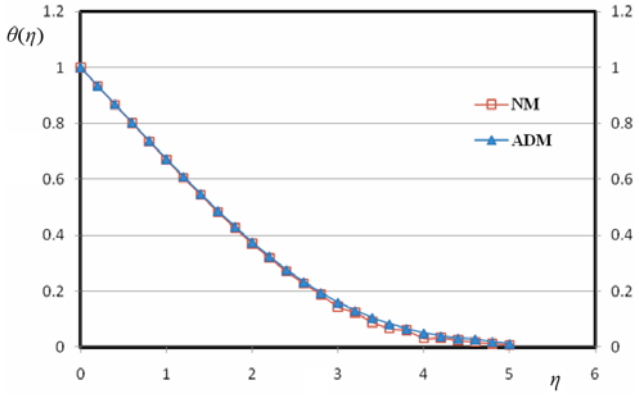

Fig. 2. The comparison of the answers resulted by *ADM* and *NM* for $\theta(\eta)$

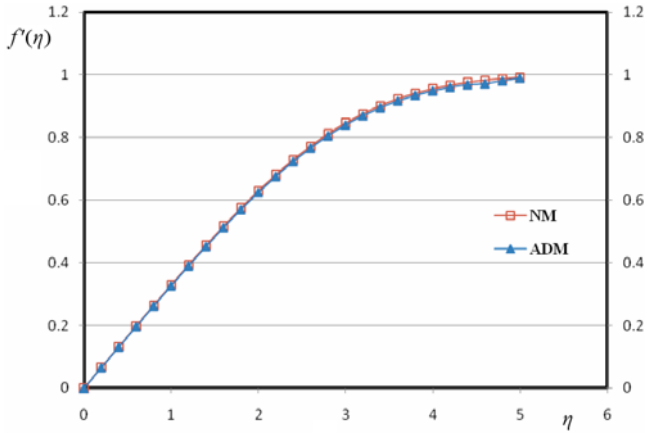

Fig. 3. The comparison of the answers resulted by *ADM* and *NM* for $f'(\eta)$

5. Conclusions

In this letter, Adomian Decomposition Method has been successfully applied to natural convection heat transfer problem with specified boundary conditions. The obtained solutions are compared with ones from numerical method and Homotopy Perturbation Method. The excellent agreement of the ADM solutions and the exact solutions shows the reliability and the efficiency of the method. This new method accelerated the convergence to the solutions. The ADM combined with the Padé approximant provide efficient alternative tools in solving nonlinear models.

Nomenclature

g – gravitational force
v – velocity component in the y direction
ADM – Adomian Decomposition Method
x – dimensional vertical coordinate
HPM – Homotopy Perturbation Method
y – dimensional horizontal coordinate
NM – numerical method
P – pressure
Pr – Prandtl number
P – density
T – temperature
T_W – temperature imposed on the plate
v – kinematic viscosity
T_∞ – local ambient temperature
α – thermal diffusivity
u – velocity component in the x direction
θ – dimensionless temperature

References

[1] Ganji D.D., Rajabi A., Taherian H.: *Application of homotopy perturbation method in nonlinear heat conduction and convection equations*, Physics Letters A, Vol. 360, No. 4–5, 2007, pp. 570–573.

[2] Fouladi F., Hosseinzadeh E., Barari A., Domairry G.: *Highly nonlinear temperature-dependent fin analysis by variational iteration method*, Heat Transfer Research, Vol. 41, No. 2, 2010, pp. 155–165.

[3] Miansari M. O., Miansari M. E., Barari A., Domairry G.: *Analysis of Blasius equation for flat-plate flow with infinite boundary value*, International Journal for Computational Methods in Engineering Science and Mechanics, Vol. 11, No. 2, 2010, pp. 79–84.

[4] Ganji D.D., Mirgolbabaei H., Miansari Me., Miansari Mo.: *Application of homotopy perturbation method to solve linear and non-linear systems of ordinary differential equations and differential equation of order three*, Journal of Applied Sciences, Vol. 8, No. 7, 2008, pp. 1256–1261.

[5] Mirgolbabaei H., Ganji D.D.: *Application of homotopy perturbation method to the combined KdV–MKdV equation*, Journal of Applied Sciences, Vol. 9, No. 19, 2009, pp. 3587–3592.

[6] Mirgolbabaei H., Ganji D.D., Taherian H.: *Soliton solution of the Kadomtse-Petviashvili equation by homotopy perturbation method*, World Journal of Modelling and Simulation, Vol. 5, No. 1, 2009, pp. 38–44.

[7] Adomian G.: *Solving frontier problems of physics, the decomposition method*, Kluwer Academic, Dordrecht, 1994.

[8] Hashim I., Noorani M.S.M., Batiha B.: *A note on the Adomian decomposition method for the generalized Huxley equation,* Applied Mathematics and Computation, Vol. 181, No. 2, 2006, pp. 1439–1445.

[9] Hashim I.: *Adomian decomposition method for solving BVPs for fourth-order integrodifferential equations*, Journal of Computational and Applied Mathematics, Vol. 193, No. 2, 2006, pp. 658–664.

[10] Hashim I., Noorani M.S.M., Ahmad R., Bakar S.A., Ismail E.S., Zakaria A.M.: *Accuracy of the Adomian decomposition method applied to the Lorenz system*, Chaos Solitons Fractals, Vol. 28, No. 5, 2006, pp. 1149–1158.

[11] Hashim I., Noorani M.S.M., Said Al-Hadidi M.R.: *Solving the generalized Burgers–Huxley equation using the Adomian decomposition method*, Mathematical and Computer Modelling, Vol. 43, No. 11–12, 2006, pp. 1404–1411.

[12] Noorani M.S.M., Hashim I., Ahmad R., Bakar S.A., Ismail E.S., Zakaria A.M.: *Comparing numerical methods for the solutions of the Chen system*, Chaos Solitons Fractals, Vol. 32, No. 4, 2007, pp. 1296–1304.

[13] Sun Y.P., Liu S.B., Keith S.: *Approximate solution for the nonlinear model of diffusion and reaction in porous catalysts by the decomposition method*, Chemical Engineering Journal, Vol. 102, No. 1, 2004, pp. 1–10.

[14] Wazwaz A.M.: *The modified decomposition method and Padé approximants for a boundary layer equation in unbounded domain*, Applied Mathematics and Computation, Vol. 177, No. 2, 2006, pp. 737–744.

[15] Awang Kechil S., Hashim I.: *Approximate analytical solution for MHD stagnation-point flow in porous media*, Communications in Nonlinear Science and Numerical Simulation, Vol. 14, No. 2, 2009, pp. 1346–1354.
[16] Awang Kechil W.S., Hashim I.: *Non-perturbative solution of free-convective boundary-layer equation by Adomian decomposition method*, Physics Letters A, Vol. 363, No. 1–2, 2007, pp. 110–114.
[17] Hayat T., Hussain Q., Javed T.: *The modified decomposition method and Padé approximants for the MHD flow over a non-linear stretching sheet*, Nonlinear Analysis: Real World Applications, Vol. 10, No. 2, 2009, pp. 966–973.
[18] Incropera F.P., Dewitt D.P.: *Introduction to heat transfer*, 3rd edition, John Wiley & Sons, Inc., 1996.
[19] Baker G.A.: *Essentials of padé approximants*, Academic Press, New York, 1975.

Analityczne rozwiązanie wymuszonego konwekcyjnie przepływu w warstwie przyściennej płaskiej płyty

W artykule przedstawiono zastosowanie metody dekompozycji Adomiana do wymuszonego, konwekcyjnie przepływu ciepła w poziomej, płaskiej płycie. Rozwiązania nieliniowych równań różniczkowych opisujących zagadnienie poszukiwana w postaci szeregów Adomiana. Z porównania otrzymanych wyników z wynikami innych metod numerycznych wynika doskonała ich zgodność, która potwierdza skuteczność zastosowanej metody. Otrzymane rozwiązanie pozwoliło jednoznacznie wyznaczyć rozkład i prędkości mian temperatury w analizowanej płycie.

ARCHIVES OF CIVIL AND MECHANICAL ENGINEERING

Vol. X 2010 No. 2

Application of photoelastic coating technique in tests of solid wooden beams reinforced with CFRP strips

T.P. NOWAK, L.J. JANKOWSKI, J. JASIEŃKO
Wrocław University of Technology, Wybrzeże Wyspiańskiego 27, 50-370 Wrocław, Poland

The paper presents selected results of tests carried out on hundred year old joists strengthened with carbon fibre reinforced polymers (CFRP). Besides the conventional electric-resistance extensometers (ERSG), the photoelastic coating technique (PCT) was used to measure strains in the reinforced (bonded) cross sections. No such attempt to apply PCT has been described in the literature before. The technique requires further studies to verify agreement between its results and the ones obtained by conventional measuring techniques.

Keywords: *timber structures, strengthening, CFRP, rehabilitation, photoelastic coating technique, four-point bending*

1. Introduction

The preservation of historic wooden components covers not only their technical condition, but also the artistic and cultural value of the building as a whole, including its ornamental details (often in the form of original woodcarving and polychrome). According to the Venice Charter, any measures taken with regard to national heritage buildings are to preserve and reveal the historic and aesthetic value the building, respecting the ancient substance and elements constituting authentic documents of the past. It is, however, allowed to strengthen historic buildings using modern conservation, construction and engineering techniques, provided the principles of conservation doctrine are adhered to [1–6].

The advances made in materials technology have significantly contributed to the development of construction and conservation technologies. When high-strength epoxy resins were synthesized in the late 1960s, attempts were made to use them to strengthen building structures. Compositions based on synthetic resins can be used to reinforce structural cross sections, to reproduce cross-sectional geometry and to produce joints bonding the reinforcing element with the reinforced one. The use of resins and gluing is becoming a recognized way of conserving timber structures, except for surface protection [3, 7–8].

The load-bearing capacity of components subjected to bending is usually determined by the cross-sectional tension zone. Wood defects in the tension zone reduce the load-

bearing capacity of the component much more than wood defects in the compression zone. A possible way of strengthening is to use reinforcement in the form of, for example, steel bars and plates and FRP (Fibre Reinforced Polymers) rods and strips [9–13]. Epoxy adhesives are mainly used to bond the reinforcement with the wood [14]. Steel plates and FRP materials are also used to reinforce shearing zones [15–16].

FRP composite materials are increasingly often used to reinforce wooden elements, increasing their load-bearing capacity and stiffness and endowing them with a more uniform structure [17–20]. Moreover, the new materials can be used to strengthen historic components in poor technical condition. FRP composites are usually reinforced with carbon fibres (CFRP), glass fibres (GFRP) and aramid fibres (AFRP).

This paper presents selected results of experimental research aimed at applying CFRP strips to reinforce defective (biological corrosion, inclusions, slope of grain, cracks) wooden beams and restore their load-bearing capacity, with a special focus on a comparison of strains measured by electric-resistance strain gauges with the ones determined using the photoelastic coating technique.

2. Material and method

2.1. Material

Wooden (pine) joists from a hundred (ca) year old building were the subject of the investigations. Different ways of reinforcing the beams with CFRP strips, presented in [e.g. 11, 20–21], were applied. Series A beams were not reinforced and served as the reference. In total, 21 beams (including 18 one hundred year old ones; 7 types, 3 beams in a series), each 4000 mm long and 120×220 mm in cross section, were tested. Test results for the series F beams are presented.

The series F beams were reinforced in the maximum bending moment zone with 400–600 mm long CFRP strips in a horizontal arrangement. The weakening of the tension zone was simulated by a cut out hole 25 mm in diameter (Figure 1).

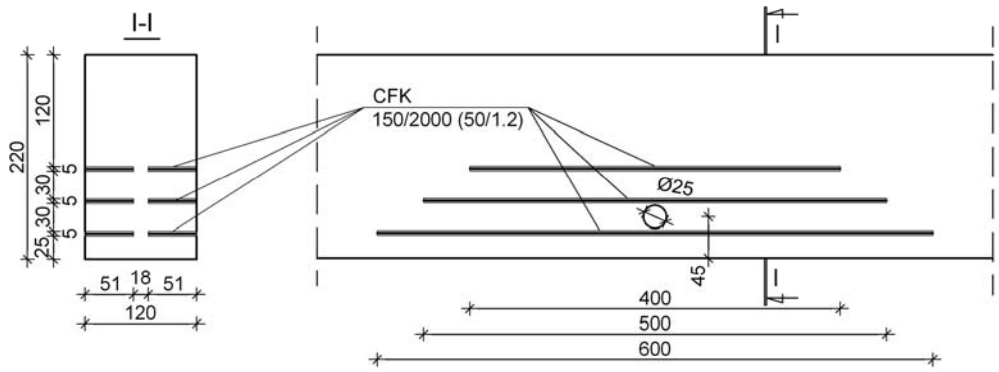

Fig. 1. Reinforcement scheme for beams of series *F* [mm]

Because of its consistency (making it easy to insert the reinforcement into the cross section), adhesive S&P Resin 55 (based on epoxy resin) for composite mats was used.

Table 1. Technical data of CFRP strip

Kind of strip	Strip width/breadth b [mm]	Strip thickness t [mm]	Young's modulus E [GPa]	Tensile strength f_t [MPa]
CFK S&P 150/2000	50	1.2	165	2800

2.2. Method

The beams were subjected to four-point bending (Figure 2) on a testing stand shown in Figure 3.

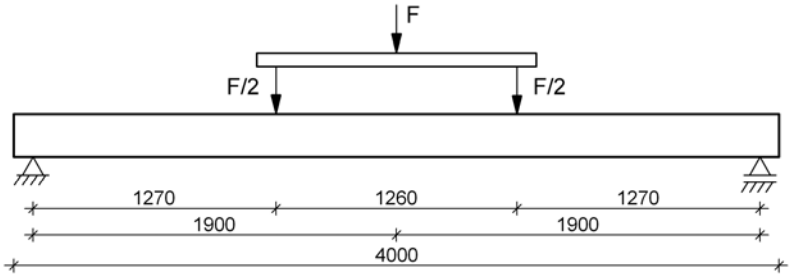

Fig. 2. Loading configuration and dimensions of tested beams in [mm]

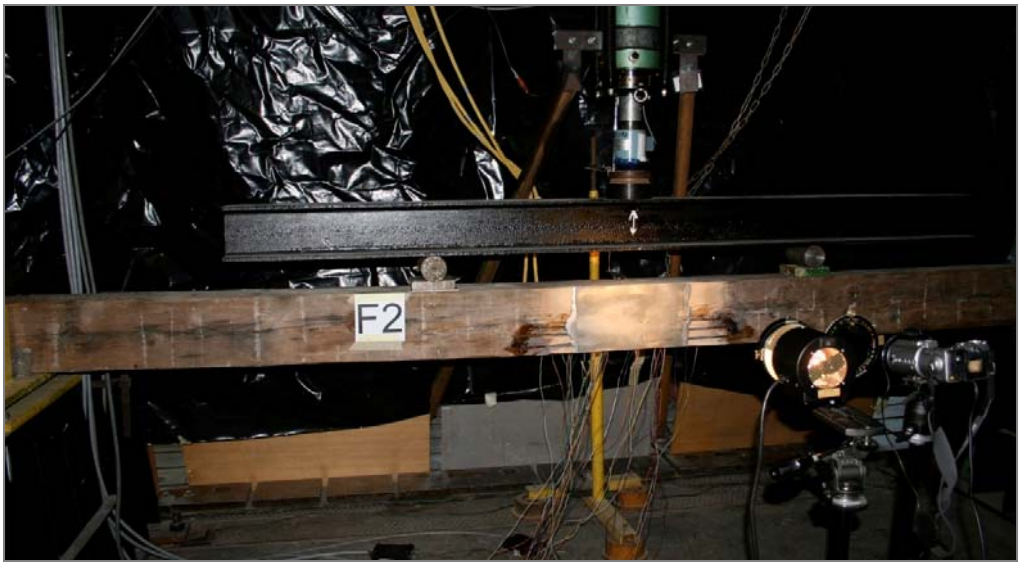

Fig. 3. Beam F2 on testing stand

Fork support, preventing loss of flexural stability (buckling), was used. Loading was applied by a servomotor made by VEB Verkzeugstoffprüfmaschine Leipzig and the force was measured by an ETP 7920-16 force gauge made by MOM Kalibergyár. The results were registered by a PC and a multichannel measuring system UPM 100 made by Hottinger Baldwin Messtechnik. The measuring equipment used in the tests was calibrated to 1% of the indication error in at least accuracy class 1.

During measurements the following were registered: the loading force (including the ultimate force) by the computer system, beam displacement in the middle cross section and on the supports by induction gauges W50 TS, strains in the wood by electric-resistance strain gauges RL 300/50 and strains in the strip by electric-resistance strain gauges RL 120/20. On the lateral surfaces of the beams (in the middle of their span) strain gauges were stuck on as shown in Figure 4. On the strips strain gauges were stuck on at every 50 mm along the whole length of each strip (Figure 5).

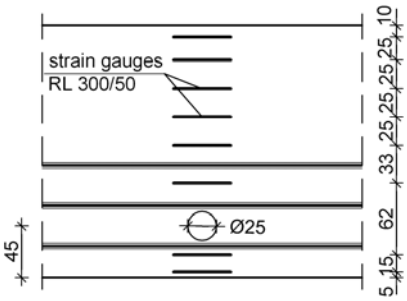

Fig. 4. Arrangement of electric resistance strain gauges on lateral surface of beam *F* [mm]

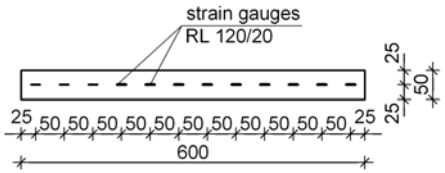

Fig. 5. Arrangement of electric resistance strain gauges on strip in beam *F* [mm]

Strains in the middle cross section of the tested beams were measured by electric-resistance strain gauges (ERSG) and on the opposite lateral surfaces by means of the photoelastic coating technique (PCT).

The photoelastic coatings were made of epoxy resin Epidian 5 with an di-n-phthalate addition, cold hardened with amino hardener Z-1 (100:12.5:10 parts by weight). The plate was 1.9 mm thick, 400 mm wide and 200 high. The coatings were glued to the lateral surfaces of the beams in the bending region, using an adhesive with an aluminium dust addition. A polariscope of V type (model 031 made by Vishay) and a digital camera were used to record images of (full- and half-order) isochromatic fringes.

Photoelastic measurements were performed using the field method. Full- and half-order ($N = 0, 1, 2...$ and $N = 0.5, 1.5, 2.5...$) isochromatic images were recorded. The information about the location of the particular isochromatic fringes in the analyzed cross section was used to determine the strain pattern. The accuracy of estimating the location of an isochromatic fringe of a given order was ± 0.1 of the isochromatic fringe order.

The surface of beam F2 prior to sticking on the photoelastic coating is shown in Figure 6. A knot, a hole, slots with bonded-in strips, natural cracks and the characteristic pattern of fibres around the knot are visible.

Fig. 6. Surface of beam F2 before photoelastic coating was stuck on [21]

3. Results

Table 2 shows ultimate force values for beams of series A and F. The increase in load-bearing capacity for the series F beams relative to the series A beams (unreinforced reference beams) was calculated from formulae (1).

$$\Delta F_u = \frac{F_{u,F} - F_{u,A}}{F_{u,A}} \cdot 100\% \tag{1}$$

where F_u is the mean ultimate force value for a particular beam series.

The increase in the load capacity of the tested elements reinforced with CFRP strips is significant since it amounted to 21% for the series F beams and to slightly above 79% for the series D beams [20–21]. The results for series F are very similar, which should be regarded as exceptional for full-size solid wooden cross sections (Table 2 and Figure 7).

Table 2. Ultimate force values for series A and F beams

	Beam					
	A1	A2	A3	F1	F2	F3
Ultimate force F_u [kN]	27.02	30.69	35.01	37.59	36.49	38.08
Mean ultimate force $F_{u,av}$ [kN]	30.91			37.39		
Increase in load capacity ΔF_u [%]	–			21.0		

Figure 7 shows static equilibrium paths and, for comparison, a trend line (determined by the least squares method) for the three tested reference beams. Limit deflection L/250 for floors and deflection L/167, i.e. increased by 50% for old (historic) building under repair are represented by vertical lines [22].

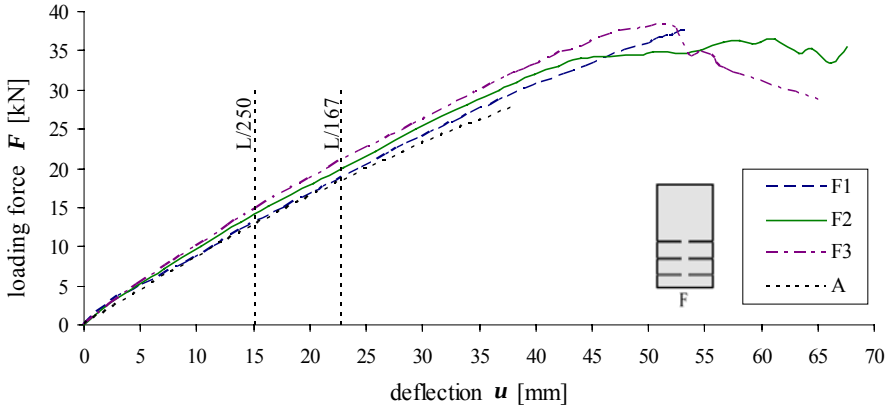

Fig. 7. Equilibrium paths for series F beams

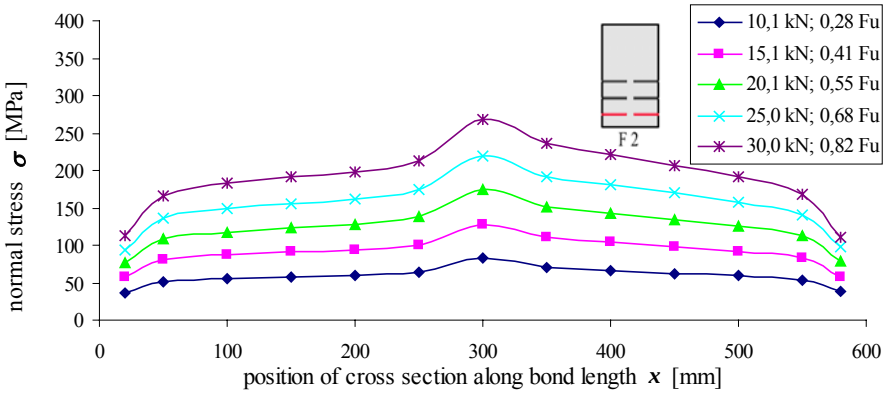

Fig. 8. Normal stress in bottom strip in beam F2

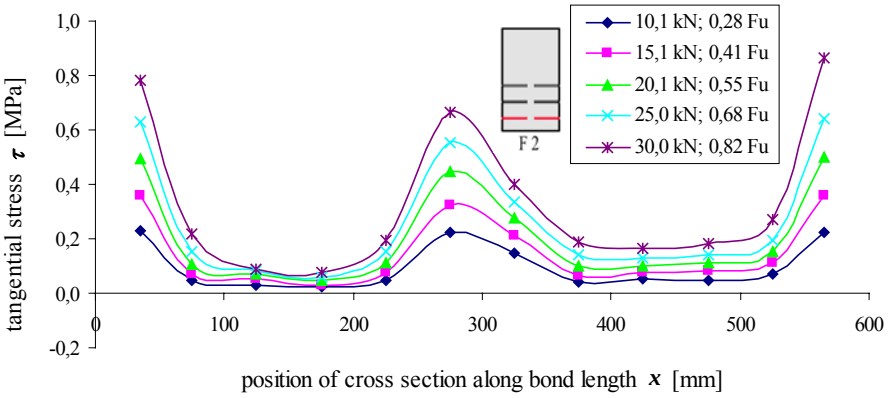

Fig. 9. Tangential stress in bond for bottom strip in beam F2

Figure 8 shows the normal stress pattern in the bottom strip of beam F2 while the tangential stress in the adhesive-bonded joint is shown in Figure 9. For the series F beams the maximum stress in the bottom strip was 363 MPa (strain in beam F1 was registered at a force of 37.2 kN immediately before the beam failed). The degree of strip cross section use was less than 13%. The tensile strength of the strip is 2800 MPa (Table 1).

The strains in the central cross sections of the tested beams were calculated on the basis of the recorded photoelastic images, from this basic relation [23–24]:

$$(\varepsilon_1 - \varepsilon_2) = N \cdot f_\varepsilon, \tag{2}$$

where:

ε_1, ε_2 – the principal strains [–],

N – the fringe order [–].

$$f_\varepsilon = \frac{\lambda}{2t_c \cdot K}, \tag{3}$$

where:

λ – the wavelength of the white light used during recording [m],

t_c – the thickness of the photoelastic coating [m],

K – an optical strain coefficient [–].

Strain isochromatic order $f_\varepsilon = 1.501 \times 10^{-3}$ was adopted for the calculations.

Figures 10–23 show exemplary images of full-order isochromatic fringes and strain $\varepsilon(h)$ distributions for different loading levels (beam F2).

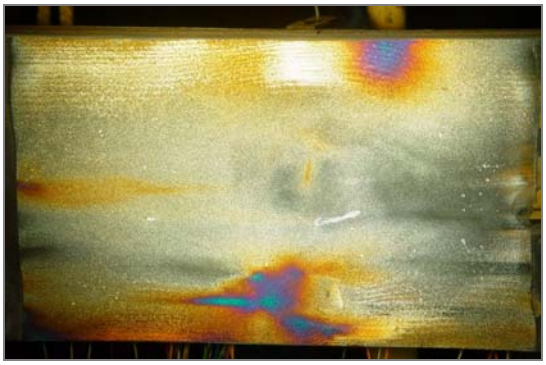

Fig. 10. Isochromatic fringes – beam F2 (F = 10.1 kN)

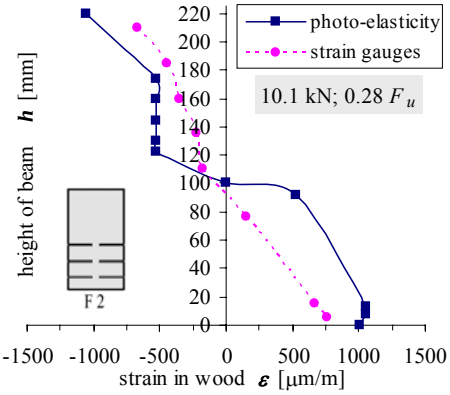

Fig. 11. Strain in wood in bent section – beam F2 (F = 10.1 kN)

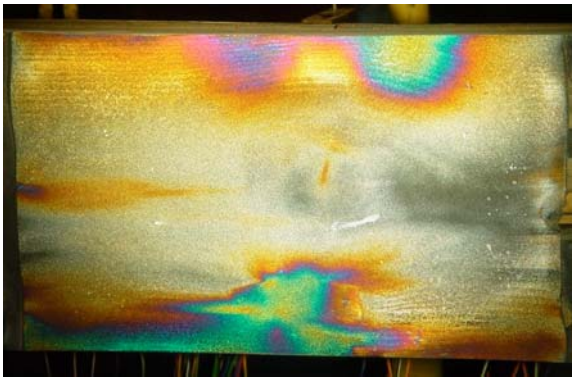

Fig. 12. Isochromatic fringes – beam F2 (F = 15.1 kN)

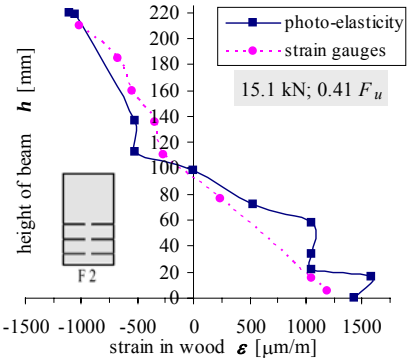

Fig. 13. Strain in wood in bent section – beam F2 (F = 15.1 kN)

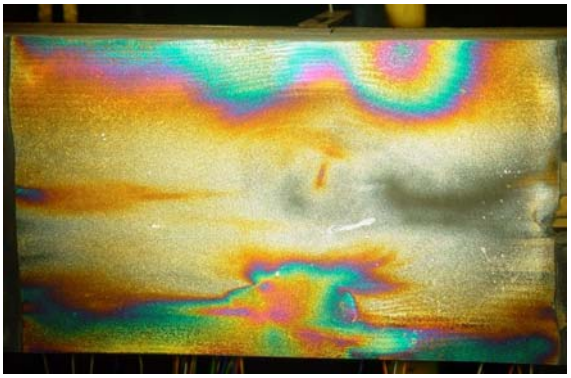

Fig. 14. Isochromatic fringes – beam F2 (F = 20.1 kN)

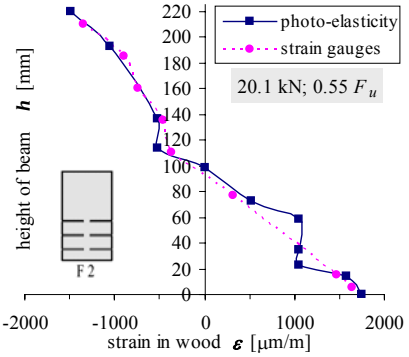

Fig. 15. Strain in wood in bent section – beam F2 (F = 20.1 kN)

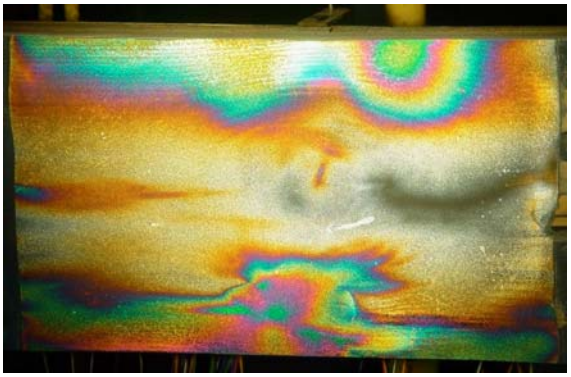

Fig. 16. Isochromatic fringes – beam F2 (F = 25 kN)

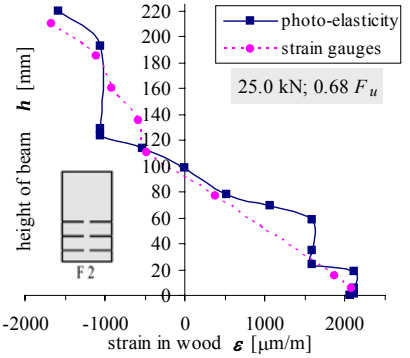

Fig. 17. Strain in wood in bent section – beam F2 (F = 25 kN)

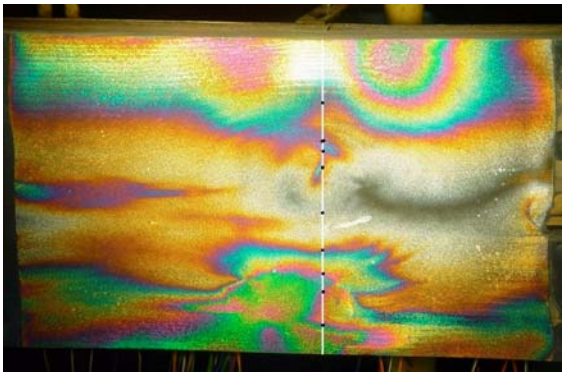

Fig. 18. Isochromatic fringes (with marked analyzed section) – beam F2 (F = 30 kN)

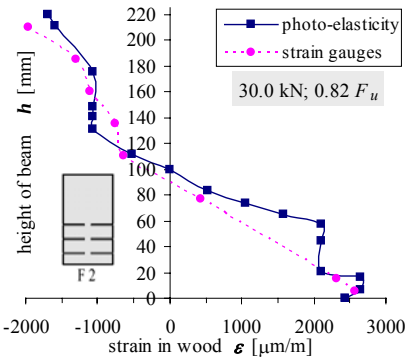

Fig. 19. Strain in wood in bent section – beam F2 (F = 30 kN)

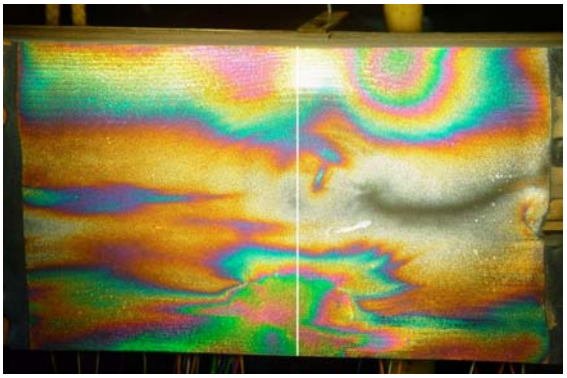

Fig. 20. Isochromatic fringes – beam F2 (F = 34.5 kN)

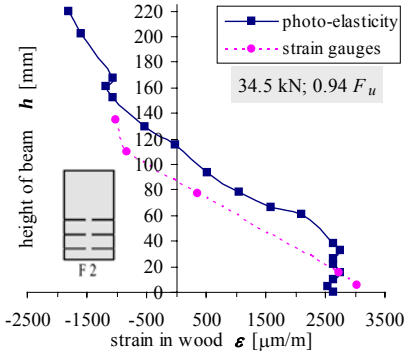

Fig. 21. Strain in wood in bent section – beam F2 (F = 34.5 kN)

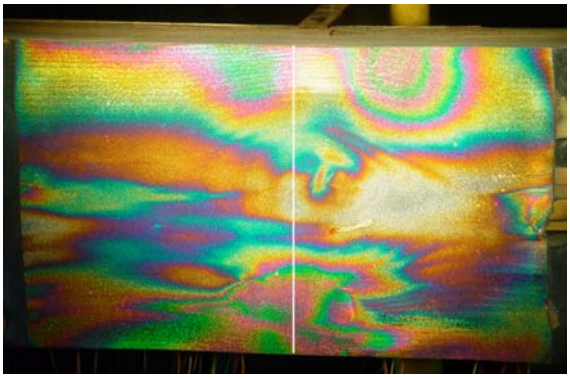

Fig. 22. Isochromatic fringes – beam F2 (F = 36.4 kN)

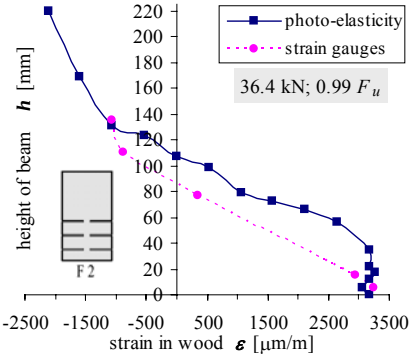

Fig. 23. Strain in wood in bent section – beam F2 (F = 36.4 kN)

An analysis of the isochromatic fringe images and strain $\varepsilon(h)$ distributions in beam F2 (Figures 10–19) showed that:

- the distribution of strain $\varepsilon(h)$ in the analyzed cross section is nonlinear and its disturbances increase with the load and are closely connected with the structure of the investigated surface,
- the sign of strain $\varepsilon(h)$ changes at a distance of ca 95 mm from the lower edge of the beam and this point shifts only slightly as the load increases,
- the effect of the hole on strain distribution in the tensioned zone is clearly visible, whereas the knot located at the level of the beam's theoretical neutral axis generates a lower strain gradient,
- changes in the $\varepsilon(h)$ value in the extreme fibres of the tensioned zone indicate the influence of the bottom strip: initially $\varepsilon(h)$ increases and from the load of 25.0 kN decreases, which is probably connected with the interference of strain fields generated by the hole located above, the influence of the strip and the bending of the beam; after the ultimate force value (36.49 kN) was reached, the strip came unstuck from the wood.

Thanks to the use of the photoelastic coating the state of strain in the investigated area of the beam could be qualitatively and quantitatively assessed for the whole loading range. The comparison of the strain values (calculated on the basis of the images of isochromatic fringes) for the loads of 34.5 kN (Figure 20) and 36.4 kN (Figure 22) indicates that when the load of 34.5 kN was exceeded, the beam entered the stage of failure. This is corroborated by the disproportionately large increase in strain relative to the increase in force, the nonlinearity of the deflection-force function and the characteristic patterns of isochromatic fringes around the tips of the cracks propagating during this stage of loading. For example, Figure 24 shows a pattern of isochromatic fringes indicating that the loading of the crack's edges corresponds to mode I with a small percentage of mode II. Although cracking was not closely analyzed here, one should note that the obtained information (images of isochromatic fringes) makes such analysis possible.

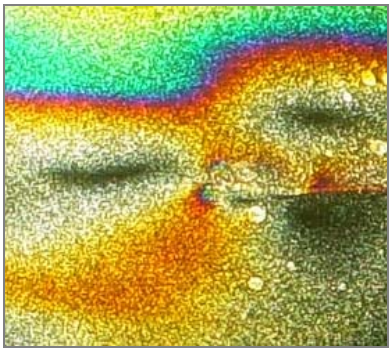

Fig. 24. Characteristic pattern of isochromatic fringes at crack's tip

In order to quantitatively compare the strain measuring techniques, the relative difference $\Delta\varepsilon$ between the strains measured by strain gauges and the ones determined using the photoelastic coating technique was calculated for the points corresponding to the extreme strain gauges (Figure 4). The results for different load levels are compared in Table 3. The values of $\Delta\varepsilon$ were calculated from the formula:

$$\Delta\varepsilon = \left| \frac{\varepsilon_g - \varepsilon_p}{\varepsilon_g} \right| \cdot 100\%, \tag{4}$$

where:

ε_g – strain in the timber, obtained from electrical-resistance strain gauge (ERSG) measurements,

ε_p – strain in the timber, obtained from photoelastic measurements (PCT).

Table 3. Comparison of strains in cross section of wood, determined by ERSG measurements and PCT measurements, for different load levels

Force F [kN]	Height of beam h [mm]	Strain (ERSG) ε_g [μm/mm]	Strain (PCT) ε_p [μm/mm]	Relative differences in strain $\Delta\varepsilon$ [%]
10.1	5	759	1037	36.6
	210	–667	–942	41.2
15.1	5	1187	1477	24.4
	210	–1018	–1013	1.5
20.1	5	1636	1724	5.4
	210	–1353	–1326	2.0
25.0	5	2081	2114	1.6
	210	–1663	–1395	16.1
30.0	5	2571	2640	2.7
	210	–1954	–1580	19.1
34.5	5	3035	2537	16.4
36.4	5	3250	3171	0.2

Fig. 25. Failure mode of beam F2

The mode of failure of beam F2 is shown in Figure 25. In none of the tested models the CFRP strip was found to fail. In most cases the beam failed along wood fibres, but not at the glue-wood boundary.

4. Conclusions

The investigations [21–22] have shown that the photoelastic coating reproduces well the structure of wood, including its cracks, defects, nail marks and connector (wooden plugs, screws, nails, etc.) holes.

When a photoelastic coating was stuck on, strain diagram disturbances caused by tangential stresses could be observed in the discontinuities (notches) in the cross section. Electric-resistance extensometry alone does not offer such possibilities since the measurements have a quasi-pointwise character, whereas the photoelastic coating supplies information from the whole surface.

The differences between the strain values measured by the strain gauges and the ones determined using the photoelastic method (Table 3) should be ascribed to structural differences (in wood fibre patterns, concentration of fibres, structural cracks and inclusions) between the two opposite lateral sides of the beams. It is impossible to produce a 120×220 mm (the tested beam cross section) wooden beam which would have an ideally parallel pattern of fibres on both sides.

To sum up, thanks to the use of the photoelastic coating the interaction between the reinforcing elements and the reinforced structure could be assessed more precisely. Therefore, this technique can be recommended for measuring strains in the components of timber structures. The observed differences between the strains measured by electric-resistance strain gauges and the ones determined by means of the photoelastic coating should not be considered as discriminating any of the measuring techniques.

It should be noted that the photoelastic coating became unstuck only at an advanced stage of failure. The results presented in [21] showed that the propagation of cracks in the wood (accompanying its failure) was reproduced in the characteristic image of isochromatic fringes observed in the coating and the cracking of the coating proceeded in the same direction as the failure in the wood. This opens up possibilities of observing the dynamics of the phenomena connected with limit states in timber structures.

References

[1] Balsamo A., Cerone M., Viskovic A.: *New wooden structures with composite material reinforcements for historical buildings: the case of the arena flooring in the Colosseum*, [in:] Proceedings of the IABSE Conference: *Innovative wooden structures and bridges*, Lahti, Finland, 29–31 August, 2001, pp. 361–366.

[2] Borchardt J.K.: *Reinforced plastics help preserve historic buildings*, Reinforced Plastics, Vol. 47, No. 11, 2003, pp. 30–32.

[3] Jasieńko J.: *Glued and engineering joints in repair, conservation and reinforcement of historical timber structures* (in Polish), Lower Silesia Educational Publishers (DWE), Wrocław, 2003.
[4] Parisi M. A., Piazza M.: *Restoration and strengthening of timber structures: principles, criteria and examples*, Practice Periodical on Structural Design and Construction, Vol. 12, No. 4, 2007, pp. 177–185.
[5] Quagliarini E., D'Orazio M., Stazi A.: *Rehabilitation and consolidation of high-value "camorcanna" vaults with FRP*, Journal of Cultural Heritage, Vol. 7, No. 1, 2006, pp. 13–22.
[6] Van Gemert D., Vanden Bosch M.: *Structural restoration of wooden beams by means of epoxy resin*, Materials and Structures, Vol. 20, No. 3, 1987, pp. 165–170.
[7] Wheeler A.S., Hutchinson A.R.: *Resin repairs to timber structures*, International Journal of Adhesion and Adhesives, Vol. 18, No. 1, 1998, pp. 1–13.
[8] Ajdukiewicz, A., Brol J.: *Modern strengthening methods of old timber structures*, in: Proceedings of the IABSE Conference: *Innovative wooden structures and bridges*, Lahti, Finland, 29–31 August, 2001, pp. 479–484.
[9] Borri A., Corradi M., Grazini A.: *A method for flexural reinforcement of old wood beams with CFRP materials*, Composites Part B: Engineering, Vol. 36, No. 2, 2005, pp. 143–153.
[10] De Lorenzis L., Scialpi V., Tegola A.L.: *Analytical and experimental study on bonded-in CFRP bars in glulam timber*, Composites Part B: Engineering, Vol. 36, No. 4, 2005, pp. 279–289.
[11] Jasieńko J., Nowak T., Bednarz Ł.: *Reinforcement of bent timber beams in historic buildings*, in: *Proceedings of the international conference on protection of historical buildings*, Prohitech 09, Rome, Italy, 21–24 June, 2009, pp. 325–330.
[12] Radford D.W., Van Goethem D., Gutkowski R.M., Peterson M.L.: *Composite repair of timber structures,* Construction and Building Materials, Vol. 16, No. 7, 2002, pp. 417–425.
[13] Schober K.U., Rautenstrauch K.: *Post-strengthening of timber structures with CFRP's*, Materials and Structures, Vol. 40, No. 10, 2007, pp. 27–35.
[14] Raftery G., Harte A., Rodd P.: *Bonding of FRP materials to wood using thin epoxy gluelines*, International Journal Adhesion and Adhesives, Vol. 29, No. 5, 2009, pp. 580–588.
[15] Akbiyik A., Lamanna A.J., Hale W.M.: *Feasibility investigation of the shear repair of timber stringers with horizontal splits*, Construction and Building Materials, Vol. 21, No. 5, 2007, pp. 991–1000.
[16] Triantafillou T.C.: *Composites: a new possibility for the shear strengthening of concrete, masonry and wood*, Composites Science and Technology, Vol. 58, No. 8, 1998, pp. 1285–1295.
[17] Bogacz W., Lis Z., Łodygowski T., Rapp P.: *Tests and calculations of wooden beams reinforced with bonded-in carbon fibre strips* (in Polish), Inżynieria i Budownictwo, No. 10, 2007, pp. 541–544.
[18] Brol J.: *Strengthening of bent glued laminated (glulam) beams with GARP tapes at the stage of production*, Wiadomości Konserwatorskie, No. 26, 2009, pp. 345–353.
[19] Makowski A.: *Investigations of the influence of CFRP composite composition on stress and strain in the elastic states of reinforced composite I-beams* (in Polish), Przemysł Drzewny, No. 11, 2007, pp. 24–28.
[20] Nowak T.: *Analysis of the static work of bent wooden beams reinforced with CFRP* (in Polish), PhD thesis, Wroc. Uni. of Tech., 2007, http://www.dbc.wroc.pl/publication/1778.

[21] Jankowski L.J., Jasieńko J., Nowak T.P.: *Experimental assessment of CFRP reinforced wooden beams by 4-point bending tests and photoelastic coating technique*, Materials and Structures, Vol. 43, No. 1–2, 2010, pp. 141–150.
[22] Polish Standard PN-B 03150:2000 *Timber structures – structural analysis and design* (in Polish).
[23] Dally J.W., Riley W.F.: *Experimental stress analysis*, McGraw-Hill Inc., 2001.
[24] Kapkowski J., Słowikowska I., Stupnicki J.: *Testing of stresses by the photoelastic coating method* (in Polish)., PWN, Warsaw, 1987

Zastosowanie metody elastooptycznej w badaniach drewnianych belek wzmocnionych taśmami CFRP

W pracy przedstawiono wybrane wyniki badań wzmocnionych stuletnich belek stropowych. Do wzmocnienia i odtworzenia nośności drewnianych belek z defektami – korozja biologiczna, inkluzje, skręt włókien, pęknięcia drewna – zastosowano taśmy CFRP (*carbon fibre reinforced polymers*). Obok tradycyjnych metod pomiarowych – czujniki elektrooporowe (ERSG) – do pomiaru odkształceń przekrojów wzmocnionych (zespolonych) zastosowano metodę elastooptycznej warstwy powierzchniowej (PCT). Dotychczas nie opisano takiej próby w literaturze przedmiotu. Metoda wymaga przeprowadzenia dalszych badań, mających na celu weryfikację zgodności z pomiarami metodami tradycyjnymi.

ARCHIVES OF CIVIL AND MECHANICAL ENGINEERING

Vol. X 2010 No. 2

Sediment particles and turbulent flow simulation around bridge piers

R. PASIOK, E. STILGER-SZYDŁO
Institute of Geotechnics and Hydrotechnics, Wrocław University of Technology,
Wybrzeże Wyspiańskiego 27, 50-370 Wrocław, Poland.

Scientific surveys regarding the mechanisms of transportation of bed material grains from the scour hole are undersupplied in literature. This work takes into account the mechanisms behind a local scour, associated with a bridge pier impact. In order to gather information about the flow field, an appropriately formulated numerical model of flow was used, the so-called LES (large-eddy simulation). The numerical analyses carried out in this work, examining the mechanisms of the transportation of bed material grains by means of a suitably formulated flow model, constitute theoretical background for the analysis of velocity fields around bridge piers. Those analyses will come in handy during hydraulic computations of bridges.

Keywords: *bridge piers, bed scour, particles, turbulent flow model*

1. Introduction

Bridge architectural structures are founded in complex and complicated geological-engineering conditions [16]. Typically, in the subsoil there occur low-bearing soils (mud aggregates and peats), large, concentrated vertical and horizontal loads transferred by the bridge supports onto the subsoil, as well as a deep scour of the river bed. Those circumstances impose the necessity of using deep foundations, following high-quality subsoil investigation. A designer should take into account rigorously the bed scour next to the supports. World statistics confirm that about 80% of all bridge failures were caused by the wash-out of piers (Figure 1). Hence, the proper designing and maintenance of the supports – because of that potential threat – are responsible, to a great extent, for the bridge endurance.

Scouring is a particular form of bed erosion, caused by the impact of hydrodynamic forces, leading to the river-bed lowering. It occurs both during the freshet as well as in normal flow conditions. Scour intensity grows with the increase of the flow velocity. A scour hole is a hollow, brought about by scouring. The scouring process consists of such components as:

- aggradation (deposition of the sediment that comes from river-bed erosion) and degradation (lowering of the stream bed level, which results from the deficiency of sedimentation of the material coming from the river basin upper part);

• general scour (stream bed lowering along the entire watercourse bed profile or on its considerable part) – periodical or in course of freshets;

• local scour (the entrainment of bed material next to bridge piers and abutments), in form of:

a) clear-water scour – when there is no rubble movement from the areas located higher,

b) live-bed scour – when the rubble is entrained from higher areas to the scour hole beneath.

Fig. 1. An example of bridge scour [22]

The size of the scour holes depends on the shape of the building that affects the flow. It is the shape of the buildings that generates a turbulent flow, which, in turn, conditions the occurrence of the structures that affect bed scour process. Most of the researchers concentrate on the scour hole shape and its evolution in time, leaving aside an exact survey of the behaviour of particular bed material grains.

A complex phenomenon of scouring around bridge piers is one of the leading causes of bridge failure but its mechanisms are still under investigations [10]. Numerical models are often presently used for turbulent flow investigations [12]. The paper exemplifies the use of such model to track mass particles in a vicinity of cylindrical pier. Flow observations reveal that a complex ordered flow pattern (Figure 2) occurs even in a case of simple geometry hydraulic structure [8].

Models based on Reynolds averaged Navier–Stokes (RANS) equations give as a result a statistical flow field characteristics and applying them to highly unsteady flow objects studies is limited [20]. Flow objects are coherent fluid packets that temporarily

move along similar trajectories. The object size (called often an object scale) can be much diversified. There are many other works aimed at flow structure description [6], [17]. In a case of cylindrical pier most often specified objects are: downward flow at the upstream side of a pier, horseshoe vortex and vertical wake vortices. These vortices are accompanied by considerable velocity and pressure gradients. Many authors suggest that the objects participate in bed material transport [3]. The paper gives a brief description of large-eddy simulation (LES) formulated for present study. Similarly to RANS, the model is based on Navier–Stokes equations. Although, degrees of freedom (number of parameters involved) of exact solution are limited by variables filtering [2].

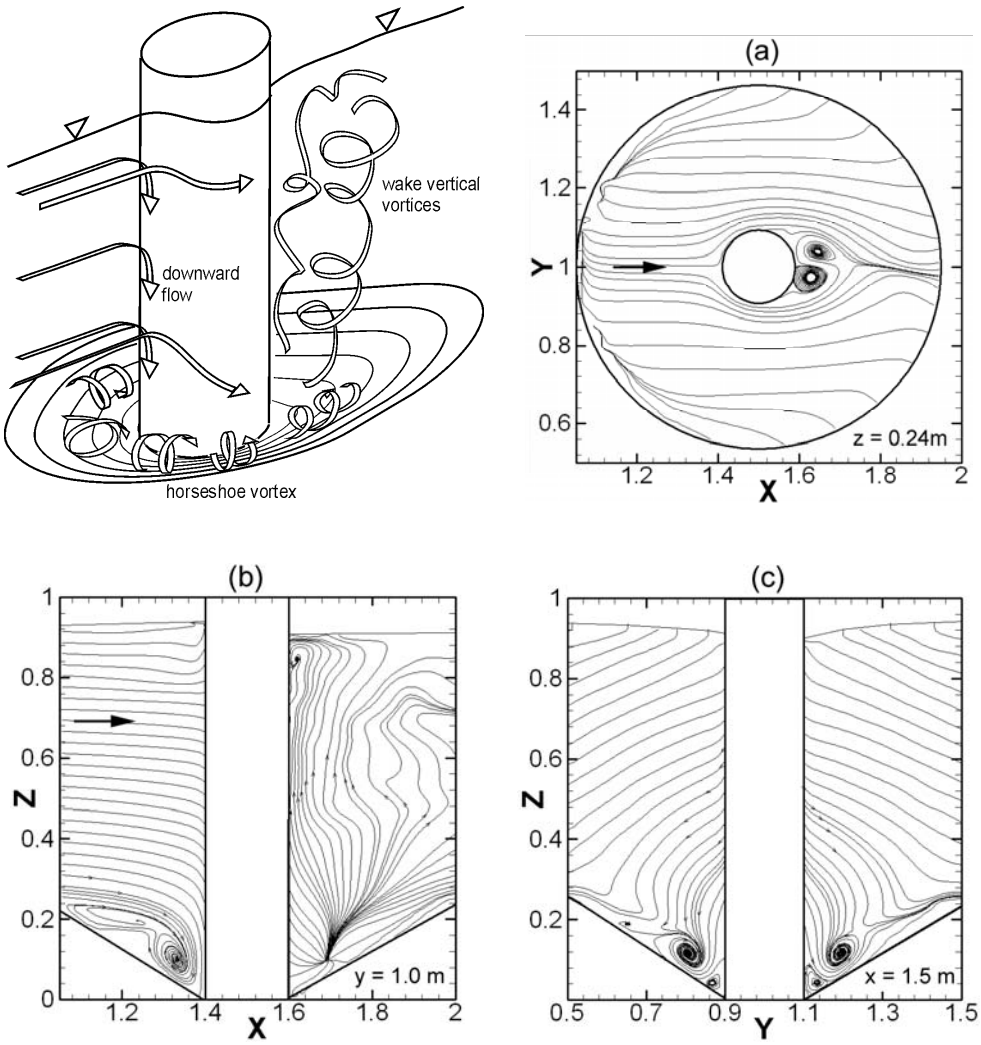

Fig. 2. Flow pattern around cylindrical pier with a developed scour hole

To get the exact solution all the space and time scales of the solution must be taken into account. Then, there is no need to introduce additional assumptions concerning different turbulent scales interaction, i.e. we do not need a turbulence model. This is called a direct numerical simulation (DNS). It demands great computational power as the grid must be very fine and accurate higher order numerical schemes must be used. The computational cost of DNS is proportional to the Reynolds number cubed (Re^3).

The computational domain was discretized by finite volume method [7]. Second order finite difference schemes were used for equations approximation. Finally, a discrete particle motion model was formulated for spherical mass particles.

Scientific surveys regarding the mechanisms of transportation of bed material grains from the scour hole are undersupplied in literature. Due to the complex characteristics of the flow around bridge piers, such observations inflict significant difficulties. This work takes into account the mechanisms behind a local scour, associated with a bridge pier impact. In order to gather information about the flow field, an appropriately formulated numerical model of flow was used, the so-called LES (large-eddy simulation). Even for minor average flow velocity values, the alteration of flow direction or separation may trigger the occurrence of some remarkably durable flow structures, with characteristic large velocity gradients.

2. Turbulent flow model

The model is based on Navier–Stokes (N-S) equations for incompressible fluid

$$\frac{\partial \mathbf{u}}{\partial t} + \nabla\cdot(\mathbf{uu}) = -\frac{1}{\rho}\nabla p + \nabla\cdot\nu\left(\nabla\mathbf{u} + \nabla\mathbf{u}^T\right). \tag{1}$$

Equations (1) are solved only for a certain range of turbulent object scales. To maintain influence of objects not directly included in the solution a model of their action is introduced – this is analogous to a turbulence model in RANS. RANS, however, does not give much information about the flow objects of our interest. In LES we solve directly large-scale anisotropic turbulence objects that can be represented on a computational mesh. These are called resolved objects or scales. It is assumed that the smaller objects, which cannot be represented on a mesh, are more isotropic and much easier to model. These are subgrid scale objects. The size that separate resolved and subgrid scales is called a cut-off length and should be placed sufficiently far in the inertial subrange of turbulent energy spectrum, i.e. where the energy transfer is described by the Kolmogorov law. Considering the turbulent energy spectrum the difference between RANS and LES can be easily depicted (Figure 3). In RANS, practically all the spectrum is modelled. In LES, by variables filtering procedure [5], an exact solution for a considerable part of the spectrum is obtained. Therefore, in LES we get

much more detailed flow information than in RANS. Nevertheless, it should be noted that LES comes at much bigger computational cost.

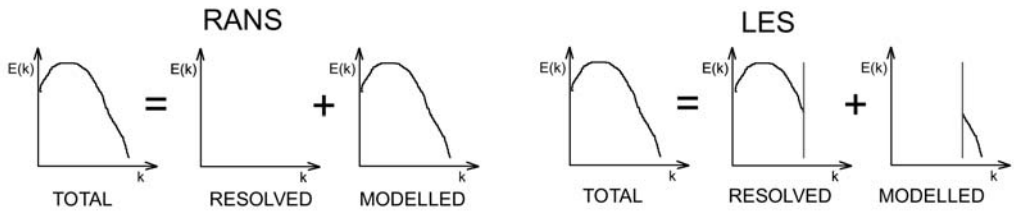

Fig. 3. Decomposition of turbulent energy spectra ($E(k)$) in RANS and LES, k is a wave number (inverse characteristic length of objects) – adopted from [15]

$$\nu_{\mathrm{SGS}} = (C_S \Delta)^2 \left|\overline{\mathbf{S}}\right|, \quad \overline{\mathbf{S}} = 1/2\left(\nabla \overline{\mathbf{u}} + \nabla \overline{\mathbf{u}}^T\right). \tag{2}$$

The influence of unresolved subgrid scales is expressed by the subgrid model. In this work the dynamic Smagorinsky model is used in which subgrid scale viscosity defined by Equation (2) [15]. To obtain the effect of energy transfer between resolved and unresolved scales an eddy-viscosity concept is formulated and it is assumed that the subgrid stress tensor τ depends on rate of strain tensor of resolved scales. Smagorinsky model coefficient C_S is calculated during simulation on the basis of velocity field of the resolved scales.

Filtered N-S equations together with subgrid model can be written as

$$\frac{\partial \overline{\mathbf{u}}}{\partial t} + \nabla \cdot \left(\overline{\mathbf{u}}\,\overline{\mathbf{u}}\right) = -\frac{1}{\rho}\nabla \overline{p} + \nabla \cdot \nu\left(\nabla \overline{\mathbf{u}} + \nabla \overline{\mathbf{u}}^T\right) + \nabla \cdot \boldsymbol{\tau}. \tag{3}$$

The equations represent conservation law for an infinite small space-time region. To use them in finite volume method they must be integrated over the control volume and time (as LES is intrinsically unsteady). In the presented work a collocated, unstructured mesh is used.

$$\int_t^{t+\Delta t}\left[\frac{\mathrm{d}}{\mathrm{d}t}\int_V \overline{\mathbf{u}}\,\mathrm{d}V + \int_V \nabla \cdot (\overline{\mathbf{u}}\,\overline{\mathbf{u}})\,\mathrm{d}V - \int_V \nabla \cdot \nu_{eff}\left(\nabla \overline{\mathbf{u}} + \nabla \overline{\mathbf{u}}^T\right)\mathrm{d}V\right]\mathrm{d}t = -\int_t^{t+\Delta t}\left[\frac{1}{\rho}\int_V \nabla \overline{p}\,\mathrm{d}V\right]\mathrm{d}t, \tag{4}$$

where:

ν_{eff} is a sum of kinematic viscosity ν and modelled subgrid viscosity ν_{SGS}.

Solution of the algebraic equations system for all transported quantities is obtained by iterative conjugate gradient method Bi-CGSTAB [18]. The pressure matrix is solved in PISO procedure [9].

3. Solid particles simulation

A discrete particle motion model is based on equation resulting from Newton's second law. Considering forces acting on a particle, friction and gravity is taken into account. The friction force is computed on the basis of friction coefficient C_D in the formulation of Schiller and Nauman [4]. Equation of particle motion reads

$$\frac{\mathbf{d}\mathbf{u}_p}{\mathbf{d}t} = -\frac{\mathbf{u}_p - \mathbf{u}}{\tau_{\mathbf{u}}} + \mathbf{g}, \tag{4}$$

where:

$\mathbf{u}_d$ is velocity of particle,

$\mathbf{u}$ is fluid velocity in the computational cell (volume) in which the particle resides at the moment,

$\tau_{\mathbf{u}}$ is particle momentum relaxation time [13].

$$\tau_{\mathbf{u}} = \frac{8m_p}{\pi\rho C_D D^2 |\mathbf{u}_p - \mathbf{u}|} = \frac{4}{3}\frac{\rho_p D}{\rho C_D |\mathbf{u}_p - \mathbf{u}|}, \tag{5}$$

where:

$_p$ applies to the discrete phase, i.e. solid particles,

m is a mass,

ρ is density,

D is particle diameter. Equation (5) is solved independently from fluid equations – fluid phase is frozen while the new particles positions are solved, then particles are frozen and their momentum is added as a source term to the momentum equation of fluid. The decoupling let us avoid stability problems in momentum calculations. Particles model includes a simple collision *hard sphere model* [11].

When a collision between two particles occurs, algebraic equation of momentum conservation is used. Particles velocities after collision are computed on the basis of coefficient of restitution $C_R = u_n^{ac}/u_n^{bc} = (u_{\xi 2}^{ac} - u_{\xi 1}^{ac})/(u_{\xi 2}^{bc} - u_{\xi 1}^{bc})$ (Figure 4b), where u_n is relative particles velocity magnitude before (^{bc}) and after collision (^{ac}). A change of colliding particles momentum is

$$\Delta\mathbf{M}_{cp} = m_p(1 + C_R)(\mathbf{u}_1^{bc} - \mathbf{u}_2^{bc}), \tag{6}$$

where $m_p = \dfrac{m_1 m_2}{m_1 + m_2}$.

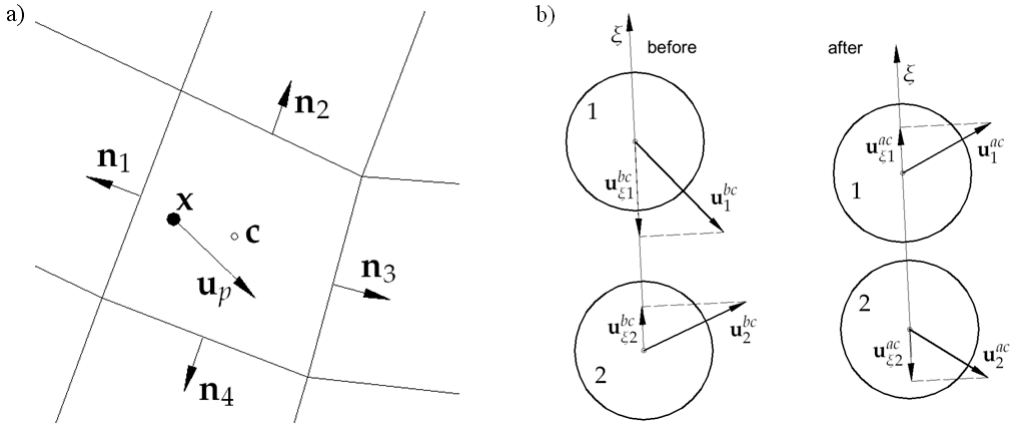

Fig. 4. Illustration for particles tracking (a) and particles collision schema (b)

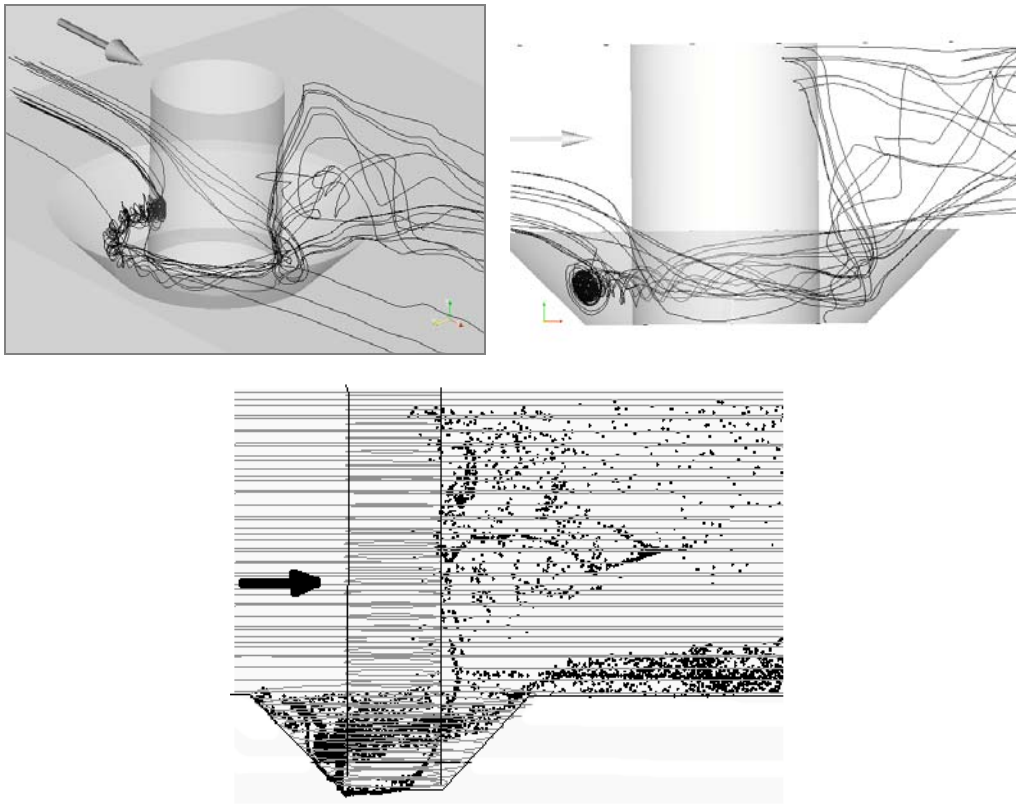

Fig. 5. Instantaneous velocity stream traces and marker particles around a cylindrical pier with a scour hole

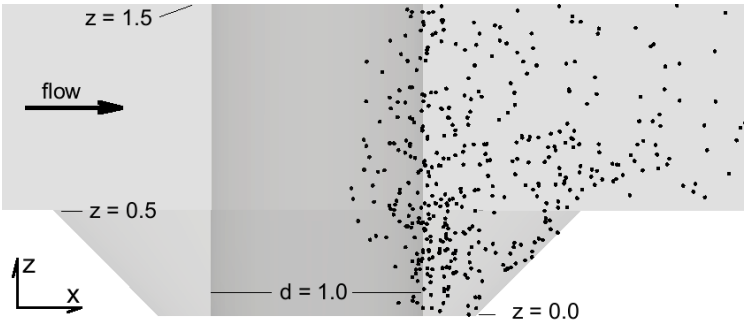

Fig. 6. Positions of mass particles generated close to the bed on downstream side of the scour hole (particles size not to scale)

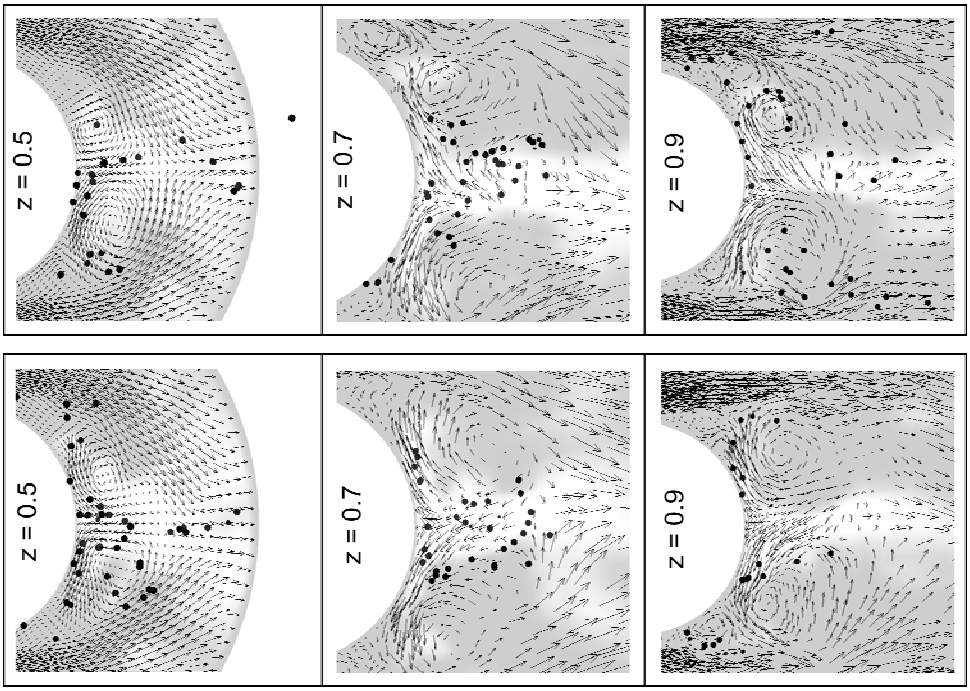

Fig. 7. Example of particles positions at various levels and times. See text for details

The corrected velocities

$$\mathbf{u}_1^{ac} = \mathbf{u}_1^{bc} - \frac{\Delta \mathbf{M}_{cp}}{m_1} \text{ and } \mathbf{u}_2^{ac} = \mathbf{u}_2^{bc} - \frac{\Delta \mathbf{M}_{cp}}{m_2}, \tag{7}$$

are used as an initial condition for particles motion Equation (5).

When the particle enters the computational domain its position is found by checking for which cell the condition $\beta_i \le 0$, $\beta_i = (\mathbf{x}-\mathbf{c})\cdot\mathbf{n}_i$ is met for all walls i (Figure 4a). Then an efficient "from face to face" method is used for particles tracking [13]. Particle doesn't change the cell if

$$\lambda_i > 1, \quad \lambda_i = \frac{(\mathbf{c}-\mathbf{x})\cdot\mathbf{n}_i}{(\mathbf{u}_p\Delta t)\cdot\mathbf{n}_i}, \tag{8}$$

and passes across a face if $\lambda_i < 1$ – then the new particle position is calculated as $\mathbf{x}_{new} = \mathbf{x}_{old} + \lambda\mathbf{u}_p\Delta t$.

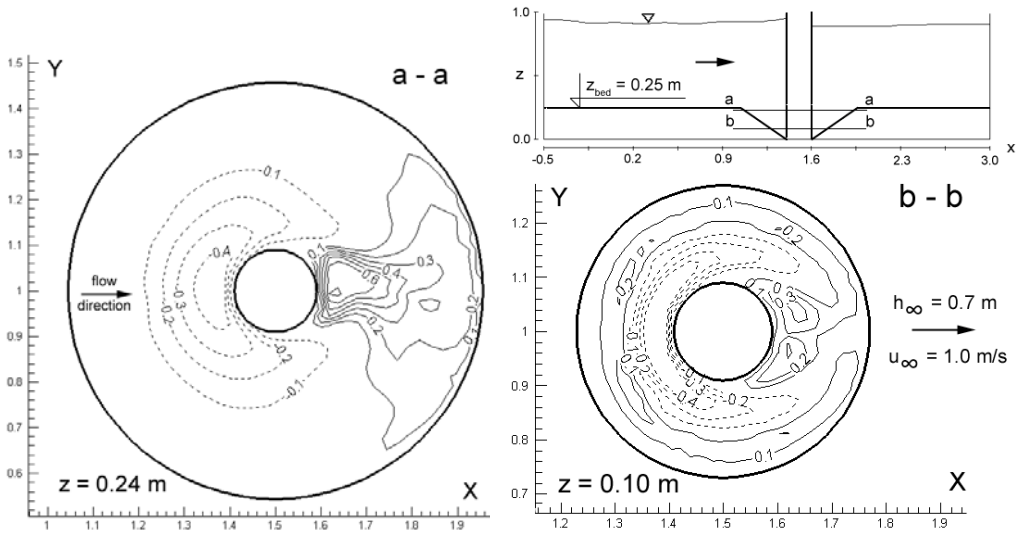

Fig. 8. Instantaneous vertical component of velocity in scour hole [m/s] – dashed line for negative values

4. Results

The models described above are used for studies of flow and particles motion around a cylindrical pier with a scour hole. It is not a scouring model at piers. The aim of computations is to investigate trajectories of particles already lifted from bed – particles are randomly generated slightly above the bed. Turbulent objects that develop around a pier: horseshoe vortex and wake vertical vortices are greatly affected by the existence of a scour hole – all the vortices are much more intense. The previous studies [14] with marker-particles (i.e. with zero mass) indicated the possible mechanism of transporting particles out of the scour hole. The markers tended to concentrate in vertical vortices cores, regions of local vorticity maxima and pressure minima. Once trapped into a vortex core, markers were transported out of the scour hole (Figure 5).

Simulations with mass particles do not show such effect. Some of the particles generated slightly above bed level on downstream side of pier are lifted up as shown in Figure 7. The results of simulations performed for limited range of mass particle diameters indicate that particles move rather in a strong jet directed towards the surface. The jet is enclosed by downstream pier wall and vertical wake vortices. The vertical vortices are the main driving force for the jet. Figure 7 shows example particles positions at various levels above the bed ($z = 0.5$ is the initial bed level). Arrows show velocity vectors directions and magnitude. Brightness corresponds with vertical velocity component value.

5. Prevention of bed scour next to bridge piers

The numerical analyses carried out in this work, examining the mechanisms of the transportation of bed material grains by means of a suitably formulated flow model, constitute theoretical background for the analysis of velocity fields around bridge piers. Those analyses will come in handy during hydraulic computations of bridges.

In contemporary designing the authors take into account the occurrence of bed scour holes at the bridge supports, and so they adjust the pier foundations to the maximum value of the forecasted declining of the soil around them. The largest general and local scour is forecasted, and on that basis the foundations are designed in such a way so that the bridge piers are stable in case of predicted wash-out.

When determining anticipated scour, one takes into consideration hydraulic conditions that will occur after the bridge crossing is built; it is also indispensable to analyse the angle of the flow to piers (angle of attack), in order to assess the rate by which the water flow under the bridge will decrease. Hydraulic computations of bridges include: determining minimum clear span as well as the expected deepening of the river bed in the bridge cross-section, local scour at the piers and the height of swell under the bridge. The minimum clear span is settled on the basis of permissible scour values in the bridge cross-section. Bridge clear span should be estimated by means of a trial method, which entails: determining minimum clear span, the settling of the assumed location of abutments and piers as well as their size, the computation of predicted scour and swell values, and then, their comparison with the conditions given in [21]. Many computational cases are taken into account, depending on: flow type, scour proneness of the river bed, the way the rubble progresses. By means of an analysis of the river bed scour, the size of the bed lowering in a bridge cross-section is determined, which is expressed by the degree of bridge cross-section scour. That is the relation of average depth values after and before the river-bed scour, calculated for a reliable datum of water level. Permissible values of the degree of scour, depending on the support foundation type, are presented in [21].

Basic knowledge about the flow is provided by diverse measurement techniques. Another available source includes automatic devices recording local bed scour at the bridge piers. They work in the manner of stationary echo sounders or they are equipped

with the sensors that are fastened to elastic tapes, arranged radially around the piers and embedded at different depths in the river bed. The sensors may as well be attached to the foundations or to vertical bars submerged in the river bed. By obtaining the information on the scour progress, it is possible to undertake counteraction at the right time. Among the methods of preventing the effects of river bed scour at the bridge piers, the following should be enumerated: applying deep foundations, a suitable location and shape of the supports, soil reinforcement, appropriate control of the upper course of the river (which has the impact on the lower course), as well as the techniques of preventing or reducing erosion and local scour of the river's banks and bed. The protection of the river bed against erosion includes the following methods: reducing the hydraulic force that affects the banks and bed of a river, increasing the resistance of the river's banks and bed to the hydraulic force impact. The first group entails the modification of piers (by giving them a more streamlined shape or through the encasing of a multi-pier frame with a reinforced concrete coating, which will easily stop the remains or debris carried along by the water; finally, the devices connected with piers that locally change the stream course – for instance horizontal slabs over the river bed or cascades constructed across the watercourse. The second group comprises the protections of the river's banks and bed (by means of mattresses, rock fillings, a sheet-pile wall etc.). The watercourse bed scour may be prevented by means of the drowning of a mattress around the foundation and loading it with a rock filling. Instead of the mattress, it is possible to make a rock filling embedded below the watercourse bed level. In some cases, in order to prevent the river bed erosion, it is necessary to apply regulating hydrotechnical architectural structures, e.g. longitudinal dams, repelling spurs (wing dams), cascades or the reinforcement of the river bed on a long section below the bridge location. To counteract the erosion of the river's banks and bed, it is also possible to use a cribwork in the form of wire-net containers that are filled with stones (most frequently the container's size is 2×1×1 m, whereas for the protection against the bottom scour, smaller ones – 0.5 m thick – are used). The cribwork joined with wire is a good safeguard for large surfaces of banks or bed. The protection and reinforcement of a pier based on a shallow foundation that is located on a soft rock prone to river erosion, may be achieved by means of embedding a reinforced well, which would surround the foundation, into the rock or by installing piles next to the pier, and constructing a structure that will transfer loads from the pier onto the well (piles).

An important issue is the question of how to reduce the danger posed to bridge structures by floods. Basic principles for the designing of new bridges from that perspective should be as follows:

- bridge architectural structures should be located at the places where the stream direction during the great water is the same as in the periods of low and average water,
- bridges should not be built at the places where islands, shoals and rubble sedimentation are likely to occur,
- the foundations should be embedded at the depths that are out of the area where scour affects horizontal and side bearing capacities of the supports,

- the foundations should be protected against abrasion, which is caused by the bed material carried by the stream of water,
- shallow foundations should be connected with the surrounding sheet piles, which minimizes the inclination of piers, in case local bed scour occurs in their proximity,
- the embankment under the driveways to the bridge should be protected against the river scour.

6. Conclusions

The study was aimed at investigation of mass particles trajectories around a pier. Simulations for a limited range of mean flow conditions indicate that the particles trajectories depend on intensity of wake vertical vortices being the main driving force moving the particles out of the scour hole. These flow objects are highly unsteady and demand sufficiently detailed modelling approach. LES has been shown to be efficient way of modelling turbulent flow around submerged objects.

Simulations confirm strong interdependence of horseshoe vortex system and wake vertical vortices. Wake vortices originate as corner vortices near bed on left and right side of a pier (Figure 2c). Their character depends on horseshoe vortex strength which in turn changes much as a scour hole develops. Therefore, it is suggested that all the major flow structures around a pier (down flow, horseshoe and wake vortices) should be considered as a one system rather than separate objects. As these flow structures are responsible for scouring, investigating their mutual influence is a key to counteract their effects.

Acknowledgments

Most of the computations for the present work were carried out with the OpenFOAM CFD Toolbox [19] (http://www.openfoam.org) released from OpenCFD under the terms of the GNU GPL 2 license (http://www.gnu.org).

References

[1] Ashworth P.J., Bennett S.J., Best J.L., McLelland S.J.: *Coherent flow structures in open channels*, John Wiley & Sons, 1996.
[2] Berselli L.C., Iliescu T., Layton W.J.: *Mathematics of large eddy simulation of turbulent flows*, Springer-Verlag, 2006.
[3] Breusers H.N.C., Raudkivi A.J.: *Bubbles, drops and particles*, Academic Press, 1991.
[4] Clift R., Grace J.R., Weber M.E.: *Bubbles, drops and particles*, Academic Press, 1978.
[5] de Villiers E.: *The potential of large eddy simulation for the modelling of wall bounded flows*, PhD thesis, Imperial College of Science, Technology and Medicine, London – not published yet (private correspondence), 2006.
[6] Dey S., Raikar R.V.: *Characteristics of horseshoe vortex in developing scour holes at piers*, Journal of Hydraulic Engineering, Vol. 133, No. 4, 2007, pp. 399–413.
[7] Ferziger J.H., Peric M.: *Computational methods for fluid dynamics*, Springer, 1999.

[8] Graf W.H., Istiarto I.: *Flow pattern in the scour hole around a cylinder*, Journal of Hydraulic Research, Vol. 40, No. 1, 2002, pp. 13–20.
[9] Issa R.I.: *Solution of the implicitly discretized fluid flow equations by operator splitting*, Journal of Computatinal Physics, Vol. 62, 1986, pp. 40–65.
[10] Kirkil G., Constantinescu G., Ettema R.: *The horseshoe vortex system around a circular bridge pier on equilibrium scoured bed*, ASCE Conference Proceedings, Vol. 173, 2005, pp. 414–414.
[11] Leszczyński J.S.: *Dyskretny model dynamiki zderzeń ziaren w przepływach materiałów granulowanych*, Wydawnictwa Politechniki Częstochowskiej, 2005.
[12] Liu X., Garcia M.H.: *Numerical simulation of local scour with free surface and automatic mesh deformation*, In: Examining the Confluence of Environmental and Water Concerns, IAHR, 2006.
[13] Nordin N.P.A.: *Complex chemistry modelling of diesel spray combustion*, PhD thesis, Chalmers University of Technology, 2001.
[14] Pasiok R., Popow A.: *A numerical free surface flow model in the analysis of a bed stability at piers*, Proceedings of XXIV International School of Hydraulics, Gdańsk, 2004.
[15] Sagaut P.: *Large eddy simulation for incompressible flows*, Springer, 1998.
[16] Stilger-Szydło E.: *Posadowienia obiektów infrastruktury transportu lądowego. Teoria – projektowanie – realizacja*, DWE, Wrocław, 2005.
[17] Unger J., Hager W.: *Down-flow and horseshoe vortex characteristics of sediment embedded bridge piers*, Experiments in Fluids, Vol. 42, No. 1, 2007, pp. 1–19.
[18] Van der Vorst H.A.: *Bi-CGSTAB: a fast and smoothly converging variant of Bi-CG for the solution of non-symmetric linear systems*, SIAM Journal of Scientific Computing, Vol. 13, No. 2, 1992, pp. 631–644.
[19] Weller H., Tabor G., Jasak H., Fureby C.: *A tensorial approach to computational continuum mechanics using object oriented techniques*, Computers in Physics, Vol. 12, No. 6, 1998, pp. 620–631.
[20] Wilcox D.: *Turbulence modelling for CFD*, DCW Industries Inc., 2000.
[21] *The decree of the ministry of transportation and marine economy, 30.05.1998, concerning technical conditions required from road engineering structures and their location*, DzU (Law Gazette), 3.08.2000.
[22] Melville B.W., Coleman S.E.: *Bridge scour*, Water Resources Publications, Colorado, USA, 2000.

Rozmycia i symulowanie przepływu turbulentnego przy filarach mostowych

Brakuje w literaturze opracowań naukowych z zakresu badań mechanizmów transportu ziaren materiału dna z dołu rozmycia. Niniejsza pracę należy zaliczyć do prac nowatorskich. Rozpatruje ona mechanizmy rozmywania lokalnego, związanego z istnieniem filaru mostowego. Do zdobycia informacji o polu przepływu wykorzystano odpowiednio sformułowany numeryczny model przepływu, tzw. symulację dużych wirów (LES – *large-eddy simulation*). Przeprowadzone w niniejszej pracy analizy numeryczne, badające mechanizmy transportu ziaren materiału dna z wykorzystaniem odpowiednio sformułowanego numerycznego modelu przepływu, stanowią teoretyczne podstawy analiz pola prędkości wokół filarów mostów. Analizy te będą pomocne przy obliczeniach hydraulicznych mostów.

ARCHIVES OF CIVIL AND MECHANICAL ENGINEERING

Vol. X 2010 No. 2

Mechanics of adhesive joints as a plane problem of the theory of elasticity. Part I: general formulation

P. RAPP
Poznań University of Technology, 5 M. Skłodowskiej-Curie Sq., 60-965 Poznań, Poland.

The subject of the paper is a formulation of a general model for adhesive joints within the frame of the plane linear theory of elasticity. Adherends can be of varying thickness and made of various anisotropic materials. The adhesive surface can be curvilinear. The shape of the adherends in the joint can be arbitrary. The adhesive joint can be loaded by shear stresses of any distribution on surfaces of adherends as well as by normal and shear stresses of any distribution on edges of adherends.

The general case is expressed in a displacements space with a set of four partial differential equations of the second order and in a stresses space by means of a set of six partial differential equations of the second order. In a specific case a set of two partial differential equations of the second order was formulated for shear stresses in the adhesive. The boundary conditions allow for a possibility of sharp edges for adherends.

Keywords: *adhesively bonded joints, analytical models, two-dimensional displacement-stress analysis, anisotropy, linear elasticity*

1. Introduction

Analytical methods of a stress calculation in adhesive joints were initiated by Volkersen in [10], where he formulated and solved a one-dimensional ordinary differential equation for a shear stress in an axially loaded lap joint. Later a number of papers describing analytical models of adhesive joints appeared. However, the majority of them still dealt with generalisations of axially loaded one-dimensional cases.

An analytical description of an adhesive joint is much complicated, if the joint is loaded by a complex plane system of forces. For such loaded joints two-dimensional models in the plane of the joint should be formulated.

First analytical models of a two-dimensional lap joint in the joint plane XY, loaded by constant stresses in the direction X were presented in the papers [1–2]. It was assumed, that the joint is plane, adherends are of a constant thickness and made of isotropic materials. In the analysis it was assumed, that shear stresses τ_{xy} in the adherends were zero. For each adherend a set of two partial differential equations of the second order with constant coefficients expressed in normal stresses σ_x and σ_y was formulated. Shear stresses in the adhesive, constituting a loading of the adherends were determined from simplified equilibrium equations for a plane stress state, where the

shear stress τ_{xy} was neglected. Introduction of further simplifications, i.e. neglecting a coupling of stresses σ_x and σ_y allowed to find two uncoupled ordinary differential equations, for which an analytical solution was given. Taking the Poisson's ratio into account it was shown, that the adherends loaded in the X direction are also deformed in the Y direction. The consequence of this fact is an appearance in the adhesive the stress τ_x in the load direction and the stress τ_y perpendicular to the load direction.

A more exact two-dimensional model of an adhesive joint based on the equations of the theory of elasticity was presented in the papers [6–7]. A rectangular joint consisting of one isotropic and one orthotropic adherend was considered. It was assumed, that the isotropic adherend was loaded on edges by constant normal stresses in the directions X and Y and a self-equilibrated set of constant shear stresses, while the orthotropic adherend was not loaded. The analysis was split into two stages: a bi-axial normal stress loading and a shear stress loading.

When considering the bi-axial normal stress loading the same simplifying assumptions were adopted and the same partial differential equations as in the papers [1–2] were obtained. Due to the simultaneous action of loading in two directions the equations were not simplified to a set of ordinary differential equations. The set of partial differential equations was solved using the Fourier series. The shear stresses τ_x and τ_y in the adhesive were calculated from simplified equilibrium equations, where the shear stress τ_{xy} in the adherends was neglected.

Considering the joint loaded by the shear stresses, simplified equilibrium equations were formulated. The normal stresses σ_x and σ_y in the adherends were neglected. The problem was formulated as a partial differential equation of the second order with respect to the shear stress τ_{xy} in the orthotropic adherend. This equation was solved using the Fourier series.

Earlier, in a similar way, rectangular and infinite band joints loaded by normal and shear stresses were analysed in the papers [4–5].

A current overview of analytical models of adhesive joints and their comparison is given in [3, 8–9].

Analytical models presented in the literature provide simplified solutions, where some components of the stress state are neglected in joint equilibrium equations. Also a partial neglecting of the coupling between the variables as well as simple cases of loading of adhesive joints is featured therein.

The purpose of this paper is a formulation of a general model of an adhesive joint, based on the plane stress problem of the theory of elasticity, which would be free of the above mentioned simplifications.

2. General model of a two-dimensional adhesive joint

The subject of the paper is an analysis of adhesive joints consisting of two thin sheet adherends with an adhesive in between. It is assumed, that the adherends are thin and have constant or gently varying thickness. The middle surfaces of adherends can be

plane or slightly curved. The adhesive between the adherends is thin and can have constant or gently varying thickness. Its middle surface can be plane or gently curved. An adherend is considered as thin if the ratio of its thickness and its dimension parallel to a direction of loading action is less or equal to 0.1. A gentle variation of the adherend thickness means, that absolute values of the first derivatives of the functions describing the thickness of the adherend do not exceed 0.2. The thickness of the adhesive is measured in the direction normal to its middle surface.

The adhesive joint is modelled as a plane two-dimensional system parallel to the plane 0XY in the orthogonal system of co-ordinates 0XYZ. Projections of the thin sheet adherends and the adhesive on the plane 0XY form identical figures of an arbitrary shape. Loading of the adhesive joint can consist of forces parallel to the plane 0XY distributed on surfaces and edges of the adherends.

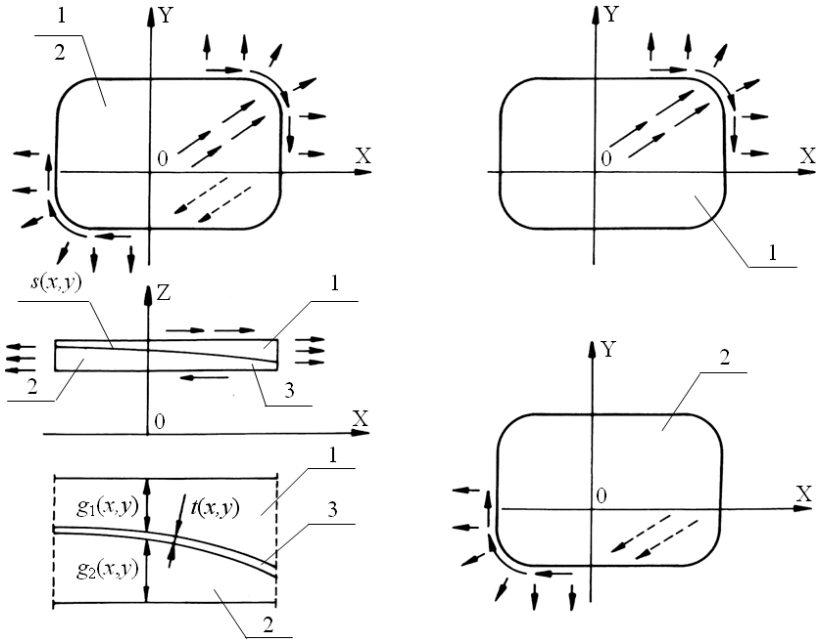

Fig. 1. Layout of an adhesive joint. 1 – adherend 1, 2 – adherend 2, 3 – adhesive

It is assumed, that the effects of bending and torsion of the thin sheet adherends are of secondary importance and can be neglected in the analysis. The thickness of the adherend is measured in the direction normal to the plane 0XY. Due to this and to the assumption, that the adherends are thin and have constant or gently varying thickness it is further assumed, that stresses across the adherend thickness are constant and form a plane stress state parallel to the plane 0XY. The thin sheet adherends of the joint are considered as plane elements parallel to the plane 0XY. The layout of the adhesive joint is presented in Figure 1. The thickness of the adherends 1 and 2 is described by

functions $g_1 = g_1(x, y)$ and $g_2 = g_2(x, y)$. It is assumed, that they are C^1 – continuous with respect to variables x, y. The functions g_1 and g_2 can be zero on some sections or in a neighbourhood of certain points on the adherends edges.

The middle surface of the adhesive is described by a function $s = s(x, y)$, which is assumed to be C^1 – continuous with respect to variables x, y. The adhesive thickness function $t = t(x, y)$ is positive and is C^1 – continuous with respect to variables x, y.

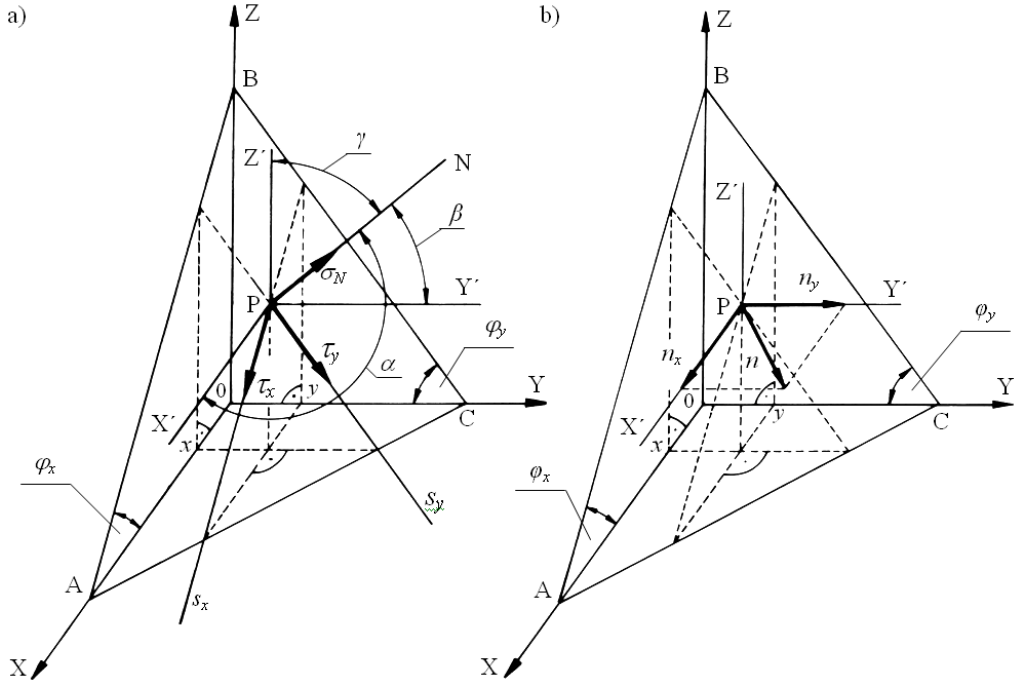

Fig. 2. The stresses in an adhesive

The adhesive is modelled as an isotropic linearly-elastic medium with stresses $\tau_x = \tau_x(x, y)$, $\tau_y = \tau_y(x, y)$ tangent to the adhesive middle surface and a stress $\sigma_N = \sigma_N(x, y)$ normal to the adhesive middle surface. The stress τ_x acts along the tangent s_x parallel to the plane 0YZ and the stress τ_y – along the tangent s_y parallel to the plane 0XZ (Figure 2a). It is assumed, that the stresses in the adhesive are constant across its thickness. As a result of an action of the shear stresses τ_x and τ_y in the adhesive, shear strains occur. They evoke relative displacements of adhesive layers in the directions tangent to the adhesive middle surface. The stress σ_N evokes strains in the adhesive, which are normal to the adhesive middle surface.

From the assumptions, that the adhesive joint is loaded by forces parallel to the plane 0XY and that the adherends undergo the plane stress state parallel to the plane 0XY it results, that a resultant $n = n(x, y)$ from the stresses τ_x, τ_y and σ_N is parallel to

the plane 0XY. Components of the stress n parallel to the axes X and Y are denoted as $n_x = n_x(x, y)$ and $n_y = n_y(x, y)$ (Figure 2b). The stresses n_x and n_y form actions from the adhesive on the adherends 1 and 2.

The angles φ_x, φ_y, α, β, γ and the stresses τ_x, τ_y, σ_N, n, n_x, n_y presented in Figure 2 are considered as positive. In particular, from these definitions it results, that angles φ_x, φ_y as the ones between the tangents to the adhesive middle surface s and the plane 0XY follow from the relations

$$\mathrm{tg}\phi_x = -\frac{\partial s}{\partial x}, \qquad \mathrm{tg}\phi_y = -\frac{\partial s}{\partial y}. \tag{1}$$

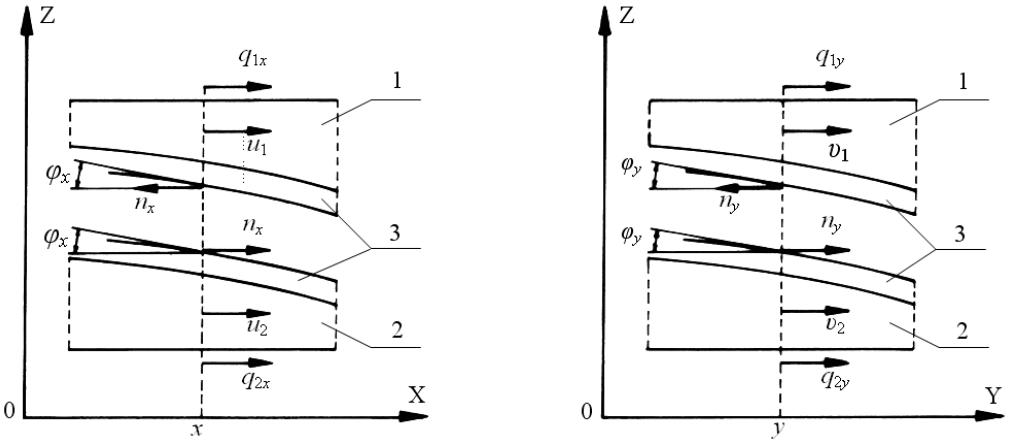

Fig. 3. Sketch of stresses in the adhesive and notation for displacements of adherends. 1 – adherend 1, 2 – adherend 2, 3 – adhesive cut along the middle surface

Displacements of the adherends 1 and 2 are described by functions $u_1 = u_1(x, y)$ and $u_2 = u_2(x, y)$ for the direction X and functions $v_1 = v_1(x, y)$ and $v_2 = v_2(x, y)$ for the direction Y. It is assumed, that the functions u_1, u_2, v_1 and v_2 are C^2 – continuous with respect to variables x, y.

Uniformly distributed loading on external surfaces of the adherends 1 and 2 expressed in terms of components parallel to the axes X and Y is denoted by $q_{1x} = q_{1x}(x, y)$, $q_{2x} = q_{2x}(x, y)$ and $q_{1y} = q_{1y}(x, y)$, $q_{2y} = q_{2y}(x, y)$. The loading components are positive when acting with the orientation of the axes X and Y. The stresses n_x, n_y in the adhesive, the external loading q_{1x}, q_{2x}, q_{1y}, q_{2y} and the displacements u_1, u, v, v_2 of the adherends 1 and 2 are shown in Figure 3.

Let ABC denote a plane tangent to the middle surface s of the adhesive at a point P with co-ordinates x, y (Figure 2). Axes X′, Y′, Z′ are parallel to the axes X, Y, Z. The tangent lines s_x and s_y, along which the stresses τ_x, τ_y act, lie in the plane ABC and are parallel to sections AB and BC, respectively. Hence, their slopes to the plane 0XY are

φ_x and φ_y, respectively. A sum of projections of components of the stresses τ_x, τ_y and σ_N along the axis Z′ is zero. Hence,

$$\sigma_N \cos\gamma - \tau_x \sin\phi_x - \tau_y \sin\phi_y = 0. \tag{2}$$

The stresses n_x, n_y in the adhesive can be expressed as

$$n_x = \tau_x \cos\phi_x + \sigma_N \cos\alpha, \tag{3.1}$$

$$n_y = \tau_y \cos\phi_y + \sigma_N \cos\beta. \tag{3.2}$$

Calculating σ_N from (2) and substituting it to (3.1–2) one gets

$$n_x = \tau_x\left(\cos\varphi_x + \frac{\cos\alpha}{\cos\gamma}\sin\varphi_x\right) + \tau_y \frac{\cos\alpha}{\cos\gamma}\sin\varphi_y, \tag{4.1}$$

$$n_y = \tau_x \frac{\cos\beta}{\cos\gamma}\sin\varphi_x + \tau_y\left(\cos\varphi_y + \frac{\cos\beta}{\cos\gamma}\sin\varphi_y\right). \tag{4.2}$$

The slope of the plane ABC with respect to the axes of the co-ordinate system 0XYZ (Figure 2) is uniquely defined by the angles φ_x, φ_y. Hence, angles α, β and γ can be expressed in terms of the angles φ_x, φ_y. This yields

$$\mathrm{tg}\alpha = \frac{\sqrt{1+\mathrm{tg}^2\phi_y}}{\mathrm{tg}\phi_x}, \qquad \mathrm{tg}\,\beta = \frac{\sqrt{1+\mathrm{tg}^2\phi_x}}{\mathrm{tg}\phi_y}, \qquad \mathrm{tg}\,\gamma = \sqrt{\mathrm{tg}^2\phi_x + \mathrm{tg}^2\phi_y}\ .$$

From this the following formulae result

$$\cos\alpha = \frac{1}{\sqrt{1+\mathrm{tg}^2\alpha}} = \frac{\mathrm{tg}\phi_x}{\sqrt{1+\mathrm{tg}^2\phi_x+\mathrm{tg}^2\phi_y}},$$

$$\cos\beta = \frac{1}{\sqrt{1+\mathrm{tg}^2\beta}} = \frac{\mathrm{tg}\phi_y}{\sqrt{1+\mathrm{tg}^2\phi_x+\mathrm{tg}^2\phi_y}},$$

$$\cos\gamma = \frac{1}{\sqrt{1+\mathrm{tg}^2\gamma}} = \frac{1}{\sqrt{1+\mathrm{tg}^2\phi_x+\mathrm{tg}^2\phi_y}}$$

$$\frac{\cos\alpha}{\cos\gamma} = \mathrm{tg}\phi_x, \qquad \frac{\cos\beta}{\cos\gamma} = \mathrm{tg}\phi_y. \tag{5}$$

Taking advantage of (5), equations (4.1–2) can be written down in the form

$$n_x = \tau_x\left(\cos\varphi_x + \mathrm{tg}\varphi_x \sin\varphi_x\right) + \tau_y \mathrm{tg}\varphi_x \sin\varphi_y, \tag{6.1}$$

$$n_y = \tau_x \mathrm{tg}\varphi_y \sin\varphi_x + \tau_y\left(\cos\varphi_y + \mathrm{tg}\varphi_y \sin\varphi_y\right). \tag{6.2}$$

The shear stresses τ_x and τ_y expressed in terms of n_x and n_y can be obtained from the equations (6.1–2), and the stress σ_N – from the formula (2). This yields

$$\tau_x = \frac{\cos\varphi_x}{1-\sin^2\varphi_x \sin^2\varphi_y} n_x - \frac{\sin\varphi_x \sin\varphi_y \cos\varphi_y}{1-\sin^2\kappa_x \sin^2\varphi_y} n_y, \tag{7.1}$$

$$\tau_y = -\frac{\sin\varphi_x \sin\varphi_y \cos\varphi_x}{1-\sin^2\varphi_x \sin^2\varphi_y} n_x + \frac{\cos\varphi_y}{1-\sin^2\varphi_x \sin^2\varphi_y} n_y, \tag{7.2}$$

$$\sigma_N = \left(\tau_x \sin\phi_x + \tau_y \sin\phi_y\right)\sqrt{1+\mathrm{tg}^2\phi_x + \mathrm{tg}^2\phi_y}. \tag{8}$$

3. General equilibrium equations for adherends

The stress state at a point of an adherend k (k = 1, 2) is determined by a normal stress $\sigma_{kx} = \sigma_{kx}(x, y)$, $\sigma_{ky} = \sigma_{ky}(x, y)$ and shear stresses $\tau_{kxy} = \tau_{kxy}(x, y)$ – Figure 4. It is assumed, that the functions σ_{kx}, σ_{ky}, τ_{kxy} are C^2 – continuous with respect to variables x, y.

An element of the adherend k (k = 1, 2) with dimensions dx, dy is loaded by forces q_{kx}, q_{ky} distributed on external surfaces of the adherends, stresses n_x and n_y in the adhesive and internal forces in adherends acting at cross-sections normal to the plane 0XY. In the adherend 1 the stresses n_x and n_y have a negative orientation and in the adherend 2 – a positive one, according to the notation presented in Figures 2 and 3. Hence, the stresses n_x and n_y acting on the adherend k (k = 1, 2) can be expressed as $(-1)^k n_x$ and $(-1)^k n_y$. Integration of the stresses σ_{kx}, σ_{ky} and τ_{kxy} across the thickness of the adherend k yields internal normal and shear forces related to the unit length dx or dy of the rectangle $dx \times dy$

$$N_{kx} = \sigma_{kx}\, g_k, \qquad N_{ky} = \sigma_{ky}\, g_k, \qquad T_{kxy} = \tau_{kxy}\, g_k. \tag{9}$$

The internal forces and loading of the element of the adhesive joint are shown in Figure 5. Taking into account the fact, that the stresses $(-1)^k n_x$, $(-1)^k n_y$ (k = 1, 2) are

distributed on the surface $s(x, y)$, which is oriented with respect to the axes X and Y by the angles φ_x, φ_y, equilibrium equations of the element of the adherend k can be expressed in the form

$$\frac{\partial N_{kx}}{\partial x}+\frac{\partial T_{kxy}}{\partial y}+(-1)^k\frac{\sqrt{1-\sin^2\varphi_x\sin^2\varphi_y}}{\cos\varphi_x\cos\varphi_y}n_x+q_{kx}=0, \tag{10.1}$$

$$\frac{\partial T_{kxy}}{\partial x}+\frac{\partial N_{ky}}{\partial y}+(-1)^k\frac{\sqrt{1-\sin^2\varphi_x\sin^2\varphi_y}}{\cos\varphi_x\cos\varphi_y}n_y+q_{ky}=0. \tag{10.2}$$

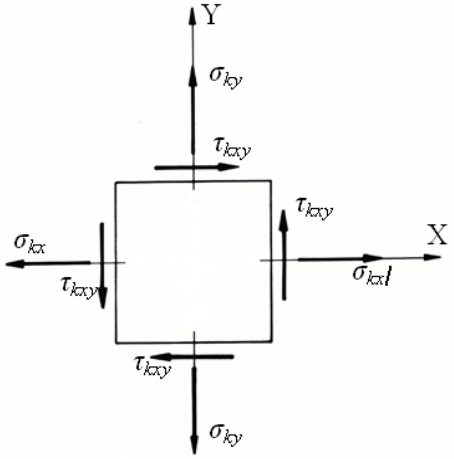

Fig. 4. The stress state in an adherend

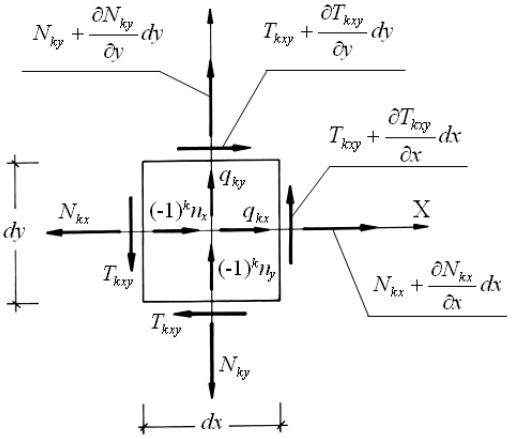

Fig. 5. Internal forces and loads acting on an element of an adherend

Taking advantage of the relations (9) in the Equations (10.1–2), the general equilibrium equations for the adherends (k = 1, 2) are obtained

$$\frac{\partial\sigma_{kx}}{\partial x}g_k+\frac{\partial\tau_{kxy}}{\partial y}g_k+\sigma_{kx}\frac{\partial g_k}{\partial x}+\tau_{kxy}\frac{\partial g_k}{\partial y}+(-1)^k\frac{\sqrt{1-\sin^2\varphi_x\sin^2\varphi_y}}{\cos\varphi_x\cos\varphi_y}n_x+q_{kx}=0, \tag{11.1}$$

$$\frac{\partial\tau_{kxy}}{\partial x}g_k+\frac{\partial\sigma_{ky}}{\partial y}g_k+\tau_{kxy}\frac{\partial g_k}{\partial x}+\sigma_{ky}\frac{\partial g_k}{\partial y}+(-1)^k\frac{\sqrt{1-\sin^2\varphi_x\sin^2\varphi_y}}{\cos\varphi_x\cos\varphi_y}n_y+q_{ky}=0. \tag{11.2}$$

4. Constitutive equations for adherends

It is assumed, that the adherends 1 and 2 are made of anisotropic materials. Linear strains in the directions of the axes X and Y are denoted by ε_{kx}, ε_{ky}, respectively, and γ_{kxy} denotes a shear strain for the adherend k (k = 1, 2) in the plane 0XY. With the assumption of the general anisotropy a physical law for the adherends 1 and 2 takes the form

$$\sigma_{kx} = s_{k11}\,\varepsilon_{kx} + s_{k12}\,\varepsilon_{ky} + s_{k13}\,\gamma_{kxy}, \tag{12.1}$$

$$\sigma_{ky} = s_{k21}\,\varepsilon_{kx} + s_{k22}\,\varepsilon_{ky} + s_{k23}\,\gamma_{kxy}, \tag{12.2}$$

$$\tau_{kxy} = s_{k31}\,\varepsilon_{kx} + s_{k32}\,\varepsilon_{ky} + s_{k33}\,\gamma_{kxy}. \tag{12.3}$$

The matrix of the coefficients in the Equations (12.1–3) must be symmetric.

The coefficients s_{k11} ... in the physical law (12.1–3) for the both adherends are determined with respect to the common axes X and Y of the co-ordinate system 0XY.

Taking into account the Cauchy's geometric relations

$$\varepsilon_{kx} = \frac{\partial u_k}{\partial x}, \qquad \varepsilon_{ky} = \frac{\partial \upsilon_k}{\partial y}, \qquad \gamma_{kxy} = \frac{\partial u_k}{\partial y} + \frac{\partial \upsilon_k}{\partial x}, \tag{13}$$

one can express the constitutive relations for the adherend k (k = 1, 2) in the form

$$\sigma_{kx} = s_{k11}\frac{\partial u_k}{\partial x} + s_{k12}\frac{\partial \upsilon_k}{\partial y} + s_{k13}\left(\frac{\partial u_k}{\partial y} + \frac{\partial \upsilon_k}{\partial x}\right), \tag{14.1}$$

$$\sigma_{ky} = s_{k21}\frac{\partial u_k}{\partial x} + s_{k22}\frac{\partial \upsilon_k}{\partial y} + s_{k23}\left(\frac{\partial u_k}{\partial y} + \frac{\partial \upsilon_k}{\partial x}\right), \tag{14.2}$$

$$\tau_{kxy} = s_{k31}\frac{\partial u_k}{\partial x} + s_{k32}\frac{\partial \upsilon_k}{\partial y} + s_{k33}\left(\frac{\partial u_k}{\partial y} + \frac{\partial \upsilon_k}{\partial x}\right). \tag{14.3}$$

5. Constitutive equations for adhesive

As a result of an action of shear stresses τ_x and τ_y shear strains are evoked in an adhesive. They lead to relative displacements of the adhesive layers in the direction tangent to the adhesive middle surface. The stress σ_N causes the strain in the adhesive that is normal to its middle surface. The surfaces of contact between the adhesive and the

adherends 1 and 2 are called the external layers. Their spacing is equal to the adhesive thickness t. The relative displacements of the external layers of the adhesive in the tangent directions s_x, s_y and in the normal direction N are denoted as Δ_{sx}, Δ_{sy} and Δ_N, respectively (Figure 6a).

It is assumed, that adhesive material is linearly elastic. Its Young's and Kirchhoff's moduli are denoted as E_s and G_s, respectively.

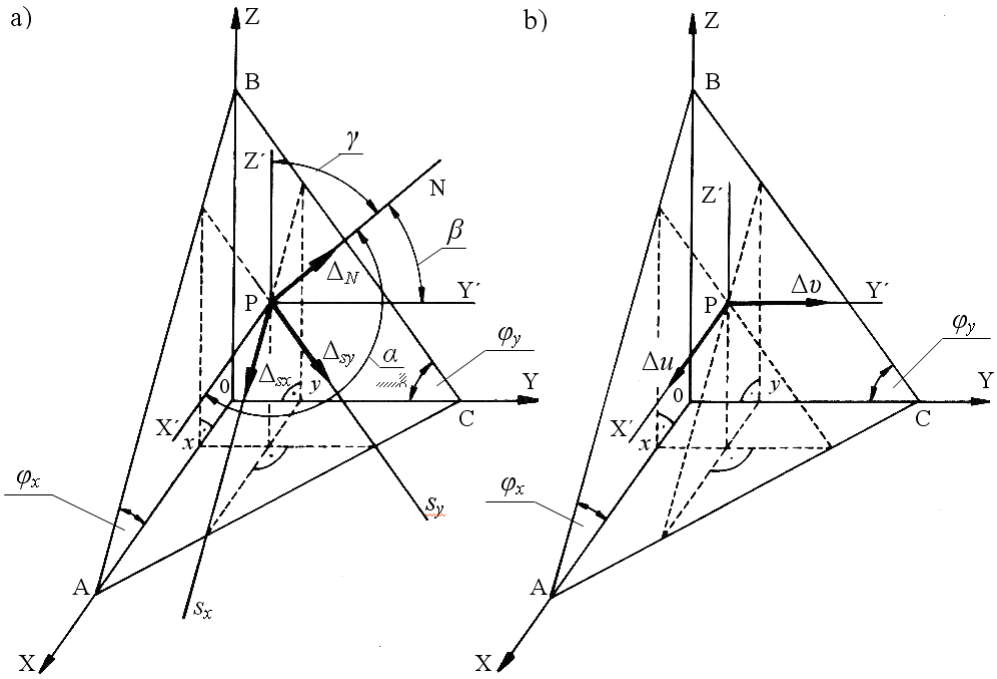

Fig. 6. Relative displacements of the external layers of the adhesive

A physical law for the adhesive with the thickness t takes the form

$$\Delta_{sx} = \frac{t}{G_s}\tau_x, \qquad \Delta_{sy} = \frac{t}{G_s}\tau_y, \qquad \Delta_N = \frac{t}{E_s}\sigma_N. \tag{15}$$

Differences of displacements of the adherends 1 and 2 on the surfaces of contact with the adhesive in the directions X and Y are denoted as (Figure 6b)

$$\Delta u = u_1 - u_2, \qquad \Delta v = v_1 - v_2. \tag{16}$$

In further considerations a relation between the displacements u_k and v_k of the adherends and the stresses n_x and n_y in the adhesive is necessary.

The differences of the displacements Δu and $\Delta \upsilon$ defined in (16) are equal to a sum of components of displacements Δ_{sx}, Δ_{sy}, Δ_N in the directions X′ and Y′. Hence, according to Figure 6a and taking into account, that the directions X′ and Δ_{sy} as well as Y′ and Δ_{sx} are orthogonal, one gets

$$\Delta u = \Delta_{sx} \cos\varphi_x + \Delta_N \cos\alpha, \tag{17.1}$$

$$\Delta \upsilon = \Delta_{sy} \cos\varphi_y + \Delta_N \cos\beta. \tag{17.2}$$

Substitution of (15) into the Equations (17.1–2) and using the notation (16) yields

$$u_1 - u_2 = \tau_x \frac{t}{G_s} \cos\varphi_x + \sigma_N \frac{t}{E_s} \cos\alpha, \tag{18.1}$$

$$\upsilon_1 - \upsilon_2 = \tau_y \frac{t}{G_s} \cos\varphi_y + \sigma_N \frac{t}{E_s} \cos\beta. \tag{18.2}$$

Substituting the stress σ_N expressed by (8) to the Equations (18.1–2) and using the formulae (5), one can rewrite the Equations (18.1–2) in the form

$$u_1 - u_2 = \tau_x \left(\frac{t}{G_s} + \frac{t}{E_s} \mathrm{tg}^2\varphi_x \right) \cos\varphi_x + \tau_y \frac{t}{E_s} \mathrm{tg}\varphi_x \mathrm{tg}\varphi_y \cos\varphi_y, \tag{19.1}$$

$$\upsilon_1 - \upsilon_2 = \tau_x \frac{t}{E_s} \mathrm{tg}\varphi_x \mathrm{tg}\varphi_y \cos\varphi_x + \tau_y \left(\frac{t}{G_s} + \frac{t}{E_s} \mathrm{tg}^2\varphi_y \right) \cos\varphi_y. \tag{19.2}$$

Relations between the displacements u_k and υ_k of the adherends 1 and 2 and the stresses n_x and n_y in the adhesive are obtained by an elimination of the shear stresses τ_x and τ_y from the Equations (6.1–2) and (19.1–2). This operation yields

$$n_x = \frac{G_s}{t} \left[\delta_u (u_1 - u_2) + \delta_{u\upsilon} (\upsilon_1 - \upsilon_2) \right], \tag{20.1}$$

$$n_y = \frac{G_s}{t} \left[\delta_{\upsilon u} (u_1 - u_2) + \delta_\upsilon (\upsilon_1 - \upsilon_2) \right], \tag{20.2}$$

where:

$$\delta_u = \frac{1+\mathrm{tg}^2\phi_x + \dfrac{G_s}{E_s}\mathrm{tg}^2\phi_y}{1+\dfrac{G_s}{E_s}(\mathrm{tg}^2\phi_x + \mathrm{tg}^2\phi_y)}, \qquad \delta_\upsilon = \frac{1+\dfrac{G_s}{E_s}\mathrm{tg}^2\phi_x + \mathrm{tg}^2\phi_y}{1+\dfrac{G_s}{E_s}(\mathrm{tg}^2\phi_x + \mathrm{tg}^2\phi_y)}, \tag{21.1}$$

$$\delta_{u\upsilon} = \delta_{\upsilon u} = \frac{\left(1-\dfrac{G_s}{E_s}\right)\mathrm{tg}\phi_x\,\mathrm{tg}\phi_y}{1+\dfrac{G_s}{E_s}(\mathrm{tg}^2\phi_x + \mathrm{tg}^2\phi_y)}. \tag{21.2}$$

The Equations (20.1–2) are considered as the constitutive equations for the adhesive.

6. General equations expressed in terms of displacements

General equations of a two-dimensional adhesive joint expressed in terms of displacements u_1, u_2 and υ_1, υ_2 are obtained from the equilibrium Equations (11.1–2) substituting the relations (14.1–3) and (20.1–2). After some algebra one gets a set of four elliptic differential equations of the second order with unknown displacements u_1, u_2, υ_1 and υ_2 for the adherends 1 and 2.

$$\left[s_{k11}\frac{\partial^2 u_k}{\partial x^2} + (s_{k13}+s_{k31})\frac{\partial^2 u_k}{\partial x\partial y} + s_{k33}\frac{\partial^2 u_k}{\partial y^2} + s_{k13}\frac{\partial^2 \upsilon_k}{\partial x^2} + (s_{k12}+s_{k33})\frac{\partial^2 \upsilon_k}{\partial x\partial y} + s_{k32}\frac{\partial^2 \upsilon_k}{\partial y^2}\right] g_k +$$

$$+\left(s_{k11}\frac{\partial u_k}{\partial x} + s_{k13}\frac{\partial u_k}{\partial y} + s_{k13}\frac{\partial \upsilon_k}{\partial x} + s_{k12}\frac{\partial \upsilon_k}{\partial y}\right)\frac{\partial g_k}{\partial x} + \left(s_{k31}\frac{\partial u_k}{\partial x} + s_{k33}\frac{\partial u_k}{\partial y} + s_{k33}\frac{\partial \upsilon_k}{\partial x} + s_{k32}\frac{\partial \upsilon_k}{\partial y}\right)\frac{\partial g_k}{\partial y} +$$

$$+(-1)^k a_u(u_1-u_2) + (-1)^k a_{u\upsilon}(\upsilon_1-\upsilon_2) + q_{kx} = 0, \tag{22.1}$$

$$\left[s_{k31}\frac{\partial^2 u_k}{\partial x^2} + (s_{k33}+s_{k21})\frac{\partial^2 u_k}{\partial x\partial y} + s_{k23}\frac{\partial^2 u_k}{\partial y^2} + s_{k33}\frac{\partial^2 \upsilon_k}{\partial x^2} + (s_{k23}+s_{k32})\frac{\partial^2 \upsilon_k}{\partial x\partial y} + s_{k22}\frac{\partial^2 \upsilon_k}{\partial y^2}\right] g_k +$$

$$+\left(s_{k31}\frac{\partial u_k}{\partial x} + s_{k33}\frac{\partial u_k}{\partial y} + s_{k33}\frac{\partial \upsilon_k}{\partial x} + s_{k32}\frac{\partial \upsilon_k}{\partial y}\right)\frac{\partial g_k}{\partial x} + \left(s_{k21}\frac{\partial u_k}{\partial x} + s_{k23}\frac{\partial u_k}{\partial y} + s_{k23}\frac{\partial \upsilon_k}{\partial x} + s_{k22}\frac{\partial \upsilon_k}{\partial y}\right)\frac{\partial g_k}{\partial y} +$$

$$+(-1)^k a_{\upsilon u}(u_1-u_2) + (-1)^k a_\upsilon(\upsilon_1-\upsilon_2) + q_{ky} = 0, \tag{22.2}$$

where $k = 1$ for the adherend 1 and $k = 2$ for the adherend 2.

In the Equations (22.1–2) the following notation was introduced:

$$a_u = \frac{\sqrt{1-\sin^2\varphi_x \sin^2\varphi_y}}{\cos\varphi_x \cos\varphi_y}\frac{G_s}{t}\delta_u, \qquad a_\upsilon = \frac{\sqrt{1-\sin^2\varphi_x \sin^2\varphi_y}}{\cos\varphi_x \cos\varphi_y}\frac{G_s}{t}\delta_\upsilon,$$

$$a_{u\upsilon} = \frac{\sqrt{1-\sin^2\varphi_x \sin^2\varphi_y}}{\cos\varphi_x \cos\varphi_y}\frac{G_s}{t}\delta_{u\upsilon}, \; a_{\upsilon u} = a_{u\upsilon}. \tag{23}$$

7. Boundary conditions

The adherends 1 and 2 are bounded by circumferential boundary surfaces normal to the plane 0XY. A width of the boundary surface is equal to the adherend thickness. Let p_{kx} and p_{ky} (k = 1, 2) denote stresses acting on the boundary surfaces of the adherend k. It is assumed, that the stresses p_{kx} and p_{ky} are parallel to the axes X and Y, respectively, and that they are constant across the thickness of the adherends. These stresses are considered as a known external boundary loading for the adherends in the plane parallel to 0XY. Let P(x_p, y_p) be an arbitrary point lying at an intersection line for the boundary surface and the middle surface of the adherend k. Besides the stresses p_{kx} and p_{ky}, also internal stresses σ_{kx}, σ_{ky}, τ_{kxy} distributed on the internal cross-sections orthogonal to the plane 0XY as well as a loading $\boldsymbol{X}_k$ and $\boldsymbol{Y}_k$ distributed on the surface of the adherend k (k = 1, 2), transformed to the plane parallel to 0XY (Figure 7), act on an elementary fragment of the adherend k in a neighbourhood of the point P. The element is oriented in the system of axes X′, Y′ parallel to X and Y. The external loads are

$$\boldsymbol{X}_k = (-1)^k \frac{\sqrt{1-\sin^2\varphi_x \sin^2\varphi_y}}{\cos\varphi_x \cos\varphi_y} n_x + q_{kx}, \tag{24.1}$$

$$\boldsymbol{Y}_k = (-1)^k \frac{\sqrt{1-\sin^2\varphi_x \sin^2\varphi_y}}{\cos\varphi_x \cos\varphi_y} n_y + q_{ky}, \tag{24.2}$$

where k = 1 for the adherend 1 and k = 2 for the adherend 2.

Equilibrium conditions of the boundary element in the adherend k (k = 1, 2) take the form

$$\sigma_{kx}\frac{g_k(x_1,y_1)+g_k(x_1,y_2)}{2}\Delta y + \tau_{kxy}\frac{g_k(x_1,y_1)+g_k(x_2,y_1)}{2}\Delta x$$

$$= \boldsymbol{X}_k \frac{\Delta x \Delta y}{2} + p_{kx} \frac{g_k(x_1, y_2) + g_k(x_2, y_1)}{2} \Delta s. \tag{25.1}$$

$$\tau_{kxy} \frac{g_k(x_1, y_1) + g_k(x_1, y_2)}{2} \Delta y + \sigma_{ky} \frac{g_k(x_1, y_1) + g_k(x_2, y_1)}{2} \Delta x$$

$$= \boldsymbol{Y}_k \frac{\Delta x \Delta y}{2} + p_{ky} \frac{g_k(x_1, y_2) + g_k(x_2, y_1)}{2} \Delta s. \tag{25.2}$$

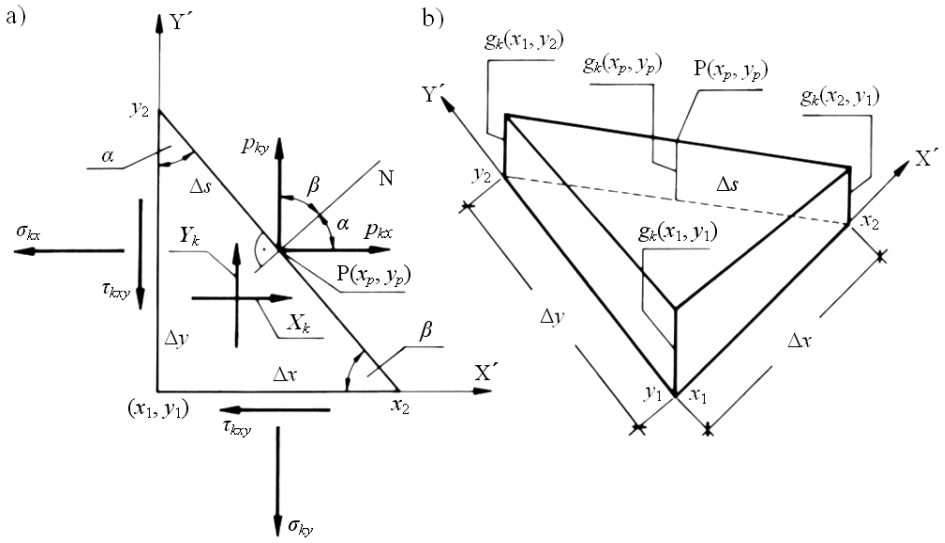

Fig. 7. The stress state at a boundary point of an adherend

In Figure 7b one can observe, that:

$$g_k(x_1, y_1) = g_k(x_2, y_1) - \frac{g_k(x_2, y_1) - g_k(x_1, y_1)}{\Delta x} \Delta x, \tag{26}$$

$$g_k(x_1, y_1) = g_k(x_1, y_2) - \frac{g_k(x_1, y_2) - g_k(x_1, y_1)}{\Delta y} \Delta y. \tag{27}$$

After substitution of the quantities g_k (x_1, y_1) from the formula (26) to the first components of the Equations (25.1–2), and from the formula (27) to the second components of these equations and observing, that $\Delta y/\Delta s = \cos\alpha = l$ and $\Delta x/\Delta s = \cos\beta = m$ one gets

$$\left(\sigma_{kx}\, l + \tau_{kxy}\, m\right)\frac{g_k(x_1,y_2)+g_k(x_2,y_1)}{2} = \; p_{kx}\,\frac{g_k(x_1,y_2)+g_k(x_2,y_1)}{2} +$$

$$+\frac{\Delta x\Delta y}{2\Delta s}\left(\sigma_{kx}\,\frac{g_k(x_2,y_1)-g_k(x_1,y_1)}{\Delta x}+\tau_{kxy}\,\frac{g_k(x_1,y_2)-g_k(x_1,y_1)}{\Delta y}+\boldsymbol{X}_k\right), \tag{28.1}$$

$$\left(\tau_{kxy}\, l + \sigma_{ky}\, m\right)\frac{g_k(x_1,y_2)+g_k(x_2,y_1)}{2} = \; p_{ky}\,\frac{g_k(x_1,y_2)+g_k(x_2,y_1)}{2} +$$

$$+\frac{\Delta x\Delta y}{2\Delta s}\left(\tau_{kxy}\,\frac{g_k(x_2,y_1)-g_k(x_1,y_1)}{\Delta x}+\sigma_{ky}\,\frac{g_k(x_1,y_2)-g_k(x_1,y_1)}{\Delta y}+\boldsymbol{Y}_k\right). \tag{28.2}$$

On the base of the equations (28.1–2) separate boundary conditions for the special edges: "non-sharp" with $g_k(x_p, y_p) > 0$ and "sharp" with $g_k(x_p, y_p) = 0$ can be formulated.

If $\Delta x \to 0$ and $\Delta y \to 0$, then $x_1, x_2 \to x_p$ and $y_1, y_2 \to y_p$. Also

$$g_k(x_1, y_1),\ g_k(x_2, y_1),\ g_k(x_1, y_2) \to g(x_p, y_p), \tag{29}$$

$$\frac{\Delta x\Delta y}{\Delta s} = \frac{1}{\sqrt{\dfrac{1}{\Delta x^2}+\dfrac{1}{\Delta y^2}}} \to 0\,, \tag{30}$$

$$\frac{g_k(x_2,y_1)-g_k(x_1,y_1)}{\Delta x} \to \left.\frac{\partial g_k(x,y)}{\partial x}\right|_{x=x_p,\, y=y_p}, \tag{31}$$

$$\frac{g_k(x_1,y_2)-g_k(x_1,y_1)}{\Delta y} \to \left.\frac{\partial g_k(x,y)}{\partial y}\right|_{x=x_p,\, y=y_p}. \tag{32}$$

Case 1. A non-sharp edge with $g_k(x_p, y_p) > 0$

Taking the limits $\Delta x \to 0$, $\Delta y \to 0$ in the Equations (28.1–2) and considering the conditions (29) – (32) one gets:

$$(\sigma_{kx}\, l + \tau_{kxy}\, m)\, g_k(x_p, y_p) = p_{kx}\, g_k(x_p, y_p), \tag{33.1}$$

$$(\tau_{kxy}\, l + \sigma_{ky}\, m)\, g_k(x_p, y_p) = p_{ky}\, g_k(x_p, y_p), \tag{33.2}$$

Hence, the known boundary conditions for the plane element in the plane state of stress are obtained

$$\sigma_{kx}\, l + \tau_{kxy}\, m = p_{kx}, \tag{34.1}$$

$$\tau_{kxy}\, l + \sigma_{ky}\, m = p_{ky}\,. \tag{34.2}$$

Substitution of the constitutive Equations (14.1–3) to (34.1–2) yields the final form of the boundary conditions for the non-sharp edge

$$\left[s_{k11}\frac{\partial u_k}{\partial x} + s_{k12}\frac{\partial \upsilon_k}{\partial y} + s_{k13}\left(\frac{\partial u_k}{\partial y} + \frac{\partial \upsilon_k}{\partial x}\right)\right] l$$

$$+\left[s_{k31}\frac{\partial u_k}{\partial x} + s_{k32}\frac{\partial \upsilon_k}{\partial y} + s_{k33}\left(\frac{\partial u_k}{\partial y} + \frac{\partial \upsilon_k}{\partial x}\right)\right] m = p_{kx}, \tag{35.1}$$

$$\left[s_{k31}\frac{\partial u_k}{\partial x} + s_{k32}\frac{\partial \upsilon_k}{\partial y} + s_{k33}\left(\frac{\partial u_k}{\partial y} + \frac{\partial \upsilon_k}{\partial x}\right)\right] l$$

$$+\left[s_{k21}\frac{\partial u_k}{\partial x} + s_{k22}\frac{\partial \upsilon_k}{\partial y} + s_{k23}\left(\frac{\partial u_k}{\partial y} + \frac{\partial \upsilon_k}{\partial x}\right)\right] m = p_{ky}, \tag{35.2}$$

where $k = 1$ for the adherend 1 and $k = 2$ for the adherend 2.

Case 2. A sharp edge with $g_k(x_p, y_p) = 0$

It was assumed, that the adherend thickness could be equal to zero on some sections or in a neighbourhood of certain points on the adherend edge. If $g_k(x_p, y_p) = 0$ at the point (x_p, y_p), then the real numbers $\delta_x > 0$ and $\delta_y > 0$ exist, such that $g_k(x, y) = 0$ for $x \in (x_p - \delta_x, x_p + \delta_x)$ and $y \in (y_p - \delta_y, y_p + \delta_y)$. Hence, if $0 < \Delta x < \delta_x$ and $0 < \Delta y < \delta_y$, then $g_k(x_1, y_1) = g_k(x_2, y_1) = g_k(x_1, y_2) = 0$. So the Equations (28.1–2) can be written down in the form:

$$\frac{\Delta x \Delta y}{2\Delta s}\left(\sigma_{kx}\frac{g_k(x_2, y_1) - g_k(x_1, y_1)}{\Delta x} + \tau_{kxy}\frac{g_k(x_1, y_2) - g_k(x_1, y_1)}{\Delta y} + \boldsymbol{X}_k \right) = 0, \tag{36.1}$$

$$\frac{\Delta x \Delta y}{2\Delta s}\left(\tau_{kxy}\frac{g_k(x_2, y_1) - g_k(x_1, y_1)}{\Delta x} + \sigma_{ky}\frac{g_k(x_1, y_2) - g_k(x_1, y_1)}{\Delta y} + \boldsymbol{Y}_k \right) = 0. \tag{36.2}$$

After taking into account, that $\frac{\Delta x \Delta y}{\Delta s} > 0$, the Equations (36.1–2) yield

$$\sigma_{kx} \frac{g_k(x_2, y_1) - g_k(x_1, y_1)}{\Delta x} + \tau_{kxy} \frac{g_k(x_1, y_2) - g_k(x_1, y_1)}{\Delta y} + \boldsymbol{X}_k = 0, \tag{37.1}$$

$$\tau_{kxy} \frac{g_k(x_2, y_1) - g_k(x_1, y_1)}{\Delta x} + \sigma_{ky} \frac{g_k(x_1, y_2) - g_k(x_1, y_1)}{\Delta y} + \boldsymbol{Y}_k = 0. \tag{37.2}$$

Despite that the values $g_k(x_2, y_1)$ and $g_k(x_1, y_2)$ are zero, explicit forms of the difference quotients of the function g_k are kept in the Equations (37.1–2). In the limits $\Delta x \to 0$, $\Delta y \to 0$ and taking into account (31) and (32), from the Equations (37.1–2) the following conditions are obtained

$$\sigma_{kx} \left.\frac{\partial g_k(x,y)}{\partial x}\right|_{x=x_p, y=y_p} + \tau_{kxy} \left.\frac{\partial g_k(x,y)}{\partial y}\right|_{x=x_p, y=y_p} + \boldsymbol{X}_k = 0, \tag{38.1}$$

$$\tau_{kxy} \left.\frac{\partial g_k(x,y)}{\partial x}\right|_{x=x_p, y=y_p} + \sigma_{ky} \left.\frac{\partial g_k(x,y)}{\partial y}\right|_{x=x_p, y=y_p} + \boldsymbol{Y}_k = 0. \tag{38.2}$$

The final form of the boundary conditions for the sharp edge is determined, when the constitutive Equations (14.1–3) and the formulae (24) with (20.1–2) and (23) are substituted to the conditions (38.1–2). After these calculations one gets

$$\left(s_{k11}\frac{\partial u_k}{\partial x} + s_{k13}\frac{\partial u_k}{\partial y} + s_{k13}\frac{\partial \upsilon_k}{\partial x} + s_{k12}\frac{\partial \upsilon_k}{\partial y}\right)\frac{\partial g_k}{\partial x} + \left(s_{k31}\frac{\partial u_k}{\partial x} + s_{k33}\frac{\partial u_k}{\partial y} + s_{k33}\frac{\partial \upsilon_k}{\partial x} + s_{k32}\frac{\partial \upsilon_k}{\partial y}\right)\frac{\partial g_k}{\partial y}$$

$$+ (-1)^k a_u (u_1 - u_2) + (-1)^k a_{u\upsilon} (\upsilon_1 - \upsilon_2) + q_{kx} = 0, \tag{39.1}$$

$$\left(s_{k31}\frac{\partial u_k}{\partial x} + s_{k33}\frac{\partial u_k}{\partial y} + s_{k33}\frac{\partial \upsilon_k}{\partial x} + s_{k32}\frac{\partial \upsilon_k}{\partial y}\right)\frac{\partial g_k}{\partial x} + \left(s_{k21}\frac{\partial u_k}{\partial x} + s_{k23}\frac{\partial u_k}{\partial y} + s_{k23}\frac{\partial \upsilon_k}{\partial x} + s_{k22}\frac{\partial \upsilon_k}{\partial y}\right)\frac{\partial g_k}{\partial y}$$

$$+ (-1)^k a_{\upsilon u} (u_1 - u_2) + (-1)^k a_{\upsilon} (\upsilon_1 - \upsilon_2) + q_{ky} = 0, \tag{39.2}$$

where $k = 1$ for the adherend 1 and $k = 2$ for the adherend 2.

It is evident, that the boundary conditions on the sharp edge have the identical form as the Equations (22.1–2) with $g_k = 0$ substituted. This statement allows for an exten-

sion of the conditions (39.1–2) as well for the case of an edge, which is sharp at a single point.

The boundary conditions for both, the non-sharp or sharp edge constitute equilibrium conditions, however the type of this equilibrium differs for these two cases.

The boundary conditions for the non-sharp edge express equilibrium of internal stresses in the adherend and the external stresses, which form a loading of the adherend. On the non-sharp edge the Equations (22.1–2) preserve their form, so the not sharp edge belongs to the domain of definition of the solution of these equations.
On the sharp edge (of zero thickness) stresses are not defined. In this case the boundary conditions express an internal equilibrium of stresses in the adherend at points with the extreme location at the sharp edge.

The sharp edge causes a singularity. The equations in displacements (22.1–2) are degenerate and take the form identical to the independently derived boundary conditions (39.1–2). Along the sharp edge the set of definiteness of the displacements equations is open. Hence, the sharp edge does not belong to the set of definiteness of the displacements equations for the adherend at which the sharp edge is found. In the case of the sharp edge the displacements equations are fulfilled in an open set, while at the sharp edge itself only the boundary conditions hold. The displacements and the resulting variables are determined on the sharp edge as the unilateral internal limits.

Static boundary conditions are not sufficient to achieve a uniqueness of a solution for the Equations (22.1–2). Indeed, if the functions $u_k(x, y)$ and $v_k(x, y)$ are solutions of the Equations (22.1–2), then the functions $u_k(x,y) - \theta y + u_0$, and $\upsilon_k(x,y) + \theta x + \upsilon_0$ are also solutions of these equations for arbitrary constants u_0 , v_0 , θ. It can be proved by a mere substitution. The constants u_0 and v_0 are interpreted as arbitrary displacements of the joint in the directions of the axes X and Y, while θ is interpreted as a small rotation of the joint about the origin of the co-ordinates system.

It results from these considerations, that in a class of solutions fulfilling the Equations (22.1–2) the adhesive joint has three degrees of freedom: two as a free body with respect to arbitrary displacements along the axes X and Y, and the third one as a free body with respect to a small rotation about the origin of the co-ordinates system.

To achieve the uniqueness of the solution for the Equations (22.1–2) kinematic boundary conditions must be enforced, restraining at least three degrees of freedom in order to make the adhesive joint stationary.

The points of restraining, which makes the system stationary should be treated as boundary points.

8. Equations for adherends expressed in terms of stresses

To get the full general analytical formulation it is also purposeful to express the equations for an adhesive joint in terms of stresses in the adherends.

Solving the Equations (20.1–2) with respect to $u_1 - u_2$ and $\upsilon_1 - \upsilon_2$ one gets

$$u_1 - u_2 = \frac{t\delta_\upsilon}{G_s(\delta_u\delta_\upsilon - \delta_{u\upsilon}\delta_{\upsilon u})} n_x - \frac{t\delta_{u\upsilon}}{G_s(\delta_u\delta_\upsilon - \delta_{u\upsilon}\delta_{\upsilon u})} n_y , \tag{40.1}$$

$$\upsilon_1 - \upsilon_2 = -\frac{t\delta_{\upsilon u}}{G_s(\delta_u\delta_\upsilon - \delta_{u\upsilon}\delta_{\upsilon u})} n_x + \frac{t\delta_u}{G_s(\delta_u\delta_\upsilon - \delta_{u\upsilon}\delta_{\upsilon u})} n_y . \tag{40.2}$$

Differentiation of these equations gives differences of strains in the adherends

$$\varepsilon_{1x} - \varepsilon_{2x} = \frac{\partial}{\partial x}(u_1 - u_2) = \frac{1}{G_s}\frac{\partial}{\partial x}\left[\frac{t\delta_\upsilon}{(\delta_u\delta_\upsilon - \delta_{u\upsilon}\delta_{\upsilon u})} n_x - \frac{t\delta_{u\upsilon}}{(\delta_u\delta_\upsilon - \delta_{u\upsilon}\delta_{\upsilon u})} n_y\right], \tag{41.1}$$

$$\varepsilon_{1y} - \varepsilon_{2y} = \frac{\partial}{\partial y}(\upsilon_1 - \upsilon_2) = \frac{1}{G_s}\frac{\partial}{\partial y}\left[-\frac{t\delta_{\upsilon u}}{(\delta_u\delta_\upsilon - \delta_{u\upsilon}\delta_{\upsilon u})} n_x + \frac{t\delta_u}{(\delta_u\delta_\upsilon - \delta_{u\upsilon}\delta_{\upsilon u})} n_y\right]. \tag{41.2}$$

A constitutive relation inverse to (12.1–3) can be expressed as

$$\varepsilon_{kx} = r_{k11}\,\sigma_{kx} + r_{k12}\,\sigma_{ky} + r_{k13}\,\tau_{kxy}, \tag{42.1}$$

$$\varepsilon_{ky} = r_{k21}\,\sigma_{kx} + r_{k22}\,\sigma_{ky} + r_{k23}\,\tau_{kxy}, \tag{42.2}$$

$$\gamma_{kxy} = r_{k31}\,\sigma_{kx} + r_{k32}\,\sigma_{ky} + r_{k33}\,\tau_{kxy}. \tag{42.3}$$

The stresses n_x and n_y determined from the Equations (11.1–2) have the form

$$n_x = (-1)^{k+1}\mu\left(\frac{\partial\sigma_{kx}}{\partial x}g_k + \frac{\partial\tau_{kxy}}{\partial y}g_k + \sigma_{kx}\frac{\partial g_k}{\partial x} + \tau_{kxy}\frac{\partial g_k}{\partial y}\right) + (-1)^{k+1}\mu q_{kx}, \tag{43.1}$$

$$n_y = (-1)^{k+1}\mu\left(\frac{\partial\tau_{kxy}}{\partial x}g_k + \frac{\partial\sigma_{ky}}{\partial y}g_k + \tau_{kxy}\frac{\partial g_k}{\partial x} + \sigma_{ky}\frac{\partial g_k}{\partial y}\right) + (-1)^{k+1}\mu q_{ky}, \tag{43.2}$$

where:

$$\mu = \frac{\cos\varphi_x \cos\varphi_y}{\sqrt{1 - \sin^2\varphi_x \sin^2\varphi_y}}.$$

General equations for the stresses in the adherends can be found from the Equations (41.1–2) after substitution of the expressions (42.1–3) and (43.1–2). These equations read:

$$r_{111}\sigma_{1x} - r_{211}\sigma_{2x} + r_{112}\sigma_{1y} - r_{212}\sigma_{2y} + r_{113}\tau_{1xy} - r_{213}\tau_{2xy}$$

$$= \frac{(-1)^{k+1}}{G_s}\frac{\partial}{\partial x}\left[\frac{t\delta_\upsilon\mu}{(\delta_u\delta_\upsilon - \delta_{u\upsilon}\delta_{\upsilon u})}\left(\frac{\partial\sigma_{kx}}{\partial x}g_k + \frac{\partial\tau_{kxy}}{\partial y}g_k + \sigma_{kx}\frac{\partial g_k}{\partial x} + \tau_{kxy}\frac{\partial g_k}{\partial y}\right)\right]$$

$$- \frac{(-1)^{k+1}}{G_s}\frac{\partial}{\partial x}\left[\frac{t\delta_{u\upsilon}\mu}{(\delta_u\delta_\upsilon - \delta_{u\upsilon}\delta_{\upsilon u})}\left(\frac{\partial\tau_{kxy}}{\partial x}g_k + \frac{\partial\sigma_{ky}}{\partial y}g_k + \tau_{kxy}\frac{\partial g_k}{\partial x} + \sigma_{ky}\frac{\partial g_k}{\partial y}\right)\right]$$

$$+ \frac{(-1)^{k+1}}{G_s}\frac{\partial}{\partial x}\left[\frac{t\delta_\upsilon\mu}{(\delta_u\delta_\upsilon - \delta_{u\upsilon}\delta_{\upsilon u})}q_{kx} - \frac{t\delta_{u\upsilon}\mu}{(\delta_u\delta_\upsilon - \delta_{u\upsilon}\delta_{\upsilon u})}q_{ky}\right], \tag{44.1}$$

$$r_{121}\sigma_{1x} - r_{221}\sigma_{2x} + r_{122}\sigma_{1y} - r_{222}\sigma_{2y} + r_{123}\tau_{1xy} - r_{223}\tau_{2xy}$$

$$= -\frac{(-1)^{k+1}}{G_s}\frac{\partial}{\partial y}\left[\frac{t\delta_{\upsilon u}\mu}{(\delta_u\delta_\upsilon - \delta_{u\upsilon}\delta_{\upsilon u})}\left(\frac{\partial\sigma_{kx}}{\partial x}g_k + \frac{\partial\tau_{kxy}}{\partial y}g_k + \sigma_{kx}\frac{\partial g_k}{\partial x} + \tau_{kxy}\frac{\partial g_k}{\partial y}\right)\right]$$

$$+ \frac{(-1)^{k+1}}{G_s}\frac{\partial}{\partial y}\left[\frac{t\delta_u\mu}{(\delta_u\delta_\upsilon - \delta_{u\upsilon}\delta_{\upsilon u})}\left(\frac{\partial\tau_{kxy}}{\partial x}g_k + \frac{\partial\sigma_{ky}}{\partial y}g_k + \tau_{kxy}\frac{\partial g_k}{\partial x} + \sigma_{ky}\frac{\partial g_k}{\partial y}\right)\right]$$

$$+ \frac{(-1)^{k+1}}{G_s}\frac{\partial}{\partial y}\left[-\frac{t\delta_{\upsilon u}\mu}{(\delta_u\delta_\upsilon - \delta_{u\upsilon}\delta_{\upsilon u})}q_{kx} + \frac{t\delta_u\mu}{(\delta_u\delta_\upsilon - \delta_{u\upsilon}\delta_{\upsilon u})}q_{ky}\right], \tag{44.2}$$

where $k = 1, 2$. Hence, four Equations (44.1–2) are obtained with six unknown stress functions σ_{1x}, σ_{1y}, τ_{1xy}, σ_{2x}, σ_{2y}, τ_{2xy} for the adherends 1 and 2. The set of Equations (44.1–2) must be completed with two equations of strain compatibility

$$\frac{\partial^2\varepsilon_{kx}}{\partial y^2} + \frac{\partial^2\varepsilon_{ky}}{\partial x^2} = \frac{\partial^2\tau_{kxy}}{\partial x\partial y}, \tag{45}$$

which for $k = 1, 2$ take the form (46) below

$$\frac{\partial^2(r_{k11}\sigma_{kx}+r_{k12}\sigma_{ky}+r_{k13}\tau_{kxy})}{\partial y^2}+\frac{\partial^2(r_{k21}\sigma_{kx}+r_{k22}\sigma_{ky}+r_{k23}\tau_{kxy})}{\partial x^2}$$

$$=\frac{\partial^2(r_{k31}\sigma_{kx}+r_{k32}\sigma_{ky}+r_{k33}\tau_{kxy})}{\partial x\partial y},$$

after substitution of the relations (42.1–3).

The boundary conditions for the stresses at non-sharp edges are given by the Equations (34.1–2). A sharp edge does not enter the domain of definition of the solution of the Equations (44.1–2) and (46). The boundary conditions for the stresses at the sharp edge are obtained from the Equations (44.1–2) with the adherend thickness $g_k = 0$ substituted. Stresses are not defined on the sharp edge. In order to avoid the singularity the sharp edge must be excluded from the set of definiteness of the Equations (44.1–2) and (46). At the sharp edge the equations in stresses are fulfilled in an open set, while on the sharp edge itself only the boundary conditions hold. The derivatives of stresses present in the boundary conditions must be considered as unilateral limits of the stress derivatives defined inside the domain of equations definiteness.

It should be pointed out, that all the quantities in brackets [ ] undergoing differentiation in the Equations (44.1–2) and (46) as well as in the boundary conditions for the sharp edges are functions of two variables.

Having found the stresses in the adherends, the quantities n_x and n_y can be calculated from the formulae (43.1–2) and then the stresses in the adhesive follow from the formulae (7.1–2) and (8).

9. Equations expressed in terms of stresses in the adhesive

An adhesive joint consisting of thin sheet adherends of a constant thickness g_1 and g_2 is considered. It is assumed, that the adhesive is plane and has a constant thickness t. The adherends and the adhesive are parallel to the plane 0XY. Assumptions on loading are the same as in the general case.

It is assumed, that the adherends 1 and 2 are made of the same anisotropic material. Hence, the physical law (12.1–3) for a material in both adherends 1 and 2 has an identical form

$$\sigma_x = s_{11}\,\varepsilon_x + s_{12}\,\varepsilon_y + s_{13}\,\gamma_{xy}, \tag{47.1}$$

$$\sigma_y = s_{21}\,\varepsilon_x + s_{22}\,\varepsilon_y + s_{23}\,\gamma_{xy}, \tag{47.2}$$

$$\tau_{xy} = s_{31}\,\varepsilon_x + s_{32}\,\varepsilon_y + s_{33}\,\gamma_{xy}. \tag{47.3}$$

The Equations (22.1–2) can be expressed as

$$s_{11}\frac{\partial^2 u_k}{\partial x^2}+\left(s_{13}+s_{31}\right)\frac{\partial^2 u_k}{\partial x\partial y}+s_{33}\frac{\partial^2 u_k}{\partial y^2}+s_{13}\frac{\partial^2 \upsilon_k}{\partial x^2}+\left(s_{12}+s_{33}\right)\frac{\partial^2 \upsilon_k}{\partial x\partial y}+s_{32}\frac{\partial^2 \upsilon_k}{\partial y^2}$$

$$+\left(-1\right)^k\frac{G_s}{tg_k}\left(u_1-u_2\right)+\frac{q_{kx}}{g_k}=0, \tag{48.1}$$

$$s_{31}\frac{\partial^2 u_k}{\partial x^2}+\left(s_{33}+s_{21}\right)\frac{\partial^2 u_k}{\partial x\partial y}+s_{23}\frac{\partial^2 u_k}{\partial y^2}+s_{33}\frac{\partial^2 \upsilon_k}{\partial x^2}+\left(s_{23}+s_{32}\right)\frac{\partial^2 \upsilon_k}{\partial x\partial y}+s_{k22}\frac{\partial^2 \upsilon_k}{\partial y^2}$$

$$+\left(-1\right)^k\frac{G_s}{\mathrm{tg}_k}\left(\upsilon_1-\upsilon_2\right)+\frac{q_{ky}}{g_k}=0, \tag{48.2}$$

where $k = 1$ for the adherend 1 and $k = 2$ for the adherend 2. Subtraction of the Equations (48.1–2) for $k = 2$ from the same equations for $k = 1$ yields

$$s_{11}\frac{\partial^2\left(u_1-u_2\right)}{\partial x^2}+\left(s_{13}+s_{31}\right)\frac{\partial^2\left(u_1-u_2\right)}{\partial x\partial y}+s_{33}\frac{\partial^2\left(u_1-u_2\right)}{\partial y^2}+$$

$$+s_{13}\frac{\partial^2\left(\upsilon_1-\upsilon_2\right)}{\partial x^2}+\left(s_{12}+s_{33}\right)\frac{\partial^2\left(\upsilon_1-\upsilon_2\right)}{\partial x\partial y}+s_{32}\frac{\partial^2\left(\upsilon_1-\upsilon_2\right)}{\partial y^2}-$$

$$-\frac{G_s}{t}\left(\frac{1}{g_1}+\frac{1}{g_2}\right)\left(u_1-u_2\right)+\left(\frac{q_{1x}}{g_1}-\frac{q_{2x}}{g_2}\right)=0, \tag{49.1}$$

$$s_{31}\frac{\partial^2\left(u_1-u_2\right)}{\partial x^2}+\left(s_{33}+s_{21}\right)\frac{\partial^2\left(u_1-u_2\right)}{\partial x\partial y}+s_{23}\frac{\partial^2\left(u_1-u_2\right)}{\partial y^2}+$$

$$+s_{33}\frac{\partial^2\left(\upsilon_1-\upsilon_2\right)}{\partial x^2}+\left(s_{23}+s_{32}\right)\frac{\partial^2\left(\upsilon_1-\upsilon_2\right)}{\partial x\partial y}+s_{22}\frac{\partial^2\left(\upsilon_1-\upsilon_2\right)}{\partial y^2}-$$

$$-\frac{G_s}{t}\left(\frac{1}{g_1}+\frac{1}{g_2}\right)\left(\upsilon_1-\upsilon_2\right)+\left(\frac{q_{1y}}{g_1}-\frac{q_{2y}}{g_2}\right)=0. \tag{49.2}$$

In the considered case it follows from the formulae (1), that

$$\phi_x = \phi_y = 0\,. \tag{50}$$

Hence, from the Equations (50) and (4) one gets

$$n_x = \tau_x\,, \qquad n_y = \tau_y\,, \tag{51}$$

and from the formula (8) –

$$\sigma_N = 0\,. \tag{52}$$

Taking advantage of the formulae (50), one gets from the equations (21.1–2)

$$\delta_u = \delta_\upsilon = 1\,, \qquad \delta_{u\upsilon} = \delta_{\upsilon u} = 0. \tag{53}$$

Hence, from (53) and the formulae (20.1–2) and (51) one gets

$$\tau_x = \frac{G_s}{t}(u_1 - u_2)\,, \qquad \tau_y = \frac{G_s}{t}(\upsilon_1 - \upsilon_2)\,. \tag{54}$$

The expressions (54) are the constitutive equations for the adhesive. Using these equations one may eliminate the displacements $u_1 - u_2$ and $\upsilon_1 - \upsilon_2$ from the Equations (49.1–2). In particular, multiplication of the Equations (49.1–2) by G_s/t and substitution of the expression (54), leads to the equations for the shear stresses τ_x and τ_y in the adhesive

$$s_{11}\frac{\partial^2\tau_x}{\partial x^2} + (s_{13} + s_{31})\frac{\partial^2\tau_x}{\partial x\partial y} + s_{33}\frac{\partial^2\tau_x}{\partial y^2} + s_{13}\frac{\partial^2\tau_y}{\partial x^2} + (s_{12} + s_{33})\frac{\partial^2\tau_y}{\partial x\partial y} + s_{32}\frac{\partial^2\tau_y}{\partial y^2}$$

$$-\frac{G_s}{t}\left(\frac{1}{g_1} + \frac{1}{g_2}\right)\tau_x + \frac{G_s}{t}\left(\frac{q_{1x}}{g_1} - \frac{q_{2x}}{g_2}\right) = 0, \tag{55.1}$$

$$s_{31}\frac{\partial^2\tau_x}{\partial x^2} + (s_{33} + s_{21})\frac{\partial^2\tau_x}{\partial x\partial y} + s_{23}\frac{\partial^2\tau_x}{\partial y^2} + s_{33}\frac{\partial^2\tau_y}{\partial x^2} + (s_{23} + s_{32})\frac{\partial^2\tau_y}{\partial x\partial y} + s_{22}\frac{\partial^2\tau_y}{\partial y^2} -$$

$$-\frac{G_s}{t}\left(\frac{1}{g_1} + \frac{1}{g_2}\right)\tau_y + \frac{G_s}{t}\left(\frac{q_{1y}}{g_1} - \frac{q_{2y}}{g_2}\right) = 0. \tag{55.2}$$

The boundary condition for the shear stresses τ_x and τ_y in the adhesive can be determined from the boundary conditions (35.1–2). In particular, writing down the conditions (35.1–2) for the constitutive relations (47.1–3) and carrying out an analogous procedure as in the derivation of the Equations (55.1–2), the boundary conditions for the Equations (55.1–2) expressed in terms of τ_x and τ_y are obtained

$$\left[s_{11}\frac{\partial \tau_x}{\partial x}+s_{12}\frac{\partial \tau_y}{\partial y}+s_{13}\left(\frac{\partial \tau_x}{\partial y}+\frac{\partial \tau_y}{\partial x}\right)\right]l+\left[s_{31}\frac{\partial \tau_x}{\partial x}+s_{32}\frac{\partial \tau_y}{\partial y}+s_{33}\left(\frac{\partial \tau_x}{\partial y}+\frac{\partial \tau_y}{\partial x}\right)\right]m=\frac{G_s}{t}(p_{1x}-p_{2x}), \tag{56.1}$$

$$\left[s_{31}\frac{\partial \tau_x}{\partial x}+s_{32}\frac{\partial \tau_y}{\partial y}+s_{33}\left(\frac{\partial \tau_x}{\partial y}+\frac{\partial \tau_y}{\partial x}\right)\right]l+\left[s_{21}\frac{\partial \tau_x}{\partial x}+s_{22}\frac{\partial \tau_y}{\partial y}+s_{23}\left(\frac{\partial \tau_x}{\partial y}+\frac{\partial \tau_y}{\partial x}\right)\right]m=\frac{G_s}{t}(p_{1y}-p_{2y}) \tag{56.2}$$

10. Discussion and final remarks

The results obtained in this paper can be related to a two-dimensional model of the adhesive joint based on the equations of the theory of elasticity presented in [6–7]. In these papers a rectangular joint was considered as made of an isotropic adherend described as a substrate s of the thickness g_s, to which the second adherend – a patch of the thickness g_p made from an orthotropic material, is attached. It was assumed, that the substrate was loaded at edges by a constant normal stress in X and Y directions and by a self-equilibrated system of shear stress. The patch was not loaded. The analysis was split into two stages: the influence of the two-directional normal stress loading and the influence of the shear stress loading.

In the stage with the two-directional normal stress the shear stress τ_{kxy} in the adherends in the OXY plane of the joint was assumed to be zero. For each adherend ($k = 1, 2$) a set of two partial differential equations of the second order with constant coefficients was obtained with the normal stresses σ_{kx} and σ_{ky}. They took the form:

$$\frac{\partial^2 \sigma_{kx}}{\partial x^2}=A_{kx}\sigma_{kx}+B_{kx}\sigma_{ky}+C_{kx}, \tag{57.1}$$

$$\frac{\partial^2 \sigma_{ky}}{\partial y^2}=A_{ky}\sigma_{ky}+B_{ky}\sigma_{kx}+C_{ky}, \tag{57.2}$$

where A_{kx}, B_{kx}, C_{kx} and A_{ky}, B_{ky}, C_{ky} are constants.

The set of second-order equations was transformed to two independent equations of the fourth order with constant coefficients:

$$\frac{\partial^4 \sigma_x^p}{\partial x^2 \partial y^2} + A_x \frac{\partial^2 \sigma_x^p}{\partial x^2} + B_x \frac{\partial^2 \sigma_x^p}{\partial y^2} + C_x \sigma_x^p + D_x = 0, \tag{58.1}$$

$$\frac{\partial^4 \sigma_y^p}{\partial x^2 \partial y^2} + A_y \frac{\partial^2 \sigma_y^p}{\partial x^2} + B_y \frac{\partial^2 \sigma_y^p}{\partial y^2} + C_y \sigma_y^p + D_y = 0, \tag{58.2}$$

where A_x, B_x, C_x, D_x and A_y, B_y, C_y, D_y are constants, while σ_x^p, σ_y^p denote the normal stresses in the patch in the directions X and Y. Equations (58.1–2) were solved using the Fourier series expansion. The shear stress in the adhesive in the plane stress state was found using the equilibrium equations

$$g_1 \frac{\partial \sigma_{1x}}{\partial x} = \tau_x, \qquad g_1 \frac{\partial \sigma_{1y}}{\partial y} = \tau_y, \tag{59}$$

where the shear stress τ_{1xy} in the adherend 1 was neglected.

In the case of the shear stress loading the equilibrium equations for the adherends were taken in the form:

– for the patch

$$g_p \frac{\partial \tau_{xy}^p}{\partial x} = -\tau_x, \qquad g_p \frac{\partial \tau_{xy}^p}{\partial y} = -\tau_x, \tag{60.1}$$

– for the substrate

$$g_s \frac{\partial \tau_{xy}^s}{\partial x} = \tau_x, \qquad g_s \frac{\partial \tau_{xy}^s}{\partial y} = \tau_x, \tag{60.2}$$

with the normal stress in the adherends neglected. The problem was transformed to the second-order equation with the shear stress in the patch τ_{xy}^p:

$$\frac{\partial^2 \tau_{xy}^p}{\partial x^2} + \frac{\partial^2 \tau_{xy}^p}{\partial y^2} + E \tau_{xy}^p + F = 0, \tag{61}$$

where E and F are constants. This equation was solved using the Fourier series expansion.

The analytical models presented in [6–7], which based on the equations of the theory of elasticity were described using incomplete sets of equations, because they include several simplifications, like neglecting of some stress components in the equa-

tions, partial neglecting of the coupling between the unknowns, separation of loading and lack of compatibility conditions for strains.

A complete formulation of the problem in stresses for the adherends presented in this paper is described by the set of six Equations (44.1–2), (63).

In a particular case, if the adhesive is flat and the adherends made of an orthotropic material have a constant thickness, one gets

$$\cos\varphi_x = \cos\varphi_y = 1\,, \quad \frac{\partial g_k}{\partial x} = \frac{\partial g_k}{\partial y} = 0\,, \quad \delta_u = \delta_\upsilon = 1\,, \quad \delta_{u\upsilon} = \delta_{\upsilon u} = 0\,.$$

Then the equations in stresses (44.1–2) can be given in the form:

$$(-1)^k \frac{G_s}{\mathrm{tg}_k}\left(\frac{1}{E_{1x}}\sigma_{1x} - \frac{\nu_{1xy}}{E_{1y}}\sigma_{1y} - \frac{1}{E_{2x}}\sigma_{2x} + \frac{\nu_{2xy}}{E_{2y}}\sigma_{2y}\right) + \frac{\partial^2\sigma_{kx}}{\partial x^2} + \frac{\partial^2\tau_{kxy}}{\partial x\partial y} - \frac{\partial^2\tau_{kxy}}{\partial x^2} - \frac{\partial^2\sigma_{ky}}{\partial x\partial y} + \frac{1}{g_k}\frac{\partial q_{kx}}{\partial x} = 0, \tag{62.1}$$

$$(-1)^k \frac{G_s}{tg_k}\left(\frac{1}{E_{1y}}\sigma_{1y} - \frac{\nu_{1yx}}{E_{1x}}\sigma_{1x} - \frac{1}{E_{2y}}\sigma_{2y} + \frac{\nu_{2yx}}{E_{2x}}\sigma_{2x}\right) + \frac{\partial^2\sigma_{ky}}{\partial y^2} + \frac{\partial^2\tau_{kxy}}{\partial x\partial y} - \frac{\partial^2\tau_{kxy}}{\partial y^2} - \frac{\partial^2\sigma_{kx}}{\partial x\partial y} + \frac{1}{g_k}\frac{\partial q_{ky}}{\partial y} = 0, \tag{62.2}$$

and the equations of strain compatibility (46) read:

$$\frac{1}{E_{kx}}\frac{\partial^2\sigma_{kx}}{\partial y^2} - \frac{\nu_{kxy}}{E_{ky}}\frac{\partial^2\sigma_{ky}}{\partial y^2} + \frac{1}{E_{ky}}\frac{\partial^2\sigma_{ky}}{\partial x^2} - \frac{\nu_{kyx}}{E_{kx}}\frac{\partial^2\sigma_{kx}}{\partial x^2} = \frac{1}{G_{kxy}}\frac{\partial^2\tau_{kxy}}{\partial x\partial y}\,. \tag{63}$$

The boundary conditions for the stresses are given by Equations (34.1–2), where $k = 1, 2$.

After finding the stresses in the adherends the shear stress in the adhesive can be obtained from Equations (43.1–2), which in this case take the form:

$$\tau_x = (-1)^{k+1}\left(\frac{\partial\sigma_{kx}}{\partial x}g_k + \frac{\partial\tau_{kxy}}{\partial y}g_k + q_{kx}\right), \tag{64.1}$$

$$\tau_y = (-1)^{k+1}\left(\frac{\partial\tau_{kxy}}{\partial x}g_k + \frac{\partial\sigma_{ky}}{\partial y}g_k + q_{ky}\right). \tag{64.2}$$

Displacements in the adherends are found from the Equations (42.1–3) after single integration. To find the integration constants kinematic boundary conditions must be formulated.

The solution of the complete two-dimensional problem is difficult, because first six Equations (62.1–2), (63) must be solved and then three Equations (42.1–3) must be integrated. Hence, the formulation in displacements presented in this paper is more efficient and also more general. It requires solution of four Equations (22.1–2).

In the continuation of this paper several examples of solutions will be discussed. Also an analysis of the following problems is planned:

– derivation of the displacement and stress states in the adhesive joints from the equations in displacements for adherends made from orthotropic materials including cases with a varying thickness and a curved surface of the joint,

– determination of stress state in an adhesive from the equations in stresses for adherends of a constant thickness,

– reinforcing and reconstruction of damaged elements made of orthotropic material using adhesive joints including cases with a varying thickness of adherends and a curved surface of adhesive.

References

[1] Adams R.D., Peppiatt N.A.: *Effect of Poisson's ratio strains in adherends on stresses of an idealized lap joint*, Journal of Strain Analysis, Vol. 8, No. 2, 1974, pp. 134–139.

[2] Adams R.D., Wake W.C.: *Structural adhesive joints in engineering*, Elsevier Appl. Sci. Publ. Ltd., 1986.

[3] Ficarra Ch.H.: *Analysis of adhesive bonded fibre-reinforced composite joints*. Dissertation, North Carolina State University, 2001, Adhesion & Adhesives, Vol. 29, 2009, pp. 331–341.

[4] Kim H., Kedward K.: *Stress analysis of in-plane, shear-loaded,* Adhesively Bonded Composite Joints and Assemblies, U.S. Department of Transportation Federal Aviation Administration, Office of Aviation Research Washington, D.C. 20591, Final report DOT/FAA/AR-01/7, 2001.

[5] Kim H., Kedward K.: *Stress analysis of adhesive bonded joints under in-plane shear loading*, Journal of Adhesion, Vol. 76, No. 1, 2001, pp. 1–36.

[6] Mathias J.D., Grédiac M., Balandraud X.: *On the bi-directional stress distribution in rectangular bonded composite patches*, International Journal of Solids and Structures Vol. 43, 2006, pp. 6921–6947.

[7] Mathias J.D., Grédiac M.: *Applying the grid method to validate a numerical model predicting the transverse shear stress distributions in patched structures*, Composites: Part A 39, 2008, pp. 1194–1209.

[8] Silva L.F.M., Neves P.J.C., Adams R.D., Spelt J.K.: *Analytical models of adhesively bonded joints – Part I: Literature survey*, International Journal of Adhesion & Adhesives Vol. 29, 2009, pp. 319–330.

[9] Silva L.F.M., Neves P.J.C., Adams R.D., Wang A., Spelt J.K.: *Analytical models of adhesively bonded joints – Part II: Comparative study*, International Journal of Adhesion & Adhesives, Vol. 29, 2009, pp. 331–341.

[10] Volkersen O.: *Die Nietkraftverteilung von zugbeanspruchten Nietverbindungen mit konstante Laschenquerschnitten*. Luftfahrtforschung, Vol. 15, No. 1–2, 1938, pp. 41–47.

Mechanika połączeń klejowych jako płaskie zadanie teorii sprężystości. Część I: sformułowanie ogólne

Przedmiotem pracy jest sformułowanie ogólnego modelu połączeń klejowych w ramach płaskiej liniowej teorii sprężystości. Elementy połączenia mogą mieć zmienne grubości i mogą być wykonane z różnych materiałów anizotropowych. Powierzchnia spoiny może być zakrzywiona. Kształt elementów w płaszczyźnie połączenia może być dowolny. Połączenia klejowe mogą być obciążone naprężeniami stycznymi dowolnie rozłożonymi na powierzchniach elementów oraz naprężeniami normalnymi i stycznymi dowolnie rozłożonymi na krawędziach elementów.

Przypadek ogólny opisano w przemieszczeniach układem czterech równań różniczkowych cząstkowych rzędu drugiego oraz w naprężeniach układem sześciu równań różniczkowych cząstkowych rzędu drugiego. W przypadku szczególnym sformułowano układ dwóch równań różniczkowych cząstkowych rzędu drugiego dla naprężeń stycznych w spoinie. W warunkach brzegowych uwzględnia się możliwość występowania ostrych krawędzi elementów.

ARCHIVES OF CIVIL AND MECHANICAL ENGINEERING

Vol. X 2010 No. 2

New non-destructive method for linear polarisation resistance corrosion rate measurement

Ł. SADOWSKI
Wrocław University of Technology, Wybrzeże Wyspiańskiego 25, 50-370 Wrocław, Poland.

Corrosion of steel reinforcement is one of the most common causes of end service life in reinforced concrete structures. Corrosion is initiated and propagates unseen beneath the concrete cover and it is difficult to evaluate the severity of the problem. The most promising electrochemical method is the Linear Polarisation Resistance method which can provide a direct evaluation of the instantaneous rate of corrosion. The main drawback to this technique is that it requires a localized breakout of the concrete cover to provide an electrical connection to the steel reinforcement. This article describes an adaptation of the LPR method and the four-point Wenner resistivity method to give an assessment of the rate of steel corrosion without the requirement for a direct connection to the reinforcement. The measurements have been performed in cooperation with Construction and Infrastructure Group in University of Liverpool.

Keywords: *corrosion, concrete, non-destructive testing, resistivity methods*

1. Introduction

In recent years corrosion of steel reinforcement become a leading problem facing the civil engineering industry. Initiation of corrosion usually happens when the passivating alkaline environment provided to the steel bars by the surrounding concrete is neutralized by carbonation or disrupted by chloride ingress. Corrosion then propagates unseen until expansive corrosion products cause cracking or spalling of the concrete cover. Ongoing corrosion in adjacent uncracked regions will quickly cause further cracking to appear, which may be accelerated by the partial remediation [1].

In the last few years much attention has been given for developing portable methods for predicting remaining service life of the concrete structures. It is proper to note that the conventional corrosion assessment examination methods have been the half cell potential method [2] and the concrete resistivity method [3].

The half-cell potential technique requires breakout and an electrical access to the steel reinforcement. This should be connected to a high impedance voltmeter and a reference half-cell, in contact with the surface of the concrete. A number of measurements are taken on a regular grid and contour map of the potentials can be used to identify regions where corrosion activity is likely. Adjacent areas with a large difference in potential are indicative of corrosion activity (Figure 1a).

The concrete resistivity measurement technique was adapted from a method originally used for geophysical surveying [4]. A low magnitude AC current I at the spacing of "a" is passed through the concrete using two surface electrodes. A measurement of the potential V across the third points between the two current electrodes (Figure 1b) gives an evaluation of the electrical resistivity of the concrete in the surface region using the following equation:

$$\rho = 2\pi a \frac{V}{I} \tag{1}$$

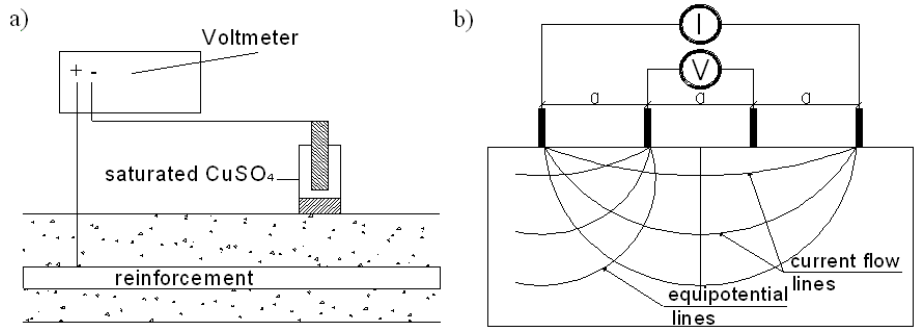

Fig. 1. Existing corrosion methods: a) half cell potential mapping, b) concrete resistivity measurement

From a measurement of low resistivity, it can be inferred that if reinforcement corrosion is ongoing then the rate of corrosion is likely to be relatively high.

Both methods have their disadvantages and work best when used in combination. It is proper to note that these methods give an indication of the probability of corrosion location and corrosion activity and do not give a direct measurement of the instantaneous rate of corrosion.

The most popular of the electrochemical techniques is the Linear Polarisation Resistance (LPR) method [5–7]. The LPR method can be used relatively rapidly and portable instrumentation has been developed [8] suitable for use in the field test. The principal of LPR is based upon disturbing the corrosion equilibrium on the surface of steel reinforcing bars by the introduction of a small perturbative DC electrical signal using a surface counter electrode. The response of the equilibrium to this perturbation is measured with respect to a reference half-cell on the surface of the concrete (Figure 2). In the article a small current step ΔI may be used as the perturbative signal and the resulting potential is ΔE measured and the polarisation resistance R_p is given by:

$$R_p = \frac{\Delta E}{\Delta I}. \tag{2}$$

The corrosion interface comprises a capacitive double layer of charged ions C_{dl} on the surface of the steel bar together with a resistive interface, known as the charge transfer resistance. The electrical circuit can be used to describe the concrete cover and the corrosion interface and the charge transfer resistance is obtained by subtracting the concrete cover resistance often described as the solution resistance R_s from the polarisation resistance (Figure 3). The instantaneous rate of corrosion is proportional to the charge transfer resistance R_{ct}:

$$R_{ct} = R_p - R_s. \tag{3}$$

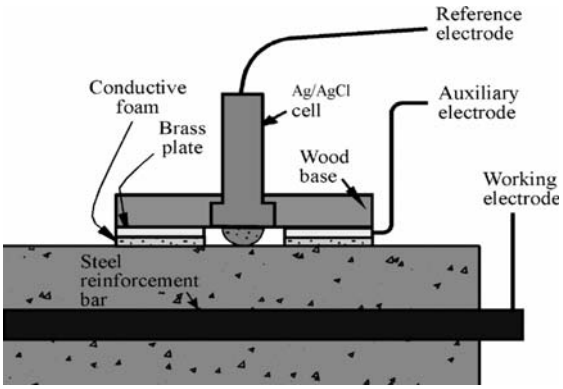

Fig. 2. Linear polarization resistance measurement [2]

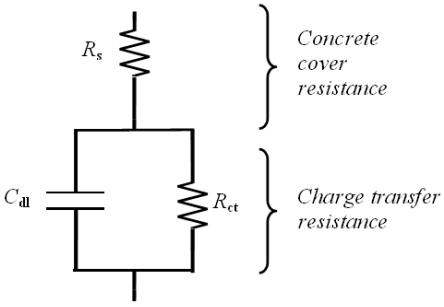

Fig. 3. Randle's equivalent electrical circuit

On the other side the corrosion current density i_{corr} requires knowledge of the area of steel being assessed "*A*" and is given by the Equation (4):

$$i_{corr} = \frac{B}{R_{ct} A}. \tag{4}$$

where a constant *B* is known as the Stern–Geary constant [9]. Typical values of corrosion rates from LPR measurements are presented in Table 1.

Table 1. Typical corrosion rates from LPR measurements [5]

Corrosion classification	Corrosion current density i_{corr}	Corrosion penetration rate
Passive/very low	Up to 0.2 μA/cm^2	Up to 2 μm/year
Low/moderate	0.2 μA/cm^2 to 0.5 μA/cm^2	2 μm/year to 6 μm/year
Moderate/high	0.5μA/cm^2 to 1.0 μA/cm^2	6 μm/year to 12 μm/year
Very High	> 1.0 μA/cm^2	> 12 μm/year

This article describes on a novel adaptation of the resistivity and LPR methods to provide an evaluation of the instantaneous rate of corrosion without the need the con-

nection to the steel reinforcement and without the need to evaluate the area of perturbation.

2. New corrosion rate assessment method

The proposed method takes advantage of the short-circuit effect of a steel bar on the resistivity method rather than avoiding it. Galvanostatic resistivity measurements were taken using a modified electrode array. To ensure the stability of potential during the 30 sec equilibrium period, the two inner standard resistivity probes were replaced with two copper-copper sulphate reference electrodes (Figure 4a). A small current signal was provided by a standard laboratory galvanostat and the resulting change in potential measures using a high impedance voltmeter (Figure 4b).

If a conventional AC four-point resistivity measurement is taken directly over a steel bar and oriented parallel to the bar then this will maximize the reduction effect of the short-circuiting bar on measurement of the apparent resistivity. The AC signal will pass easily through the capacitance C_{dl} regardless of whether the surface of the bar is corroding rapidly (i.e. R_{ct} is small) or if it is corroding slowly always passive (R_{ct} is large).

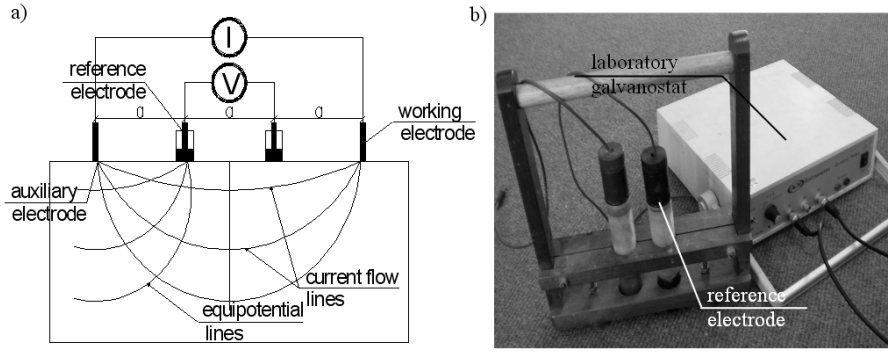

Fig. 4. New corrosion assessment method:
a) scheme of the method, b) view of the equipment

If the same four-point resistivity measurement is again taken at the same location and orientation but using a DC galvanostatic current then the effect of steel bar on the apparent resistivity measurement would be expected to be influenced by the rate of corrosion on the bar surface. Using a DC signal the current can no longer pass through the capacitance C_{dl}, after a suitable equilibrium period.

If R_{ct} is quite small then the apparent resistivity measurement should be close to a similar measurement taken over the bar using an AC signal. However if R_{ct} is large then the apparent resistivity should be close to a measurement taken using an AC signal but when no bar is in the close vicinity.

3. Experimental procedure

For this pilot study three concrete slab specimens size 400 × 300 × 100 mm were available, each containing a single short 30 mm diameter steel bar made form steel class A-III 34GS. Each of these bars had a different concrete cover (10 mm, 20 mm and 30 mm) and different ongoing corrosion rates. The slabs were made from concrete class C 20/25 and from Portland cement CEM I 42,5R and aggregate of maximum size 5 mm. To facilitate the establishment of an electrical connection, each bar was cast with one end protruding from the concrete (Figure 6). The actual rate of corrosion for each specimen was verified by taking a LPR measurement within a short time of the resistivity measurements. The surface counter electrode was sufficiently large that it was assumed that the entire surface area of the short bar was effectively polarized by the perturbing current step.

Fig. 5. Concrete resistivity measurement system (CNS Equipment)

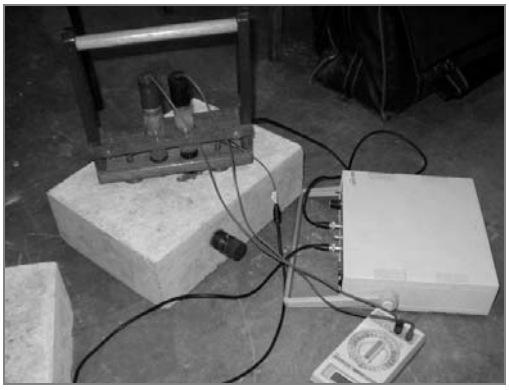

Fig. 6. The view of laboratory stand

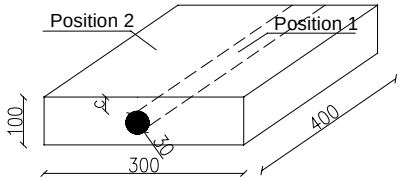

Fig. 7. Resistivity measurement locations on concrete specimen

Measurements were taken of the AC resistivity (Figure 5) both directly over and remote from the steel bar at Position 1 and Position 2 (Figure 7). The Position 2 should be located not closer from the edges than the slab thickness. In this test it was exactly 100 mm. These measurements establish the extent of maximum influence of the bar on the actual concrete resistivity. The galvanostatic DC resistivity measurement was then taken at Position 1. In this test the suitable equilibrium period was 30 second which is not inde-

pendent from the size and material of the specimen. It is proper to note that the DC resistivity measurement must be taken exactly over the reinforcement.

4. Results

From the traditional Linear Polarization Resistance corrosion techniques it was established that two of the bars were corroding actively with corrosion current densities of 8.47 μA/cm^2 and 7.28 μA/cm^2. From this it was expected that the surface of the steel bar would have a relatively small charge transfer resistance R_{ct} and that a DC measurement of resistivity over the bar should give an apparent resistivity much closer to the resistivity from an AC resistivity measurement over the bar than that of the actual concrete resistivity. Figure 8 shows that for both specimens over a small range of ambient temperatures, ρ_{DC} is much closer to $\rho_{AC,bar}$ than to $\rho_{AC,\mathrm{conc}}$.

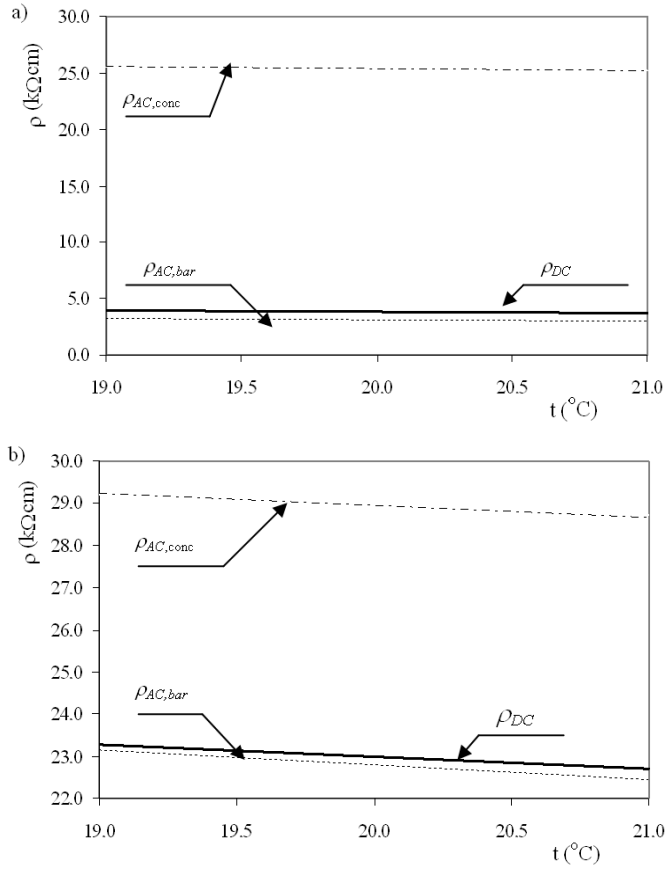

Fig. 8. Concrete resistivity measurements on specimens with actively corroding bars: a) 10 mm cover, i_{corr} = 8.47 μA/cm^2, b) 30 mm cover, i_{corr} = 7.28 μA/cm^2

Only one reinforcing bar exhibited a much lower corrosion current density of i_{corr} = 0.46 μA/cm^2 which was close to passivity. For this bar with a cover of 20 mm a much larger charge transfer resistance R_{ct} on the surface of the steel bar is expected and the presence of the bar should have small effect on a DC resistivity measurement (Figure 9). Over the range of ambient temperatures investigated, ρ_{DC} is much closer to $\rho_{AC,conc}$ then to $\rho_{AC,bar}$.

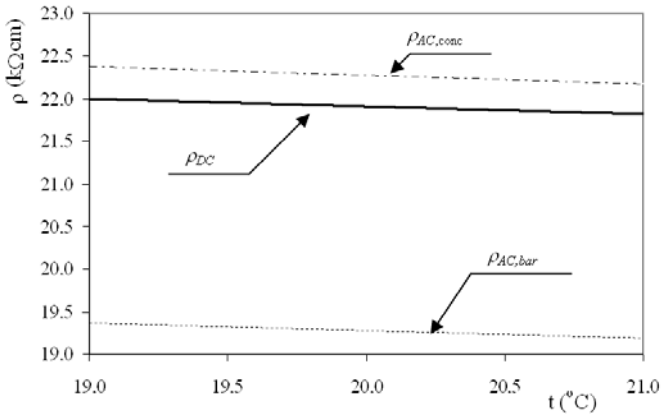

Fig. 9. Concrete resistivity measurements on specimen with passive bar, 20 mm cover, i_{corr} = 0.46 μA/cm^2

5. Conclusions

This study has shown that the short-circuit influence of an embedded steel bar in the vicinity of a concrete resistivity measurement can be used to evaluate the rate of ongoing corrosion on the surface of the bar. The measurements and analyses clearly shows that new method using a novel DC resistivity approach in conjunction with conventional AC resistivity measurements offers a means of assessing directly the instantaneous rate of corrosion using a procedure which is relatively quick and which does not require breakout of the concrete cover.

Further measurements are required to terminate the combined method limitations. Especially to validate the method with a range of different bar sizes and a wider range of covers. In addition concrete with a wider range of resistivity should be investigated.

References

[1] Pullar-Strecker P.: *Concrete reinforcement corrosion: From assessment to repair decisions*, Thomas Telford, 2002.

[2] *Standard test method for half-cell potentials of uncoated reinforcing steel in concrete*, C876-91, ASTM: Philadelphia, 1991.

[3] Broomfield J., Millard S.: *Measurement of concrete resistivity to assess corrosion rates*, Concrete, 2002, pp. 37–39.
[4] Wenner F.: *A method of measuring earth resistivity*, Bulletin of the Bureau of Standards, Vol. 12, 1912, pp. 469–478.
[5] Andrade C., Alonso C.: *Corrosion rate monitoring in the laboratory and on site*, Construction and Building Materials, Vol. 10, No. 5, 1996, pp. 315–328.
[6] Millard S.: *Measuring the corrosion rate of reinforced concrete using linear polarisation resistance*, Concrete, 2003, pp. 36–38.
[7] Gowers K., Millard S.: *Electrochemical techniques for corrosion assessment of reinforced concrete structures*, Proc. Institution Civil Engineers: Structures. & Buildings, Vol. 134, 1999, pp. 129–137.
[8] Law D., Millard S., Bungey J.: *Linear polarisation resistance measurements using a potentiostatically controlled guard ring*, NDT&E International, Vol. 1, 2000, pp. 15–21.
[9] Stern M., Geary A.: *Electrochemical Polarization – Theoretical analysis of the shape of polarization curves*, J. Electrochemical Society, Vol. 104, 1957, pp. 56–63.
[10] Sadowski Ł.: *Measurement of concrete resistivity for the assessment of corrosion risk*, I International Interdisciplinary Technical Conference of Young Scientists, Poznan, 2008.
[11] Sadowski Ł., Millard S.: *Non-destructive assessment of the corrosion risk to reinforcing steel using a measurement of the resistance of concrete* (in Polish), Przegląd Budowlany, Vol. 5, 2008, pp. 35–39.

Nowa nieniszcząca metoda pomiaru stopnia korozji z użyciem polaryzacji liniowej

Korozja stali zbrojeniowej w betonie jest jedną z głównych przyczyn degradacji konstrukcji żelbetowych. Korozja jest inicjowana i propagowana przez otulinę zbrojenia i wobec tego jest niezmiernie trudno ocenić znaczenie tego problemu. Najbardziej obiecującą elektrochemiczną metodą jest metoda polaryzacji liniowej, za pomocą której można w sposób bezpośredni wyznaczyć stopień korozji. Główną wadą metody jest konieczność odkucia betonowej otuliny w celu zapewnienia elektrycznego dostępu elektrody do zbrojenia. Artykuł opisuje adaptację metody polaryzacji liniowej wraz z metodą Wennera pomiaru oporności betonu do oceny stopnia korozji stali zbrojeniowej w betonie bez konieczności bezpośredniego kontaktu ze zbrojeniem. Badania zostały przeprowadzone przy współpracy z Construction and Infrastructure Group z University of Liverpool.

ARCHIVES OF CIVIL AND MECHANICAL ENGINEERING

Vol. X 2010 No. 2

Experimental study on ultimate strength of CK20 steel cylindrical panels subjected to compressive axial load

M. SHARIATI, M. SEDIGHI, J. SAEMI, H.R. EIPAKCHI, H.R. ALLAHBAKHSH
Mechanical Engineering Faculty, Shahrood University of Technology, Shahrood, P.O. Box 316, I.R., Iran.

In this paper, the effects of the length, sector angle and boundary conditions on the buckling load and post-buckling behaviour of cylindrical panels have been studied, experimentally. The compressive axial load has been applied on the panels using servo-hydraulic machine and different boundary conditions have been prepared by suitable fixtures. The presented results can be used in designing of these structures.

Keywords: *buckling, post-buckling, cylindrical panels, experimental test*

1. Introduction

The shell structures are important in various engineering fields. The buckling load, is usually the most criterion in designing of a long thin shell. The classification and design codes for aircraft, space vehicles, ships, offshore platforms, trains and cold formed sections are all based mostly on experimental findings and semi empirical formulas. Based on the classic theories, the buckling load of thin cylindrical shells subject to uniform axial compression can be predicted using the formula:

$$N_{cr} = \frac{E}{\sqrt{3(1-\nu^2)}}\left(\frac{t^2}{R}\right). \tag{1}$$

where:

E is the Young's modulus,

ν is Poisson's ratio,

t is shell thickness,

R is shell radius.

It is noteworthy that this formula gives an appropriate result for thin shells without cutouts with $L/R \leq 5$ [1]. For shells with moderate thickness ($R/t < 50$), this formula often overestimates the buckling load, so that buckling occurs before reaching the specified load. An analytical solution for the buckling load of isotropic and orthotropic panels has been presented by Timoshenko [2] and Lekhnitskii [3]. Magnucki [4] solved the Donnell's equation for buckling of panels with three edges simply supported and one

edge free subjected to axial load using the Galerkin method. Patel [5] discussed on static and dynamic stability of panels with the edge harmonic loading. Jiang [6] studied the buckling of panels subjected to compressive stress using the differential quadrature element method. The most experimental works, relates to the buckling of columns and cylinders. Young [7] presented an experimental investigation of concrete-filled cold-formed high strength stainless steel tube columns subjected to uniform axial compression. He studied the effects of the tube shape, plate thickness and concrete strength. The test results were compared with American and Australian standards. Zhu [8–9] studied experimentally the failure modes and strengths of aluminium alloy with and without transverse weld subjected to pure axial compression between fixed ends. The observed failure modes include yielding and buckling for different lengths. The test results were compared with some standards for aluminium structures. Liu [10] described a test procedure on cold-formed stainless steel square hollow sections subjected to pure axial compression. He concluded that design rules in Australian standard are slightly more reliable than the design rules in the American and European specifications for performed tests. Zhang [11] presented experimental and numerical investigations on the performance of repaired thin-skinned, blade-stiffened composite panels in the post-buckling range. The results showed that under the present repair scheme, the strength of the panel can be recovered satisfactorily. Further, the repair scheme was seen capable of restoring the general load path in the panels as well as the general post-buckling behaviour. Lanzi [12] reported the results of an experimental investigation on stringer-stiffened panels made of carbon fabric reinforced plastic. The axial compression tests were performed up to collapse. Experimental data demonstrated the strength capabilities of the identified structures to operate in post buckling, allowing further weight savings.

In this paper, the effects of the length, sector angle and different boundary conditions on instability of steel cylindrical panels have been studied experimentally. Also, the behaviour of the panels in post-buckling path has been shown.

2. Theoretical analysis: buckling of circular cylindrical panels under axial compression

Consider a simply supported, cylindrical panel of length L, radius R, thickness t and central angle φ. The panel is under a uniform axial compressive force N as shown in Figure 1.

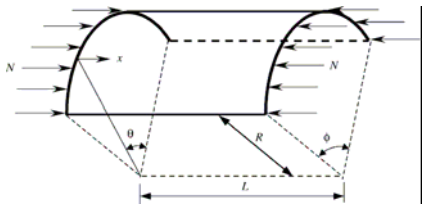

Fig. 1. Cylindrical panel under compression

For the buckling of cylindrical shells, the governing differential equations are given by

$$\frac{\partial^2 u}{\partial x^2}+\frac{1+\nu}{2R}\frac{\partial^2 v}{\partial x\partial\theta}-\frac{\nu}{R}\frac{\partial w}{\partial x}+\frac{1-\nu}{2R^2}\frac{\partial^2 u}{\partial\theta^2}=0, \tag{2}$$

$$\begin{aligned}&\frac{1+\nu}{2R}\frac{\partial^2 u}{\partial x\partial\theta}+\frac{1-\nu}{2}\frac{\partial^2 v}{\partial x^2}+\frac{1}{R^2}\frac{\partial^2 v}{\partial\theta^2}-\frac{1}{R^2}\frac{\partial w}{\partial\theta}-\frac{N(1-\nu^2)}{Et}\frac{\partial^2 v}{\partial x^2}\\&\quad+\frac{t^2}{12R^2}\left[\frac{1}{R^2}\frac{\partial^2 v}{\partial\theta^2}+\frac{1}{R^3}\frac{\partial^3 w}{\partial\theta^3}+\frac{\partial^3 w}{\partial x^2\partial\theta}+(1-\nu)\frac{\partial^2 v}{\partial x^2}\right]=0,\end{aligned} \tag{3}$$

$$\begin{aligned}&\nu\frac{\partial u}{\partial x}+\frac{1}{R}\frac{\partial v}{\partial\theta}-\frac{w}{R}-\frac{t^2}{12R^2}\\&\left[\frac{1}{R}\frac{\partial^3 v}{\partial\theta^3}+(2-\nu)R\frac{\partial^3 w}{\partial x^2\partial\theta}+R^3\frac{\partial^4 w}{\partial x^4}+\frac{1}{R}\frac{\partial^4 w}{\partial\theta^4}+2R\frac{\partial^4 w}{\partial x^2\partial\theta^2}\right]-\frac{NR(1-\nu^2)}{Et}\frac{\partial^2 w}{\partial x^2}=0,\end{aligned} \tag{4}$$

in which u, v, w are the longitudinal displacement, tangential displacement and radial displacement, respectively. The displacement functions are, however, given by

$$u=\sum_m^\infty\sum_n^\infty A_{mn}\sin\frac{n\pi\theta}{\phi}\cos\frac{m\pi x}{L}, \tag{5}$$

$$v=\sum_m^\infty\sum_n^\infty B_{mn}\cos\frac{n\pi\theta}{\phi}\sin\frac{m\pi x}{L}, \tag{6}$$

$$w=\sum_m^\infty\sum_n^\infty C_{mn}\sin\frac{n\pi\theta}{\phi}\sin\frac{m\pi x}{L}. \tag{7}$$

where:

A_{mn}, B_{mn}, C_{mn} are the unknown buckling amplitudes. By substituting Equations (5) to (7) into Equations (2) to (4), we obtain

$$N=\frac{Et}{(1-\nu^2)}\left[\frac{t^2}{12R^2}\frac{\left(\frac{n^2\pi^2}{\phi^2}+\beta^2\right)^2}{\beta^2}+\frac{(1-\nu^2)\beta^2}{\left(\frac{n^2\pi^2}{\phi^2}+\beta^2\right)^2}\right]. \tag{8}$$

Denoting $\beta = \dfrac{m\pi R}{L}$. Therefore, the buckling load for a cylindrical panel under uniform axial compression is given by

$$N_{\min} = \frac{1}{\sqrt{3(1-\nu^2)}}\left(\frac{Et^2}{R}\right). \tag{9}$$

When the angle φ is very small, the buckling behaviour of the cylindrical panel approaches that of a longitudinally compressed rectangular plate.

3. Experimental study

Some specimens with different lengths and sector angles have been prepared. All the specimens have been manufactured from one tube branch and so, they have the same radius and thickness. Figure 2 shows schematic of a panel and the dimensions have been listed in Table 1. The bucking tests were performed using a servo-hydraulic machine (INSTRON 8802). This universal test machine includes a hydraulic actuator for applying axial load on panels and two load cells with capacities 25 kN and 250 kN for different applications. The test results can be transmitted to a computer.

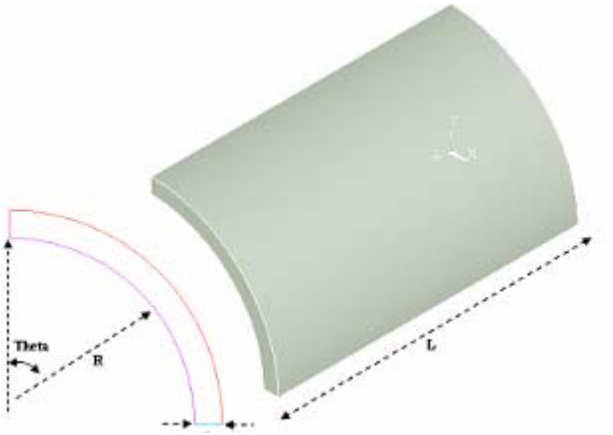

Fig. 2. Schematic of panels

Table 1. Geometrical and mechanical properties of panels

D = 42 mm	Diameter
t = 2 mm	Thickness
Θ = 90°, 120°, 180°, 355°, Complete	Sector angle
L = 100, 150, 250 mm	Length
σ_y = 340 MPa	Yield stress
E = 192 GPa	Elasticity modulus

3.1. Mechanical properties

The mechanical properties of the metal panels have obtained using the tensile test. The dimensions of tensile test specimens which are cut from the original tube, have been chosen according to

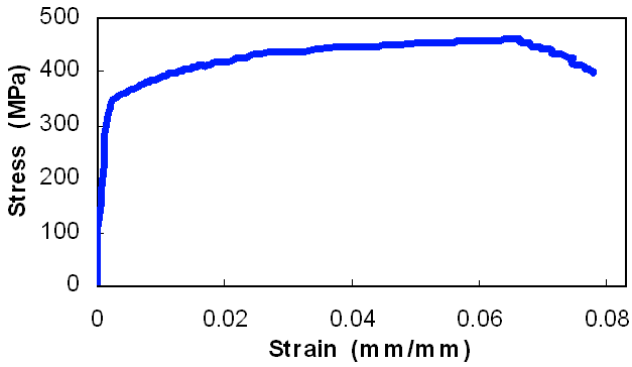

Fig. 3. Stress-strain diagram

ASTM E8 standard [13]. Figure 3 shows the stress-strain diagram for this material. The Young's modulus and the yield stress which are listed in Table 1 have been determined from Figure 3.

3.2. Boundary conditions

Two types of fixtures were designed to simulate the simply supported and clamped boundary conditions for the arc ends. Figure (4a) shows a fixture for simply supported conditions. It does not have any resistance to rotation. A fixture for clamped boundary conditions has been shown in Figure (4b). It has a narrow width and a deep slot, so the zero slope condition at the end, is reasonable.

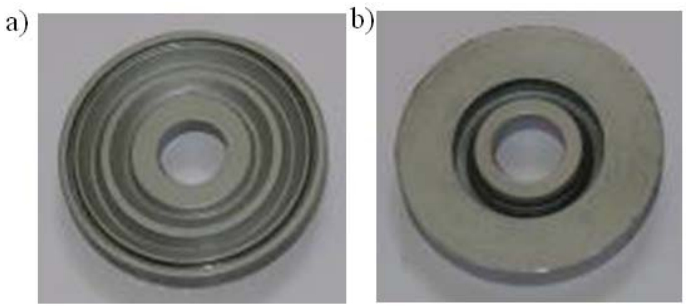

Fig. 4. a) Simply supported fixture, b) Clamped supported fixture

4. Buckling test

For the buckling test, an axial load was applied on the panels and by measuring the axial displacement, the load-displacement diagram was determined. These tests were performed for different panels with clamped and simply supported boundary condition. In all tests (except for a complete cylinder), the straight edges are free and the simple or clamped supports were applied on arc edges of panels. Figure 5 shows the test setup.

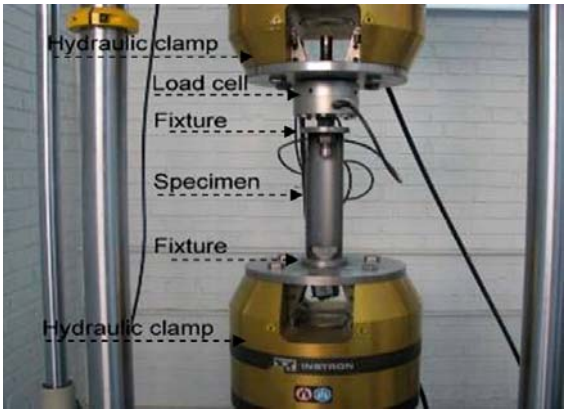

Fig. 5. Experimental test setup

4.1. Length effect

For investigation of the length effect, the buckling test was performed on some panels with the same angle and different lengths. The load-displacement for each panel was drawn. The peak values stand for the ultimate strength. For example, Figure 6 is the load – displacement diagrams for different lengths with $\theta = 90°$.

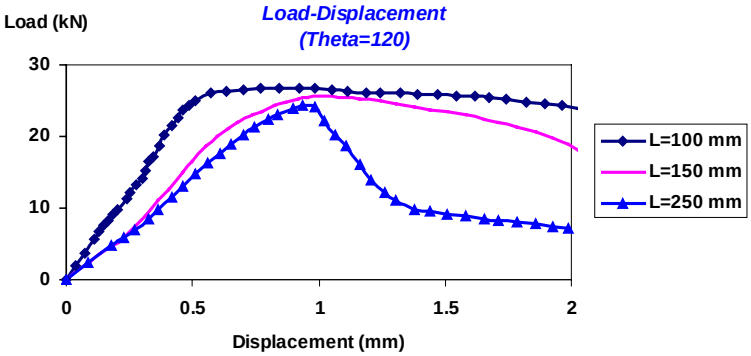

Fig. 6. Load-displacement diagram ($\theta = 120°$, simple supports)

Figure 7 shows the variation of the buckling load in terms of the length for different sector angles. The "Perfect" in Figure 7 stands for a cylinder (θ = 360°). Deformations of tested panels have been shown in Figure 8. The experimental tests show that by decreasing the panel length, the buckling load will increase slightly.

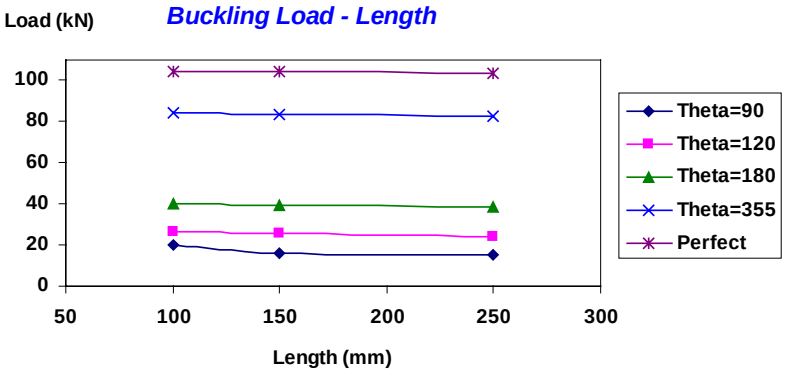

Fig. 7. Buckling load in terms of the length (for different sector angles)

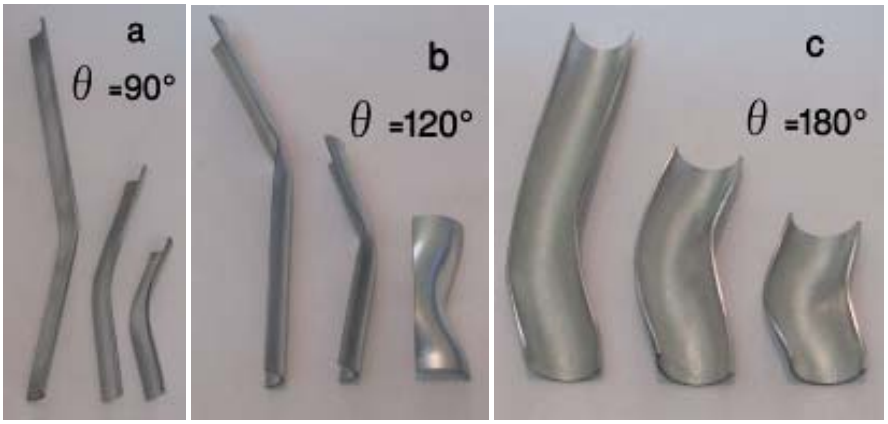

Fig. 8. Buckling mode shapes of panels with the same sector angles and different lengths (L = 100, 150, 250 mm), a) θ = 90°, b) θ = 120°, c) θ = 180°

4.2. Sector angle effect

Some experimental tests were performed on panels with L = 100 mm and θ = 90°, 120°, 180°, 355°, 360°. In Figure 9, the load-displacement diagrams for panels with different sector angle have been shown. θ = 355° corresponds to a narrow cutting on the original tube as Figure 10. Figure 11 shows the variations of the buckling load in terms of θ for different lengths and Figure 12 shows the buckling stress which it has been defined easily as the ratio of the load to cross section.

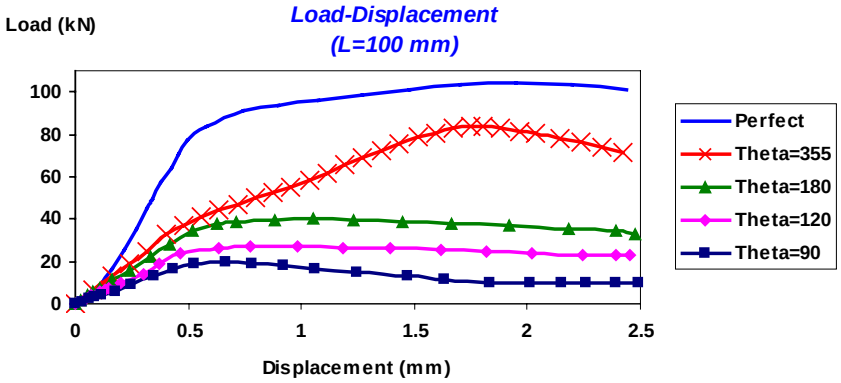

Fig. 9. Load-displacement diagram (L = 100 mm, simple supports)

Fig. 10. Panel deformation (L = 100 mm, θ = 355°)

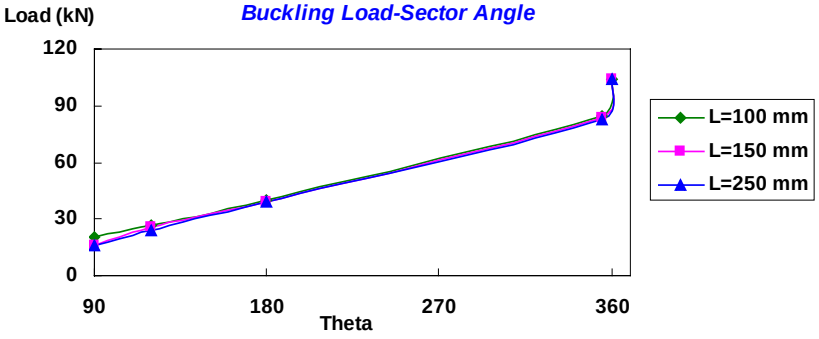

Fig. 11. Variations of buckling load in terms of sector angle for different lengths (simple supports)

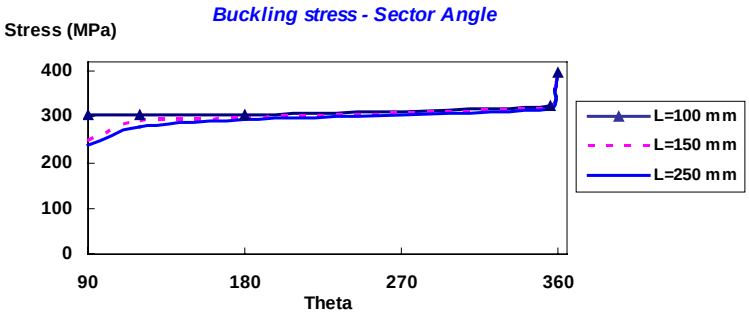

Fig. 12. Variations of buckling stress in terms of sector angle for different lengths (simple supports)

4.3. Boundary conditions effect

By changing the boundary conditions from simple to clamped, the degrees of freedom of supports reduce and the buckling load will increase. Figures 13–15 show the load-displacement diagrams for panels (θ = 90°) with different boundary conditions and the buckling loads have been listed in Table 2.

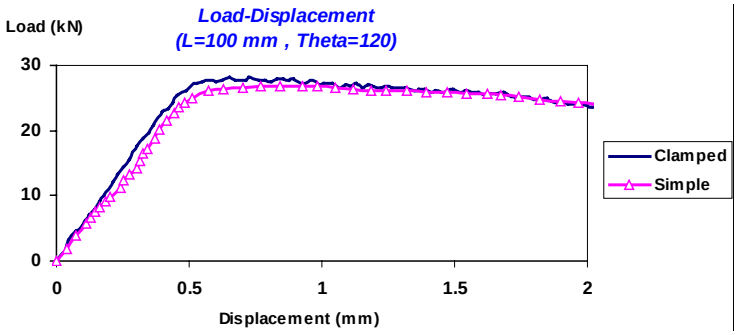

Fig. 13. Load-displacement diagram for clamped and simple supports (L = 100 mm, θ = 120°)

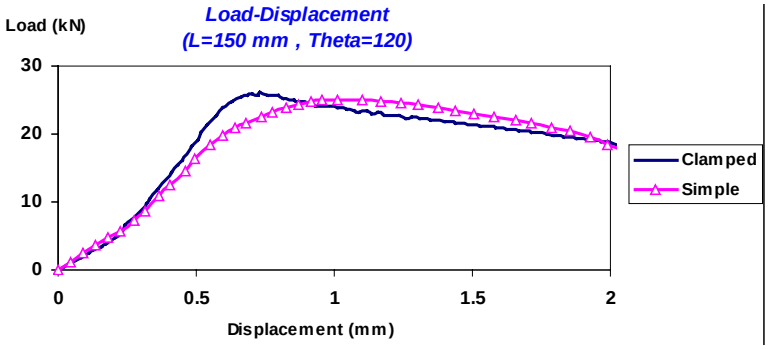

Fig. 14. Load-displacement diagram for clamped and simple supports (L = 150 mm, θ = 120°)

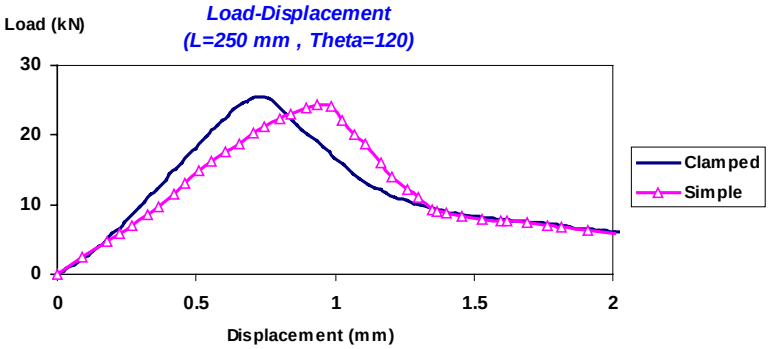

Fig. 15. Load-displacement diagram for clamped and simple supports (L = 250 mm, θ = 120°)

Table 2. Buckling loads (kN) for panels with clamped and simple supports

	θ = 90°		θ = 120°		θ = 180°		θ = 355°		θ = 360°	
	Simple	Clamped	Simple	Clamped	Simple	Clamped	Simple	Clamped	Simple	Clamped
L = 100 (mm)	19.85	20.05	26.75	28.18	39.50	39.86	84.09	85.62	106.91	–
L = 150 (mm)	15.98	16.37	25.11	26.04	38.81	39.21	83.39	85.27	105.26	–
L = 250 (mm)	14.95	15.64	24.33	25.58	38.05	38.87	82.89	84.13	103.73	104.48

4.4. Effect of eccentric loading

In this section, the effect of eccentric loading on the buckling behaviour of cylindrical panel under combined loading is studied by emphasizing on panel with similar length and three sector angle of 90°, 120° and 180°.The results indicate that buckling load is more sensitivity to eccentric load and only the eccentricity (X = 51 mm) for specimens (L = 100 mm), will cause the shell to buckle at 0.02 of axial compression load. Types of fixture were designed to simulate the combined loading and sensitivity of the cylindrical panel buckling to eccentricity is shown in Figure 16.

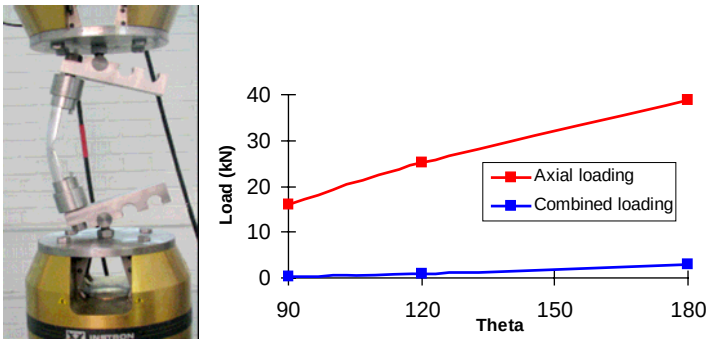

Fig. 16. Schematic of fixtures applying for combined loading and diagram of sensitivity of the panel buckling load to eccentricity

5. Confirmation of theoretical results with experimental findings

A curved plate loaded in axial compression buckle in the same manner as a cylinder when the plate curvature is large, and when the plate curvature is small it buckles essentially as a flat plate. Between these two limits there is a transition from one type of behaviour to the other. When load is applied to the plate it attains a critical load, after which the load suddenly drops. Upon further axial deformation the load continues to rise again and reaches a failure load which is greater than the buckling load if the latter occurs elastically. When the plate buckles plastically, buckling and failure are coincident.

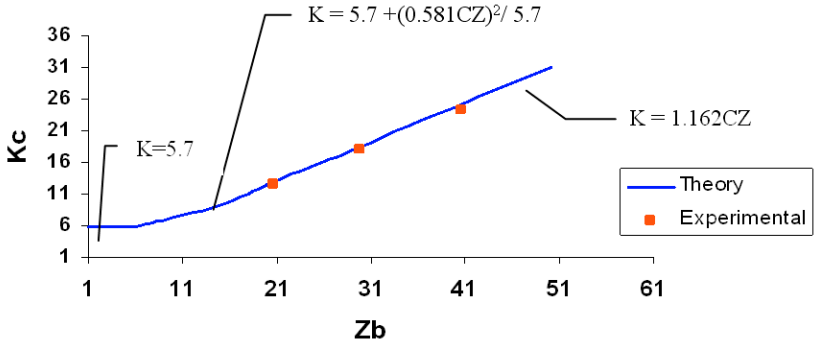

Fig. 17. Comparison of test data for (L = 150 mm, θ = 90°, 120°, 180°) with theory for axially compressed panels

Some of test data, for L = 150 mm in three different sector angle (θ = 90°, 120°, 180°), are shown in Figure 17 in terms of K_c and Z_b, where

$$Z_b = \left(1-v^2\right)^{0.5}\left(\frac{b^2}{rt}\right), \tag{10}$$

$$K_C = \frac{12\sigma_{cr}\left(1-v^2\right)}{\pi^2 E}\left(\frac{b}{t}\right)^2. \tag{11}$$

where:

E is the Young's modulus,
v is Poisson's ratio,
σ_{cr} is critical stress,
t is shell thickness,
r is shell radius,
b is width of cylindrical panel.

The boundary conditions of the panels tested were between simple supports and clamped. Thus an average of the buckling coefficients of these two limiting cases, K_{pl} = 5.7, was used for correlation purposes [14]. The theoretical results are in good agreement with the experimental tests.

6. Results

By increasing the length, the buckling load decreases slightly (Figure 7). This reduction is more for shorter lengths. Also by increasing the sector angle of a panel, the buckling load increases. It is possible to approximate the buckling load as

$$P = K\frac{\theta^n}{L^m}, \tag{12}$$

where k, m, n are constants and they depend on the geometrical and mechanical properties of panels.

In Figure 8, the deformed shape of the tested panels has been shown. For a short panel, it is snap-through like. For a long panel, it deforms like the Euler column and for a cylinder, it has a symmetric deformation. This symmetry can be approved the uniformity of the applied load. According to Figure 9, the existence of a narrow cutting (θ = 355°) can reduce the buckling load significantly. It may be due to reduction of the structure stiffness. Also the buckling load capacity of a complete cylinder is more than of this panel. Figure 10 shows the deformed shape of panel for this case. From Figures 11–12 the variations of the buckling load with respect to the sector angle is nearly linear expect for a cylinder. The yielding occurs before buckling in cylinder with L = 100 mm, so its results did not report in Figures 11–12. The buckling stress is constant approximately for θ > 90° or the buckling stress is not sensitive to the sector angle for tested specimens. For clamped boundary conditions, the buckling load is more than the simple support (Figures 13–15 Table 2). According to Figures 13–15 there is a delay of the buckling load by using simply supported boundary condition because the support permits the rotation in addition of axial displacement but in the clamped boundary conditions, there is no rotation or the structure is more restricted than the later case. In the other word, clamping the boundaries will increase the stiffness of the structure. The behaviour of the panel in post-buckling path may not be predicted or by changing the length (Figure 6), sector angle (Figure 9) and boundary conditions (Figures 13, 14); the behaviour of the panel will change. The results indicate that buckling load is more sensitivity to eccentric load (Figure 16). Figure 17 shows the theoretical results are in good agreement with the experimental tests. To check the repeatability of test, three tests have been performed for a panel with L = 150 mm, θ = 120°. The load-displacement diagrams have been shown in Figure 18 There is a good agreement between the results.

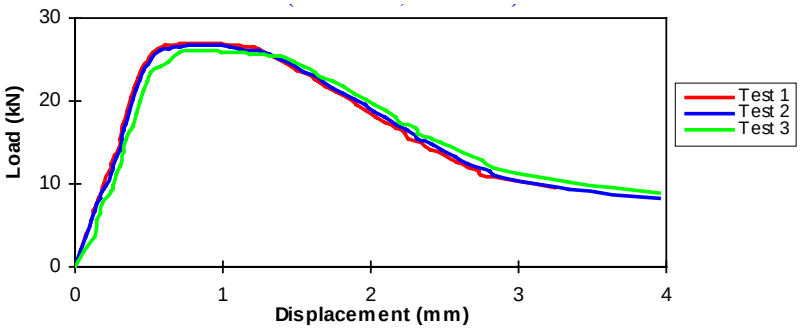

Fig. 18. Load-displacement diagram – test repeatability (L = 150 mm, θ = 120°)

7. Conclusions

The experimental tests show that:

1. By increasing the length of the panels, the bucking load decreases slightly. It is more important for short panels.
2. For $\theta > 90°$, by increasing the sector angle, the buckling load increases. Approximately, for tested panels, the buckling stress is not sensitive to the sector angle.
3. Clamped boundary conditions can increase the bucking load but the post-buckling path does not change significantly.
4. There is a delay of the buckling load by using simply supported boundary condition because, the simply support permits the rotation in addition of axial displacement but in the clamped boundary conditions structure is more restricted than the later case.
5. The existence of a longitudinal narrow slot will decrease the buckling load noticeably.
6. The results indicate that buckling load is more sensitivity to eccentric load.
7. The theoretical results are in good agreement with the experimental tests.

References

[1] Ugural A.C.: *Stresses in plates and shells*, New York, McGraw-Hill, 1981.
[2] Timoshenko S.P., Gere J.M.: *Theory of elastic stability*, New York, McGraw-Hill, 1961.
[3] Lekhnitskii S.G.: *Anisotropic plates*, Gordon and Breach, New York, 1968.
[4] Magnucki K., Mackiewicz M.: *Elastic buckling of an axially compressed cylindrical panel with three edges simply supported and one edge free*, Thin-Walled Structures, 2006, Vol. 44, No. 4, pp. 387–392.
[5] Patel S.N., Datta P.K., Sheikh A.H.: *Buckling and dynamic instability analysis of stiffened shell panels*, Thin-Walled Structures, 2006, Vol. 44, No. 3, pp. 321–333.
[6] Jiang L., Wang Y., Wang X.: *Buckling analysis of stiffened circular cylindrical panels using differential quadrature element method*, Thin-Walled Structures, 2008, Vol. 46, No. 3, pp. 390–398.

[7] Young B.: *Experimental and numerical investigation of high strength stainless steel structures*, Journal of Constructional Steel Research, 2008, Vol. 64, No. 11, pp. 1225–1230.
[8] Zhu J., Young B.: *Numerical investigation and design of aluminium alloy circular hollow section columns*, Thin-Walled Structures, 2008, Vol. 46, No. 12, pp. 1437–1449.
[9] Zhu J.H., Young B.: *Experimental investigation of aluminium alloy circular hollow section columns*, Engineering Structures, 2006, Vol. 28, No. 5, pp. 207–215.
[10] Liu Y., Young B.: *Buckling of stainless steel square hollow section compression members*, Journal of Constructional Steel Research, 2003, Vol. 59, No. 2, pp. 165–177.
[11] Zhang H., Motipalli J., Lam Y.C., Baker A.: *Experimental and finite element analyses on the post-buckling behaviour of repaired composite panels. Composites Part A*, 1998, Vol. 29, No. 11, pp. 1463–1471.
[12] Lanzi L.: *An experimental investigation on the post-buckling behaviour of composite stiffened panels*, 45th AIAA/ASME/ASCE/AHS/ASC Structures, Structural Dynamics & Materials Conference, California, 2004.
[13] ASTM A370-05, *Standard test methods and definitions for mechanical testing of steel products*.
[14] Gerard, George and Becker, Herbert: *Handbook of structural stability. Part 3: buckling of curved plates and shells*, NACA TN 3783, 1957.

Eksperymentalne badania wytrzymałości elementów cylindrycznych wykonanych ze stali CK20 poddanych osiowemu ściskaniu

W pracy przedstawiono eksperymentalne wyniki wpływu długości i kąta sektora próbek oraz warunków brzegowych na siłę wyboczenia oraz ich zachowanie się po wyboczeniu. Badania przeprowadzono na maszynie hydraulicznej, gdzie za pomocą odpowiednich uchwytów uzyskano różne warunki brzegowe. Przedstawione wyniki mogą być wykorzystane w projektowaniu struktur cylindrycznych.

ARCHIVES OF CIVIL AND MECHANICAL ENGINEERING

Vol. X 2010 No. 2

Degradation of a geared bearing of a stacker

T. SMOLNICKI, P. HARNATKIEWICZ, M. STAŃCO
Wrocław University of Technology, Wybrzeże Wyspiańskiego 25, 50-370 Wrocław, Poland.

Large size rolling-element bearings used for turning of upper body of machines used in open-pit mining are made in form of single-row or double-row ball bearings. Section diameter of those bearings may be as large as 20 m and rolling elements have diameters of 100 to 250 mm, while they are under eccentric axial load from few to tens of MN. Due to low stiffness of supportive elements and its non-uniform presence all over the circumference of the bearing, the load upon rolling elements is rather unequal in those bearings. The flow of load stream concentrates in points which are in the areas with highest stiffness. This may be achieved using modern computer-assisted design tools. The specificity of these custom made machines makes obtaining credible data for numeric models possible only by applying analyses of the already existing bearings and their support structures which had been in operation for many years. Was introduced applied to opinion of effect of long-lasting exploitation on change of parameters of bearing.

Keywords: *degradation of a geared bearing, durability turn bearing, measurement methods*

1. Introduction

Maintaining desired durability of the main turn bearing in basic open-cast mining machinery is a difficult issue. Beside choosing bearing parameters, it is also required to shape the stiffness of the supporting structures to ensure even distribution of forces over the rolling elements of the bearing [1–2]. This may be achieved using modern computer-assisted design tools [3–4]. The specificity of these custom made machines makes obtaining credible data for numeric models possible only by applying analyses of the already existing bearings and their support structures which had been in operation for many years [5–6, 9]. Below, using the example of a stacker bearing, we have shown the methods used to assess the impact that long-term operation had on bearing parameters.

2. Object inspected

The object subjected to inspection is a stacker bearing (Figure 1) after many years in operation. It is a single-row thrust bearing with monolithic "soft" races. The basic geometric parameters of this bearing are (Figure 2):

– pitch diameter of the bearing D, 10 m,
– ball diameter d_k, 120 mm,

– number of balls z, 232,
– nominal race radius r_B/ congruence coefficient w, 63 mm/0.952,
– body mass M, 640 Mg.

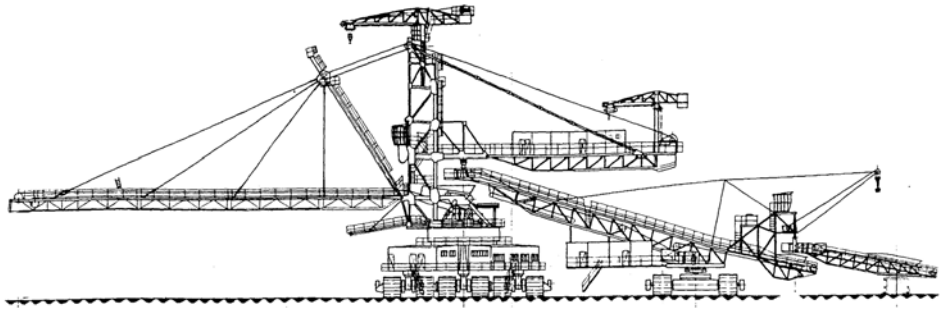

Fig. 1. An A2RsB 5000 stacker

The geometry of this bearing is not much different from typical main turn bearings of basic machinery [1, 5, 9] but unlike most of them, it does not have cages which maintain an even pitch of the rolling elements and preventing friction between them. The toothed ring is screwed down to the lower race.

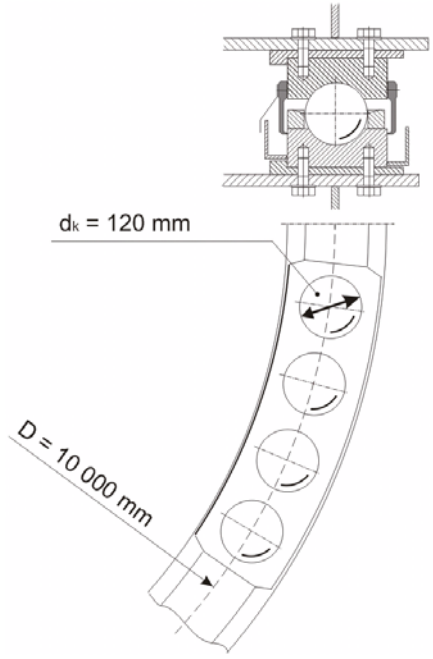

Fig. 2. The bearing of A2RsB 5000 stacker

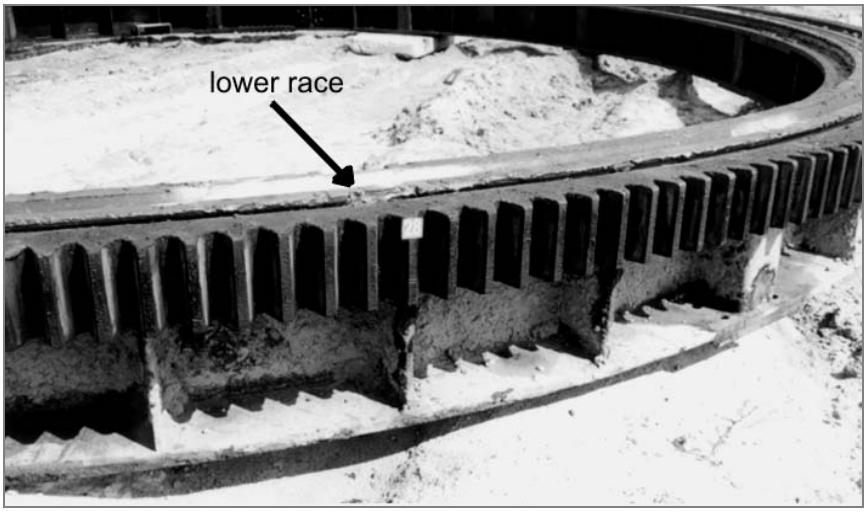

Fig. 3. Annular girder of the lower race after disassembly

The running gear of the stacker on an equilateral triangle plane consists of three main girders joined by three walls, which gives a regular hexagonal support structure. The direct frame for the bearing is a low annular girder (Figure 3) supported on the load carrying structure of the running gear in 12 points.

3. Measurement methods and results

The most common bearing degradation assessment method is inspection, which allows to make an initial assessment of the state of cooperating surfaces. An inspection can only show the presence of pitting, larger cracks, which have already surfaced, determine the size and depth of lost material, and in the case of "soft" bearings the degree of race rolling. To diagnose the state of the bearing in more detail, more advanced experimental examination methods must be used [8, 10].

In the bearing in question (Figures 3 and 4), the race was found to be in a good condition, minor material losses were observed, a lace of minor cracks had formed, the race was slightly rolled (the material did not "flow out" over the upper edge of the race) or moderately rolled (a slight outflow). A sample for microstructure assessment from a cross-section of the bearing was presented in Figure 5. This figure shows the material structure and form of the material outflows.

The chemical composition of the race material has been identified: C – 0.510%, Mn – 0.67%, Si – 0.35%, P – 0.005%, S – 0.010%, Cr – 1.04%, Ni – 0.10%, Cu – 0.15%.

Fig. 4. The surface of the lower race
(visible fracturing and minor material losses, minor rolling)

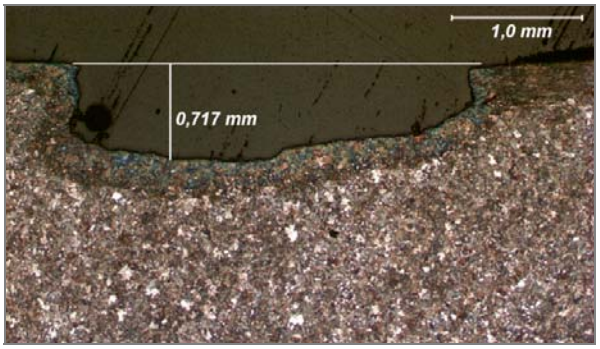

Fig. 5. Structure and form of the outflows

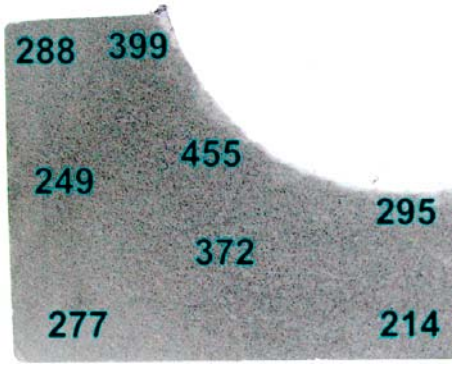

Fig. 6. Race hardness determined by the Brinell method

Hardness measurements of the race ring were determined. The results of examination of hardness were presented on Figure 6. The hardness measurements showed that

hardness in the area near surface of race exceeds the value of 455HB. It confirms that, stiffness of the supporting structures to ensure even distribution of forces over the rolling elements of the bearing is different and this cause creation of local plastic zones with hardness.

The balls had become significantly worn – they showed concave abrasion marks characteristic of ball blocking, which was caused by the neighbouring rolling balls. The diameter measurements showed diameter wear of about 0.7 mm and ovalization of 0.5 mm.

The basic method used while diagnosing surface cracks are the methods based on magnetic field distortion caused by discontinuity in ferromagnetic materials. The bearing in question did not show sings of larger cracks. Moreover, the long-term operation caused the contact surface between the race segments to roll to a considerable depth, so that applying the aforesaid method did not reveal the presence of a crack.

The above methods allowed damage to be detected; however, for the bearing to work properly, correct geometry of the contact point between the rolling element and the race must be maintained [6]. An issue largely ignored in literature for this type of bearings is the alteration of the race geometry after a long-term operation.

The change of the race thickness as a result of rolling and abrasive wear is a crucial issue for the distribution of loads onto the various rolling elements of the bearing. A direct measurement is often difficult to perform as the base surface may be damaged by cages, or by rolling of the race material over the upper race edge and therefore it is in fact only possible after the disassembly of the segments. Applying ultrasound methods may be helpful in this case.

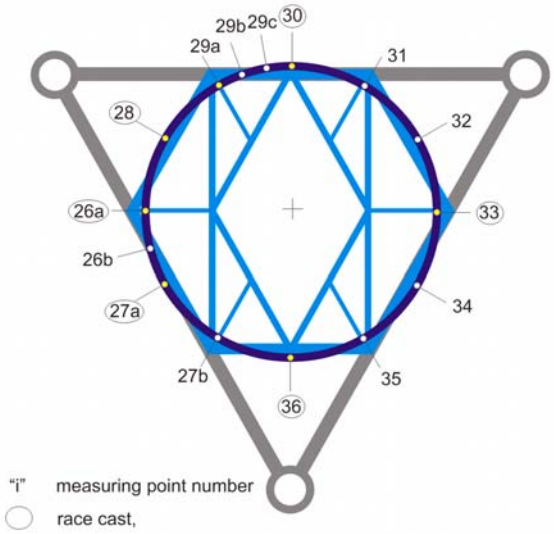

Fig. 7. Points of race thickness measurement ("i" measuring point number, thickness measurement, crack examination, o – race cast)

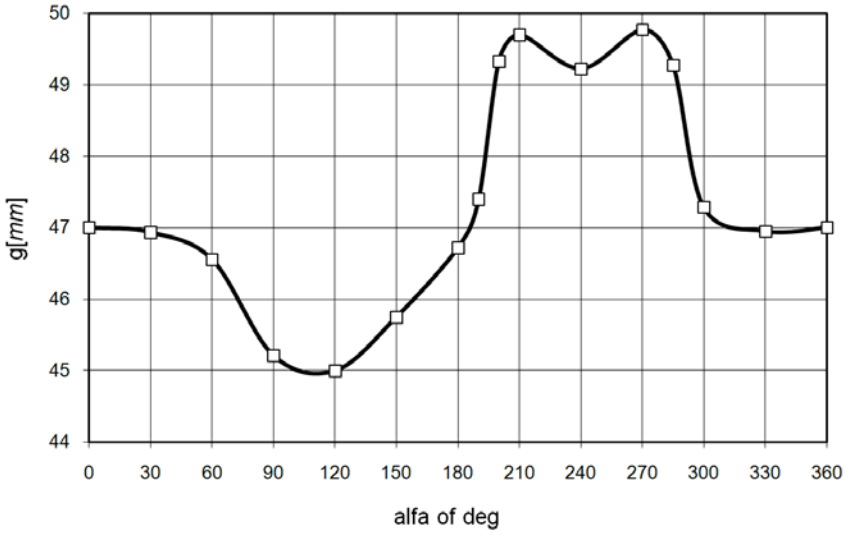

Fig. 8. Change of lower race thickness along the bearing circumference

Figure 7 shows the distribution of measuring points on the bearing circumference. The reading accuracy of 0.5 mm is sufficient for the measurement. In the bearing in question, a reduction of lower race thickness from 5.3 mm in soft points of the supportive structure to 10 mm in hard points was obtained (Figure 8).

The measurement results correspond to the observations made during rolling inspection. Detailed results will be published separately, after wear measurements have been taken for the upper race as well.

Another geometrical feature necessary for the assessment of the impact of long-term operation on the phenomena occurring on the contact surface between the rolling element and the race is the determination of the race curvature radii and congruence coefficient. Due to the uneven race wear, both total and local, it is impossible to carry out these measurements directly in the field. In the case of replaceable bearings, a piece of the race can be taken out for laboratory examination. In the case of bearings used for further work or having large rolling elements, it is easier to make a cast of the race.

A number of lower race casts have been made. The points were chosen on the basis of the analysis of the geometry of the supportive construction and the thickness measurement results. The race shape was converted to a numeric form using a DIGIBOT scanner with a 1º radial scale and a 1 mm circumferential scale, with the accuracy of 0.01 mm. Figure 9 presents a virtual 3D model of the race cast.

This model allows further analysis of the contact surface. Due to micro-losses, statistical methods must be applied in order to determine local curvature radii with high precision. For the bearing in question, curvature radii on the race bottom and walls (inclination angles of 20, 40 and 60º) were determined. Results for two samples are given in Figure 10.

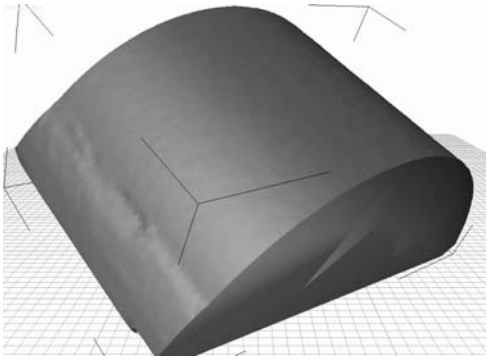

Fig. 9. A virtual model of the race surface

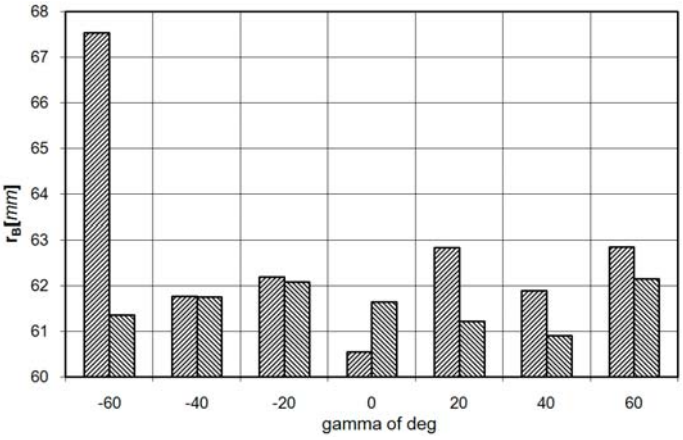

Fig. 10. Curvature radii for two different race sections

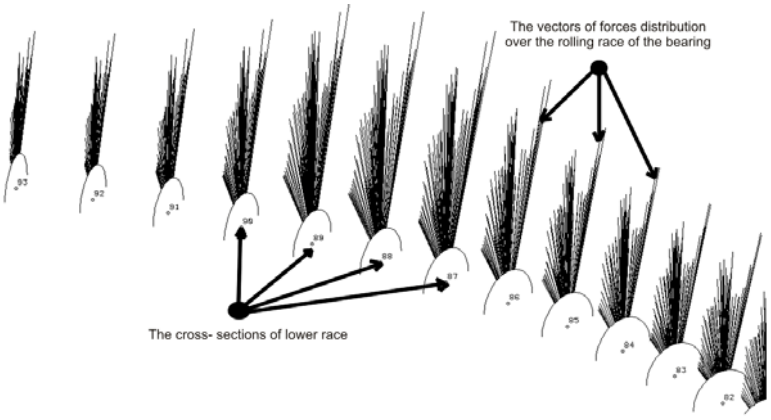

Fig. 11. Examples of maximum pressure envelopes along the race section obtained numerically

It was observed that as a result of loads in force, the congruence coefficient grew to about 0.967, which means a better fit between the ball and the race.

The largest congruence occurred in points of the heaviest pressure caused by rolling element exceedance, i.e. not on the race bottom but on the race walls. This is in line with the results of the distribution of the maximum pressure envelopes along the race section with a 360^{o} rotation of the body obtained from numerical models [4] in the finite element method for another bearing of the same type. The Figure 11 presented vectors of forces distribution over the rolling race of the bearing for exploitations conditions.

4. Final conclusions

An analysis of a stacker bearing degradation was carried out using advanced experimental and computer-assisted methods [7, 9–10]. The bearing under inspection is in a good technical condition in spite of a long-term operation, both as regards the state of its surface and its wear and tear. Various measurement methods have been applied and results corresponding to a numerical simulation by the finite element method have been obtained [8], which confirms the accuracy of the assumptions made while constructing virtual models [4–7]. The results of the geometric measurements of the bearing, in particular those related to the change in congruence coefficient (fitting between the ball and the race) may be used for construction of numerical models of bearings and supportive constructions of stackers. It is necessary to take measurements of machines exposed to larger dynamic loads and larger lateral forces (excavators) in order to verify the numerical models of bearings exposed to heavy loads.

References

[1] Durst W., Vogt W.: *Schaufelradbagger*, Trans Tech Publications, 1986.
[2] Rasper L.: *Kugeldrehverbindungen bei Tagebaugroßgeräten*, Braunkohle, Vol. 11, 1972, pp. 360–369.
[3] Rusiński E.: *Metoda elementów skończonych system COSMOS/M*, Warszawa, 1994.
[4] Smolnicki T.: *Nieliniowe modele układu bieżnia-kula-bieżnia do wyznaczenia rozkładu nacisków w wielkogabarytowym łożysku tocznym*, Przegląd Mechaniczny, No 5–6, 1999.
[5] Smolnicki T., Malcher K.: *Wpływ parametrów układu element toczny-bieżnia na jego nośność*, V Międzynarodowa Konferencja Komputerowe Wspomaganie Prac Inżynierskich, Polanica Zdrój, 2000.
[6] Smolnicki T.: *Modele numeryczne element toczny–bieżnia w wielkogabarytowych łożyskach tocznych*, XIII Konf. Nauk. Problemy Rozwoju Maszyn Roboczych, Zakopane, 2000.
[7] Smolnicki T., Rusiński E., Malcher K.: *Modele dyskretne łożysk wieńcowych w maszynach podstawowych górnictwa odkrywkowego*, III Konwersatorium Bezpieczeństwo oraz degradacja maszyn, Wrocław–Szklarska Poręba, 1997.
[8] Rusiński E., Moczko P., Czmochowski J.: *Numerical and exeprimental analysis of mines loader boom crack*, Aumation in Constraction, Vol. 17, 2008, pp. 271–277.

[9] Kania L., Pytlarz R., Reszke P.: *Numerical analysis of hardness factor in modelling of contact zone in large roller bearing*, Transport Przemysłowy, No. 1, No. 7, 2010, pp. 62–65.
[10] Rusinski E., Czmochowski J., Iluk A., Kowalczyk M.: *An analysis of the causes of a BWE counterweight boom suport fracture*, Engineering Failure Analysis, Vol 17, 2010, 179–191.

Degradacja łożyska wieńcowego zwałowarki

Wielkogabarytowe łożyska toczne obrotu nadwozia maszyn podstawowych górnictwa odkrywkowego wykonywane są w postaci jedno- lub dwurzędowych łożysk kulowych. Średnice podziałowe tych łożysk osiągają nawet 20 m, a elementy toczne mają średnicę od 100 do 250 mm, a przenoszą przyłożone mimośrodowo obciążenie osiowe od kilku do kilkudziesięciu MN. Ze względu na małą sztywność podzespołów wsporczych i jej niejednorodność po obwodzie łożyska obciążenie elementów tocznych jest w tych łożyskach bardzo nierównomierne. Przepływ strumienia obciążenia koncentruje się w miejscach, które leżą w strefach o większej sztywności. Ze względu na specyfikę tych, produkowanych jednostkowo maszyn, uzyskanie wiarygodnych danych do modeli numerycznych jest możliwe tylko w oparciu o analizę już istniejących łożysk i ich konstrukcji wsporczych poddanych wieloletniej eksploatacji. W artykule przedstawiono metody stosowane do oceny wpływu długotrwałej eksploatacji na zmianę parametrów łożyska.